

THE ELECTRONIC BAND STRUCTURE OF III (IN, AL, GA)-V (N, AS, SB)
COMPOUNDS AND TERNARY ALLOYS

A THESIS SUBMITTED TO
THE GRADUATE SCHOOL OF NATURAL AND APPLIED SCIENCES
OF
MIDDLE EAST TECHNICAL UNIVERSITY

BY

REZEK MOHAMMAD

IN PARTIAL FULFILLMENT OF THE REQUIREMENTS

FOR

THE DEGREE OF DOCTOR OF PHILOSOPHY

IN

PHYSICS

JULY 2005

Approval of the Graduate School of Natural and Applied Sciences.

Prof. Dr. Canan Özgen
Director

I certify that this thesis satisfies all the requirements as a thesis for the degree of Doctor of Philosophy.

Prof. Dr. Sinan Bilikmen
Head of Department

This is to certify that we have read this thesis and that in our opinion it is fully adequate, in scope and quality, as a thesis for the degree of Doctor of Philosophy.

Prof. Dr. Şenay Katırcıoğlu
Supervisor

Examining Committee Members

Prof. Dr. Ziya Güvenç (Çankaya University) _____

Prof. Dr. Demet Gülen (METU, PHYS) _____

Prof. Dr. Şinasi Ellialtıoğlu (METU, PHYS) _____

Assoc. Prof. Dr. Hatice Kökten (METU, PHYS) _____

Prof. Dr. Şenay Katırcıoğlu (METU, PHYS) _____

“I hereby declare that all information in this document has been obtained and presented in accordance with academic rules and ethical conduct. I also declare that, as required by these rules and conduct, I have fully cited and referenced all material and results that are not original to this work.”

Name Surname : Rezek Mohammad

Signature :

ABSTRACT

THE ELECTRONIC BAND STRUCTURE OF III (In, Al, Ga)-V (N, As, Sb) COMPOUNDS AND TERNARY ALLOYS

Mohammad, Rezek Mahmoud Salim

Ph.D., Department of Physics

Supervisor: Prof. Dr. Şenay Katırcıoğlu

July 2005, 155 pages.

In this work, the electronic band structure of III (*In, Al, Ga*) - V (*N, As, Sb*) compounds and their ternary alloys have been investigated by density functional theory (DFT) within generalized gradient approximation (GGA) and empirical tight binding (ETB) calculations, respectively.

The present DFT-GGA calculations have shown direct band gap structures in zinc-blende phase for *InN*, *InAs*, *InSb*, *GaN*, and *GaAs*. However, indirect band gap structures have been obtained for cubic *AlN*, *AlSb* and *AlAs* compounds; here, the conduction band minima of both *AlN* and *AlAs* are located at X symmetry point, while that of *AlSb* is at a position lying along $\Gamma - X$ direction.

An important part of this work consists of ETB calculations which have been parameterized for sp^3d^2 basis and nearest neighbor interactions to study the band gap bowing of III(*In, Al*)- V(*N, As, Sb*) ternary alloys. This ETB model provides a satisfactory electronic properties of alloys within reasonable calculation time compared to the calculations of DFT. Since the present ETB energy parameters

reproduce successfully the band structures of the compounds at Γ and X symmetry points, they are considered reliable for the band gap bowing calculations of the ternary alloys.

In the present work, the band gap engineering of InN_xAs_{1-x} , InN_xSb_{1-x} , $InAs_xSb_{1-x}$, $Al_{1-x}In_xN$, $Al_{1-x}In_xSb$ and $Al_{1-x}In_xAs$ alloys has been studied for total range of constituents ($0 < x < 1$). The downward band gap bowing seems the largest in InN_xAs_{1-x} alloys among the alloys considered in this work. A metallic character of InN_xAs_{1-x} , InN_xSb_{1-x} and $InAs_xSb_{1-x}$ has been obtained in the present calculations for certain concentration range of constituents (N, As) as predicted in the literature. Even for a small amount of contents (x), a decrease of the electronic effective mass around Γ symmetry point appears for InN_xAs_{1-x} , InN_xSb_{1-x} and $InAs_xSb_{1-x}$ alloys manifesting itself by an increase of the band curvature. The calculated cross over from indirect to direct band gap of ternary Al alloys has been found to be consistent with the measurements.

As a last summary, the determinations of the band gaps of alloys as a function of contents, the concentration range of constituents leading to metallic character of the alloys, the change of the electronic effective mass around the Brillouin zone center (Γ) as a function of alloy contents, the cross over from indirect to direct band gap of the alloys which are direct on one end, indirect on the other end, are main achievements in this work, indispensable for the development of materials leading to new modern circuit components.

Keywords: Electronic Band Structure, InN , $InAs$, $InSb$, AlN , $AlSb$, $AlAs$, GaN , $GaAs$, InN_xAs_{1-x} , InN_xSb_{1-x} , $InAs_xSb_{1-x}$, $Al_{1-x}In_xN$, $Al_{1-x}In_xSb$, $Al_{1-x}In_xAs$, Density Functional Theory (DFT), Empirical Tight Binding (ETB), Band Gap Bowing.

ÖZ

III (In, Al, Ga) - V (N, AS, Sb) BİLEŞİK VE ÜÇLÜ ALAŞIMLARININ ELEKTRONİK BAND YAPILARI

Mohammad, Rezek Mahmoud Salim

Doktora, Fizik Bölümü

Tez Yöneticisi: Prof. Dr. Şenay Katırcıoğlu

Temmuz 2005, 155 sayfa.

Bu çalışmada, III (*In, Al, Ga*)-V (*N, As, Sb*) bileşiklerinin band yapıları, genelleştirilmiş dereceli yaklaşım (GGA) içinde yoğunluk fonksiyonu kuramı (DFT) ile hesaplanmış, ve bu bileşiklerin üçlü alaşımlarının band yapılarının elde edilmesi de dış güdümlü sıkı bağ kuramı (ETB) hesaplarıyla sağlanmıştır.

Sonuçlandırılan DFT-GGA hesaplamalarına göre, band yapı olarak *InN*, *InAs*, *InSb*, *GaN* ve *GaAs* doğrudan band geçişli, *AlN*, *AlAs* ve *AlSb* bileşikleri ise dolaylı geçişlidir. Yukarıda belirtilen son grup bileşiklerde, iletim bandının minimumu *AlSb* için Γ -X yönünde bir konumda bulunurken, *AlN* ve *AlAs* bileşiklerinde ise X simetri noktasındadır.

Bu çalışmanın önemli bir bölümü olan ETB hesaplamaları, III (*In, Al*)-V (*N, As, Sb*) üçlü alaşımlarının band aralık bükülmesini incelemek için sp^3d^2 bazlı ve en yakın komşu etkileşmeli olarak parametrize edilmiştir. Bu ETB modeli, alaşımların kabul edilebilir elektrik özelliklerini DFT hesaplamalarına göre çok daha kısa hesaplama zamanı içinde verir. Sonuç olarak, ETB enerji parametreleri

Γ ve X simetri noktalarında bileşiklerin band yapılarını başarıyla ürettiklerinden, üçlü alaşımların band aralık bükülme hesaplamalarında güvenle kullanılmıştır.

Bu çalışmada InN_xAs_{1-x} , InN_xSb_{1-x} , $InAs_xSb_{1-x}$, $Al_{1-x}In_xN$, $Al_{1-x}In_xSb$ ve $Al_{1-x}In_xAs$ alaşımlarının band aralık değişimi, toplam katkı oranı ($0 < x < 1$) işlevinde incelenmiştir. Bu çalışmadaki alaşımlar arasında en fazla aşağı doğru band aralık bükülmesinin InN_xAs_{1-x} alaşımına ait olduğu bulunmuştur.

Literatürde öngörülen InN_xAs_{1-x} , InN_xSb_{1-x} ve $InAs_xSb_{1-x}$ 'in metalik karakterleri, belirli katkı (N, As) aralığı içinde ETB hesaplamalarıyla elde edilmiştir. Öte yandan InN_xAs_{1-x} , InN_xSb_{1-x} ve $InAs_xSb_{1-x}$ alaşımlarının Γ simetri noktası çevresinde band bükülmesinin artması ile kendini gösteren elektron etkin kütle azalması saptanmıştır. $Al_{1-x}In_xN$, $Al_{1-x}In_xSb$ ve $Al_{1-x}In_xAs$ alaşımları için hesaplanan dolaylı band aralığından doğrudan band aralığına geçiş noktasının deneysel sonuçlarla uyumlu olduğu bulunmuştur.

Bu çalışmanın son bir toparlaması olarak,

katkı oranı işlevinde alaşımların band aralığının bulunması, alaşımların metalik özellik gösterdiği katkı aralığının saptanması, Brillouin zone merkezi (Γ) çevresinde katkı oranı işlevinde elektron etkin kütle değişiminin saptanması, bir ucunda dolaylı band geçişli, diğer ucunda doğrudan band geçişli üçlü alaşımlarda katkı oranı değişiminin dolaylı / doğrudan band geçişine karşılık gelen değerinin bulunması,

yeni devre bileşenlerine yol açabilecek malzemelerin belirlenmesini sağlayan başlıca sonuçlardır.

Anahtar Kelimeler: Elektronik Band Yapı, InN , $InAs$, $InSb$, AlN , $AlSb$, $AlAs$, GaN , $GaAs$, InN_xAs_{1-x} , InN_xSb_{1-x} , $InAs_xSb_{1-x}$, $Al_{1-x}In_xN$, $Al_{1-x}In_xSb$, $Al_{1-x}In_xAs$, Yoğunluk Fonksiyonu Kuramı (DFT), Dış Güdümlü Sıkı Bağ Kuramı (ETB), Band Aralığı Bükülmesi.

... TO MY PARENTS

ACKNOWLEDGMENTS

I would like to express my sincere feelings to my supervisor, *Prof. Dr. Şenay Katırcioğlu*. I am grateful for her painstaking care in the course of this project, for her meticulous effort in teaching me very precious, numerous concepts. I could have done nothing without her. I would like to thank also all the people in the physics department for their endless help during my study. Finally, there is no words in the dictionary that can describe the Turkish people for their hospitality, generosity and kindness which I received and feel during my stay in this beautiful country.

TABLE OF CONTENTS

ABSTRACT	iv
ÖZ	vi
DEDICATION	viii
ACKNOWLEDGMENTS	viii
TABLE OF CONTENTS	x
LIST OF TABLES	xiii
LIST OF FIGURES	xv
1 INTRODUCTION	1
2 THEORY OF CALCULATION	6
2.1 Introduction	6
2.2 First Principles Computational Theory	8
2.2.1 Level 1: The Born-Oppenheimer approximation	9
2.2.2 Level 2: Hartree and Hartree-Fock Approximation	10
2.2.3 Level 3: Density Functional Theory	14
2.2.4 Level 4: Solving the equations	23
2.3 Empirical Tight Binding Theory	25
2.4 Computational Steps of the Work	28
3 THE ELECTRONIC STRUCTURE OF InN, InAs AND InSb COMPOUNDS	38
3.1 Introduction	38

3.2	The results	43
3.2.1	InN	43
3.2.2	InAs	51
3.2.3	InSb	57
4	THE ELECTRONIC BAND STRUCTURE OF InN_xAs_{1-x} , InN_xSb_{1-x} AND $InAs_xSb_{1-x}$ ALLOYS	65
4.1	Introduction	65
4.2	Electronic structure of alloys	67
4.2.1	InN_xAs_{1-x}	67
4.2.2	InN_xSb_{1-x}	73
4.2.3	$InAs_xSb_{1-x}$	76
5	THE ELECTRONIC BAND STRUCTURE OF AlN, AlSb, AlAs AND THEIR TERNARY ALLOYS WITH In.	84
5.1	Introduction	84
5.2	Electronic band structure of compounds	87
5.2.1	AlN	87
5.2.2	AlSb	93
5.2.3	AlAs	95
5.3	Electronic structure of ternary alloys	102
5.3.1	$Al_{1-x}In_xN$	102
5.3.2	$Al_{1-x}In_xSb$	107
5.3.3	$Al_{1-x}In_xAs$	110
6	THE ELECTRONIC BAND STRUCTURE OF GaN AND GaAs COMPOUNDS	114
6.1	Introduction	114
6.2	The results	119
6.2.1	<i>c-GaN</i>	119
6.2.2	GaAs	126

7	CONCLUSIONS	133
	REFERENCES	140

LIST OF TABLES

3.1	Empirical matrix elements of the sp^3d^2 Hamiltonian in eV.	42
3.2	The theoretical and experimental lattice constant values (a_{th}, a_{exp}) in Å for InN , $InAs$ and $InSb$ in cubic phase.	45
3.3	A summary of the important features, energy gaps and valance band-widths of the present DFT (adjusted) and ETB band structure for $c-InN$ compared to other experimental and theoretical calculational results. All energies are in eV.	50
3.4	A summary of the important features, energy gaps and valance band-widths of the present DFT (adjusted) and ETB band structure for $InAs$ compared to other experimental and theoretical calculational results. All energies are in eV.	55
3.5	A summary of the important features, energy gaps and valance band-widths of the present DFT (adjusted) and ETB band structure for $InSb$ compared to other experimental and theoretical calculational results. All energies are in eV.	62
5.1	Empirical matrix elements of the sp^3d^2 Hamiltonian in eV.	87
5.2	The theoretical and experimental lattice constant values (a_{th}, a_{exp}) in Å for AlN , $AlAs$ and $AlSb$ in cubic phase.	88
5.3	A summary of the important features, energy gaps and valance band-widths of the present DFT (adjusted) and ETB band structure for cubic AlN compared to other experimental and theoretical results. All energies are in eV.	92
5.4	A summary of the important features, energy gaps and valance band-widths of the present DFT (adjusted) and ETB band structure for $AlSb$ compared to other experimental and theoretical calculations results. All energies are in eV.	96
5.5	A summary of the important features, energy gaps and valance band-widths of the present DFT (adjusted) and ETB band structure for $AlAs$ compared to other experimental and theoretical calculations results. All energies are in eV.	101

5.6	The bowing parameters (in eV) for direct and indirect transitions of alloys at Γ and X symmetry points	105
6.1	Empirical matrix elements of the sp^3d^2 Hamiltonian in eV.	118
6.2	The theoretical and experimental lattice constant values (a_{th}, a_{exp}) in \AA for GaN and $GaAs$ in cubic phase.	121
6.3	A summary of the important features, energy gaps, and valence bandwidths of the present DFT (adjusted) and ETB band structure for $c-GaN$ compared to other experimental and calculational results. All energies are in eV.	124
6.4	A summary of the important features, energy gaps and valence bandwidths of the present DFT (adjusted) and ETB band structure for $GaAs$ compared to other experimental and calculational results. All energies are in eV.	131

LIST OF FIGURES

2.1	Flow chart for the n^{th} iteration in the self-consistent procedure to solve <i>Hartree – Fock</i> or <i>Kohn – Sham</i> equations	21
2.2	The ETB Hamiltonian matrix for the sp^3d^2 model.	35
3.1	Total energy of <i>c-InN</i> versus the lattice volume.	44
3.2	The energy band structure of <i>c-InN</i> by FP-LAPW(adjusted) (dotted line) and ETB (solid line).	48
3.3	Total energy of <i>InAs</i> versus the lattice volume.	52
3.4	The energy band structure of <i>InAs</i> by FP-LAPW (adjusted) (dotted line) and ETB (solid line).	56
3.5	Total energy of <i>InSb</i> versus the lattice volume.	58
3.6	The energy band structure of <i>InSb</i> by FP-LAPW (adjusted) (dotted line) and ETB (solid line).	61
4.1	Band-gap energy vs composition (x) for <i>InN_xAs_{1-x}</i> alloys.	70
4.2	The conduction band dispersion calculated for <i>InN_xAs_{1-x}</i> alloys with x = 0% (solid line), 2% (dashed line), 6% (dotted line) and 12% (star line) around Γ point at 0 K.	72
4.3	Band-gap energy vs composition (x) for <i>InN_xSb_{1-x}</i> alloys.	75
4.4	The conduction band dispersion calculated for <i>InN_xSb_{1-x}</i> alloys with x = 0% (solid line), 2% (dashed line), 6% (dotted line) and 14% (star line) around Γ point at 0 K.	77
4.5	Band-gap energy vs composition (x) for <i>InAs_xSb_{1-x}</i> alloys.	80
4.6	The conduction band dispersion calculated for <i>InAs_xSb_{1-x}</i> alloys with x = 0% (solid line), 2% (dashed line), 6% (dotted line) and 15% (star line) around Γ point at 0 K.	83
5.1	The energy band structure of <i>c-AlN</i> by FP-LAPW (adjusted) (dotted line) and ETB (solid line).	91
5.2	The energy band structure of <i>AlSb</i> by FP-LAPW(adjusted) (dotted line) and ETB (solid line).	97

5.3	The energy band structure of <i>AlAs</i> by FP-LAPW (adjusted) (dotted line) and ETB (solid line).	100
5.4	Dependence of E_g^Γ (solid line), E_g^X (dotted line), $E_g^\Gamma(av)$ (zig-zag line) and $E_g^X(av)$ (dashed line) of $Al_{1-x}In_xN$ on the <i>In</i> composition (x). .	104
5.5	Dependence of E_g^Γ (solid line), E_g^X (dotted line), $E_g^\Gamma(av)$ (zig-zag line) and $E_g^X(av)$ (dashed line) of $Al_{1-x}In_xSb$ on the <i>In</i> composition (x). .	109
5.6	Dependence of E_g^Γ (solid line), E_g^X (dotted line), $E_g^\Gamma(av)$ (zig-zag line) and $E_g^X(av)$ (dashed line) of $Al_{1-x}In_xAs$ on the <i>In</i> composition (x). .	112
6.1	Total energy of <i>c-GaN</i> versus the lattice volume.	120
6.2	The energy band structure of <i>c-GaN</i> by FP-LAPW(adjusted) (dotted line) and ETB (solid line).	123
6.3	Total energy of <i>c-GaAs</i> versus the lattice volume.	127
6.4	The energy band structure of <i>c-GaAs</i> by FP-LAPW(adjusted) (dotted line) and ETB (solid line).	130

CHAPTER 1

INTRODUCTION

Nowadays semiconductors can be grown with varying composition, a few atomic layers at a time. As a result the number of possible new electronic devices and materials for more application and the quality of the existing devices is increasing much more.

The *III* nitride (*InN*, *AlN* and *GaN*) semiconductors are potentially useful at high frequency, microwave and short-wave-length electroluminescent devices. *InN*, *AlN* and *GaN* are used for the fabrication of high speed heterojunction transistors [1] and low cost solar cells with high efficiency [2]. They are also increasingly used for visible light emitting diodes (*LEDs*) [3, 4] and laser diodes (*LDs*) [5–8] for the amber, green, blue and UV regions of the spectrum and also as the basis for high power, high temperature electronic devices [9, 10].

The *III*-Arsenide compounds (*InAs*, *AlAs* and *GaAs*) are the most used semiconductors in device technology. *InAs* has a high electron mobility, it may prove

an important material for use in high speed electronics [11, 12]. The second compound of *As*, *AlAs*, has been widely used as a barrier material in modulation-doped heterostructures and quantum well of a lattice matched heterojunctions [13, 14].

The III-Antimonide compounds (*InSb* and *AlSb*) characterized by their low energy gaps compared with the other III-V compounds. *InSb* has the lowest energy gap of any of the binary III-V materials, which makes it an interesting narrow gap semiconductors from the point of view of optical spectroscopy and optoelectronic applications [15]. This property often allows the fabrication of infrared imaging systems, free space communications, and gas phase detection systems [16, 17]. The bulk *AlSb* has been considered as a potential materials for infrared detectors and optical holographic memories [18, 19]. Epitaxial *AlSb* has been used as a component of resonant tunneling diodes [20].

Because of the large difference between the electronic band gap (the energy difference between the bottom of the conduction band and the top of the valence band), alloying semiconductors from III-V group are of particular importance for optoelectronic devices; optoelectronic devices can be designed that cover a wide spectral range.

The ternary alloys of *In*, InN_xAs_{1-x} , $InN_{1-x}Sb_x$ and $InAs_{1-x}Sb_x$, together with the alloys of *Ga*, $GaAs_xN_{1-x}$ and $GaSb_xN_{1-x}$, are the potential materials for room temperature infrared detectors, gas sensors and lasers operating in near

infrared (0.9-1.3 μm), mid - infrared (2-5 μm) and far infrared (8- 12 μm) regions [21, 22, 24–31]. It has been reported that the $Al_{1-x}In_xN$ alloys can have applications as a cladding layer or an active layer for LEDs and LDs emitting an extremely wide spectral region covering from deep ultraviolet (UV) to infrared [32], and as a potential material for thermoelectric power devices [33]. The $AlAs$ based ternary $Al_{1-x}In_xAs$ alloys have been reported as an important buffer layer materials between $InAs$ and substrate in the technology of optoelectric devices such as lasers and single electron transistors [34, 35]. Recently, $Al_{1-x}In_xAs$ alloys have been grown also for ultra fast switching device applications [36]. On the other hand the epitaxial growth of $AlInAs$ on $GaAs$ has been reported as a candidate material for triple function solar cells in a very efficiency [37]. The ternary $AlInSb$ alloys have been used as a buffer layer for multiple quantum lasers [38]. Recently, it has been reported that, $AlInSb$ alloys can be also potential materials to fabricate high efficiency low cost photovoltaic cells and photodetectors [39].

The experimental data about the III-V compounds and their ternary and quaternary alloys are limited by a few data which are available only at high symmetry points (Γ , X) in the Brillouin zone. This situation will put, as always, new demands on theorists to predict the properties of exotic semiconductors before the materials even fabricated. The theoretical methods which can be used for this purpose can be classified according to the input data:

1. First principles calculations (ab-initio calculations): In these kind of calculations only the atomic number and the number of the atoms are used as an input for the calculations. Full potential linearized augmented plane wave (FP-LAPW) method based on density functional theory (DFT) within local density approximation (LDA) [40, 41] or generalized gradient approximation (GGA) [40–42], and Hatree-Fock [43] method are extremely used first principles calculational methods in the literature.

2. Empirical methods: This kind of calculational methods need interaction energy parameters which are externally obtained from either experimental measurements or the first principles calculational results. The $\vec{k} \cdot \vec{p}$ [44, 45], empirical pseudopotential [46] and empirical tight binding [47, 48] are widely used empirical methods in the literature.

In the present work, FP-LAPW method within GG approximation is carried on *InN*, *InAs*, *InSb*, *AlN*, *AlSb*, *AlAs*, *GaN*, and *GaAs* compounds to find out the electronic band structure of them. Because of the time consuming problem in the first principles calculations of alloys, ETB method is mainly used in the present work to study the band bowing of *InN_xAs_{1-x}*, *InN_xSb_{1-x}*, *InAs_xSb_{1-x}*, *Al_{1-x}In_xN*, *Al_{1-x}In_xSb* and *Al_{1-x}In_xAs* alloys. The present FP-LAPW calculational results of the compounds are used in the derivation of ETB energy parameters of the alloys.

This thesis is organized as follows: In chapter II, the calculational methods used in this work are explained and formulated, in chapter III, V and VI, the electronic band structure of InN , $InAs$, $InSb$ and AlN , $AlSb$, $AlAs$ and GaN , $GaAs$ has been studied, respectively. The band gap bowing of the InN_xAs_{1-x} , InN_xSb_{1-x} , $InAs_xSb_{1-x}$ and ternary alloys of AlN , $AlAs$ and $AlSb$ with In has been studied in chapters IV and V, respectively, Finally, conclusion of the whole present work is outlined in chapter VII.

CHAPTER 2

THEORY OF CALCULATION

2.1 Introduction

As a result of recent successes in describing and predicting properties of materials, atomistic simulations in general and electronic structure calculations in particular have become increasingly important in the fields of physics and chemistry over the past decade, especially with the advent of present-day, high-performance computers. Assuming a knowledge of the types of atoms comprising any given material, a computational approach enables us to answer two basic questions:

- What is the atomic structure of the material?
- What are its electronic properties?

Besides this, it would be nice to get the answer to another question:

- How can we modify the bonding between atoms or the material chemical content to create novel materials with predetermined properties?

A number of methods to derive answers to these questions have been developed. These methods for computing the structure and properties of materials can conditionally be divided into two classes: those that do not use any empirically or experimentally derived quantities, and those that do. The former are often called ab-initio, or first principles methods like density functional theory (DFT), while the latter are called empirical or semi-empirical like empirical tight binding (ETB). The ab-initio methods are particularly useful in predicting the properties of new materials and for predicting trends across a wide range of materials.

The calculation of the energy levels of electrons in solids, that is the determination of the energy bands, is a central theoretical problem of solid state physics. Knowledge of these energies and of electron wave function is required, in principle, for any calculation of more directly observable properties including electrical and thermal conductivities, optical dielectric function, vibrational spectra and so on.

In practice, phenomenological models are often employed which apparently do not require such specific information, however, it means a task for fundamental theory to account for the values obtained for the parameters of such a model. The parameters of the considered models are the functions of the crystal potential which can, in principle, be determined from the results of a sufficiently complete energy band calculation.

In the present work, the sufficiently complete energy band structure of compounds, such as *InN*, *InAs*, *InSb*, *AlN*, *AlSb*, *AlAs*, *GaN* and *GaAs*, has been obtained by the combination of first principle and empirical calculations based on density functional and tight binding theories, respectively. The theories of the calculational methods considered in this work have been outlined in the following sections.

2.2 First Principles Calculational Theory

A solid is a collection of heavy, positively charged particles (nuclei) compared to lighter, negatively charged particles (electrons). If the structure composed of N nuclei and each has Z electrons, then, the theorists came face to face with a problem of N (nuclei) + $Z N$ (electrons) electromagnetically interacting particles. This is a many-body problem, and because these particles are so light compared with classical scale, it is a quantum many body problem. In principle, to study the materials and their properties, the theorist has to solve the time independent Schrödinger equation.

$$\widehat{H}\Psi = E\Psi \quad (2.1)$$

Here, Ψ is the wave function of all participating particles and \widehat{H} is the exact many-particle Hamiltonian for this system.

$$\widehat{H} = -\frac{\hbar^2}{2} \sum_i \frac{\nabla_{\vec{R}_i}^2}{M_i} - \frac{\hbar^2}{2} \sum_i \frac{\nabla_{\vec{r}_i}^2}{m_e} - \frac{1}{4\pi\epsilon_0} \sum_{i,j} \frac{e^2 Z_i}{|\vec{R}_i - \vec{r}_j|} +$$

$$\frac{1}{8\pi\epsilon_0} \sum_{i \neq j} \frac{e^2}{|\vec{r}_i - \vec{r}_j|} + \frac{1}{8\pi\epsilon_0} \sum_{i \neq j} \frac{e^2 Z_i Z_j}{|\vec{R}_i - \vec{R}_j|} \quad (2.2)$$

The mass of the nucleus at \vec{R}_i is M_i , the mass of the electron at \vec{r}_i is m_e . The first term in equation (2.2) is the kinetic energy operator for the nuclei (\hat{T}_n), the second for the electrons (\hat{T}_e). The last three terms correspond to Coulomb electron-nuclear attraction (\hat{V}_{en}), electron-electron repulsion (\hat{V}_{ee}) and nuclear-nuclear repulsion (\hat{V}_{nn}), respectively. It is out of question to solve this many body problem exactly. In order to find acceptable approximate eigenstates (acceptable solution to Schrödinger equation (2.1)), three approximations at different levels can be used, they are:

- Born-Oppenheimer Approximation (BO),
- Hartree and Hartree-Fock Approximation (H, HF),
- Density Functional theory (DFT),

These approximations make the calculations easy to be handled by transforming the many body problem to one body problem.

2.2.1 Level 1: The Born-Oppenheimer approximation

One of the most important approximation in materials science is the Born-Oppenheimer approximation. It is used in the vast majority of methods. The essence of the approximation is that the nuclei are much heavier and therefore

much slower than the electrons. One can hence ‘freeze’ them at fixed positions and assume the electrons to be in instantaneous equilibrium with them. In another words, only the electrons are kept as players in this many body problems. The nuclei are deprived from this status, and reduced to a given source of positive charge; they become ‘external’ to the electron cloud. After the application of this approximation the problem is left with a collection of ZN interacting negative particles, moving in the (now external or given) potential of the nuclei. So the nuclei do not move any more, their kinetic energy is zero and the first term in equation (2.2) disappears and the last term reduces to a constant. Therefore the many body problem is left with the kinetic energy of the electron gas, the potential energy due to electron-electron interactions and the potential energy of the electrons in the (now external) potential of the nuclei. The new many body Hamiltonian is written formally as

$$\widehat{H} = -\frac{\hbar^2}{2} \sum_i \frac{\nabla_{\vec{r}_i}^2}{m_e} + \frac{1}{8\pi\epsilon_0} \sum_{i \neq j} \frac{e^2}{|\vec{r}_i - \vec{r}_j|} - \frac{1}{4\pi\epsilon_0} \sum_{i,j} \frac{e^2 Z_i}{|\vec{R}_i - \vec{r}_j|}$$

or

$$\widehat{H} = \widehat{T}_e + \widehat{V}_{ee} + \widehat{V}_{ext} \quad (2.3)$$

2.2.2 Level 2: Hartree and Hartree-Fock Approximation

The quantum many body problem obtained after the first level approximation (Born-Oppenheimer) is much simpler than the original one, but still difficult to solve. In Hartree approximation [43], the solution of many-electron Hamiltonian

is transformed to solve one-electron Hamiltonian by assuming the electrons are independent from each other. By this assumption the total wave function for the electrons is written as:

$$\Psi(r_1, r_2, \dots, r_N) = \prod_i^N \psi(r_i) \quad (2.4)$$

Where $\psi(r_i)$ is the electron wave function. Using this definition of the wave function the electron density is represented by:

$$\rho(r) = \sum_i^N |\psi_i(r)|^2 \quad (2.5)$$

The total Hamiltonian can be written as:

$$\begin{aligned} \widehat{H} = & -\frac{\hbar^2}{2m_e} \sum_i \nabla_{\vec{r}_i}^2 - \frac{1}{4\pi\epsilon_0} \sum_i \sum_j \int \frac{eZ_j |\psi(r_i)|^2 d^3r_i}{|\vec{R}_j - \vec{r}_i|} + \\ & \frac{1}{8\pi\epsilon_0} \sum_i \sum_j \frac{|\psi(r_i)|^2 |\psi(r_j)|^2 d^3r_j d^3r_i}{|\vec{r}_i - \vec{r}_j|} \end{aligned} \quad (2.6)$$

or

$$\widehat{H} = \widehat{T}_o + V_H[\psi] \quad (2.7)$$

The Schrödinger equation becomes non-linear and requires for the self-consistency procedure.

$$(\widehat{T}_o + V_H[\psi])\Psi = E_H\Psi \quad (2.8)$$

Here, \widehat{T}_0 is the functional for the kinetic energy of a non-interacting electron gas, V_H stands for the electron effective potential and E_H is the functional of electron energy using Hartree approximation. In order to solve an equation of this type,

one starts with some trial solution $\Psi^{(0)}$ (normally atomic orbitals wave function is used) which is used to construct the potential. Solving the nonlinear Schrödinger equation (2.8) with this potential, one can obtain a new solution $\Psi^{(1)}$ which is used in turn to build a new potential. This procedure is repeated until the ground state $\Psi^{(i)}$ and the corresponding energy E^i do not deviate appreciably from those in the previous step.

Hartree product wave functions suffer from several major flaws that serve to make them physically unrealistic:

- Hartree products do not satisfy the Pauli Antisymmetry Principle which states that the sign of any many-electron wave function must be antisymmetric (i. e. change sign) with respect to the interchange of the coordinates, both space and spin, of any two electrons. The Antisymmetry Principle is a postulate of quantum mechanics derived from relativistic arguments and is, at the end, equivalent to the more standard statement of the Pauli Principle which prevents two electrons with the same spin from occupying the same spatial orbital.
- Hartree product force a particular electron to occupy a given spin orbital despite the fact that electrons are indistinguishable from one another. Lastly, because the Hartree product wave function is constructed on the assumption that the electrons are non-interacting, there exists a non-zero probability

of finding two electrons occupying the exact same point in space.

Later this wave function is modified to include the spin of the electron by the Hartree-Fock approximation [49]. This approximation is an extension of the above Hartree approximation to include the permutation symmetry of the wave function which leads to the exchange interaction. Exchange is due to the Pauli exclusion principle, which states that the total wave function for the system must be antisymmetric under particle exchange. This means that when two arguments are swapped the wave function changes sign as follows:

$$\Psi(r_1, r_2, \dots, r_i, \dots, r_j, \dots, r_N) = -\Psi(r_1, r_2, \dots, r_j, \dots, r_i, \dots, r_N) \quad (2.9)$$

Where r_i includes coordinates of position and spin. Therefore no two electrons can have the same set of quantum numbers, and electrons with the same spin cannot occupy the same state simultaneously.

Instead of using the simple product form of the wave function shown in Eq (2.4), a Slater determinant wave function [50] which satisfies antisymmetry is used. As a result of the antisymmetry wave function, Eq (2.8) can be written as:

$$E_{HF} = \hat{T}_o + V_H \quad (2.10)$$

E_{HF} is the functional electron energy using Hartree-Fock approximation, \hat{T}_o is the functional for the kinetic energy of a non-interacting electron gas and V_H stands for the electron effective potential. The solution steps of Eq. (2.10) are the same as they are defined for Hartree Eq. (2.7).

Hartree-Fock approximation performs very well for atoms and molecules, and therefore used extensively in quantum chemistry. For solids it is less accurate, however. In the present work, the electronic band structure of compounds and ternary alloys has been studied by DFT which is more modern and probably more powerful with respect to HF approximation.

2.2.3 Level 3: Density Functional Theory

Density Functional Theory formally established in 1964 by two theorems due to Hohenberg and Kohn [40]. The traditional formulation of these theorems is as follows:

- There is a one-to-one correspondence between the ground-state density $\rho(\vec{r})$ of a many-electron system (atom, molecule, solid) and the external potential, V_{ext} . An immediate consequence is that the ground-state expectation value of any observable quantity, \hat{O} , is a unique functional of the exact ground-state electron density

$$\langle \Psi | \hat{O} | \Psi \rangle = \hat{O}[\rho] \quad (2.11)$$

- Second theorem: For \hat{O} being the Hamiltonian, the ground-state total energy functional ($H[\rho] \equiv E_{V_{ext}}[\rho]$) is of the form:

$$E_{V_{ext}}[\rho] = \underbrace{\langle \Psi | \hat{T} + \hat{V} | \Psi \rangle}_{F_{HK}[\rho]} + \langle \Psi | \hat{V}_{ext} | \Psi \rangle \quad (2.12)$$

or

$$E_{V_{ext}}[\rho] = F_{HK}[\rho] + \int \rho(\vec{r}) V_{ext}(\vec{r}) d\vec{r} \quad (2.13)$$

where, the Hohenberg-Kohn density functional $F_{HK}[\rho]$ is universal for any many-electron system. $E_{V_{ext}}[\rho]$ reaches its minimal value (equal to the ground-state total energy) for the ground state density corresponding to V_{ext} .

We do not prove these theorems here, but ponder a few implications of the three keywords, invertibility (one-to-one correspondence, $\rho \longrightarrow V_{ext}$), universality and variational access (minimal value).

- **Invertibility:** the one-to-one correspondence between ground-state density and external potential is intriguing. It is obvious that a given many-electron system has a unique external potential, which by the Hamiltonian (Eq. 2.2) and the Schrödinger equation yields a unique ground-state many particle wave function. From this wave function, the corresponding electron density is easily found. An external potential hence leads in a well-defined way to a unique ground-state density corresponding to it. But intuitively it looks like the density contains less information than the wave function. If this would be true, it would not be possible to find a unique external potential if only a ground-state density is given. The first theorem of Hohenberg and Kohn tells exactly that this is possible. The density contains as much information as the wave function does (i.e. everything you could possibly know about an atom, molecule or solid). All observable quantities can be

retrieved therefore in a unique way from the density only, i.e. they can be written as functionals of the density.

- Universality (the universality of $F_{HK}[\rho]$): Eq. 2.13 is easily written down by using the density operator, and supposing the ground-state density is known, the contribution to the total energy from the external potential can be exactly calculated. An explicit expression for the Hohenberg-Kohn functional, F_{HK} , is not known. But anyway, because F_{HK} does not contain information on the nuclei and their position, it is a universal functional for any many-electron system. This means that in principle an expression for $F_{HK}[\rho]$ exists which can be used for every atom, molecule or solid which can be imagined.
- variational access: the second theorem makes it possible to use the variational principle of Rayleigh-Ritz in order to find the ground-state density. Out of the infinite number of possible densities, the one which minimizes $E_{V_{ext}}[\rho]$ is the ground-state density corresponding to the external potential $V_{ext}(\vec{r})$. Of course, this can be done only if (an approximation to) $F_{HK}[\rho]$ is known. But having found ρ , all knowledge about the system is within reach. It is useful to stress the meaning of the energy functional $E_{V_{ext}}[\rho]$ once more. When it is evaluated for the ρ density corresponding to the particular V_{ext} for this solid, it gives the ground state energy. When it

is evaluated for any other density however, the resulting number has no physical meaning.

The practical procedure to obtain the ground state density of DFT was satisfied by Kohn and Sham equation published in 1965 [41]. In Kohn Sham equation, the correlation energy is defined as this part of the total energy which is present in the exact solution, but absent in the Hartree-Fock solution. The total energy functionals $E_e[\rho]$ and $E_{HF}[\rho]$ corresponding to the exact and Hartree-Fock Hamiltonian (Eq. 2.10) respectively, are:

$$E_e = T + V \tag{2.14}$$

and

$$E_{HF} = T_o + \underbrace{(V_H + V_x)}_V \tag{2.15}$$

Here T and V are the exact kinetic and electron-electron potential energy functionals, T_0 is the functional for the kinetic energy of a non-interacting electron gas, V_H stands for the Hartree contribution and V_x for the exchange contribution. By subtracting equation (2.15) from equation (2.14), the functional for the correlation contribution appears to be

$$V_c = T - T_0 \tag{2.16}$$

The exchange contribution to the total energy is defined as the part which is present in the Hartree-Fock solution, but absent in the Hartree solution. Obviously, with the Hartree functional given by

$$E_H = T_0 + V_H \quad (2.17)$$

It can be defined as

$$V_x = V - V_H \quad (2.18)$$

With this knowledge, we can rewrite the Hohenberg-Kohn functional in the following way

$$\begin{aligned} F_{HK} &= T + V + T_o - T_o \\ &= T_o + V + \underbrace{(T - T_o)}_{V_c} \end{aligned} \quad (2.19)$$

$$= T_o + V + V_c + V_H - V_H \quad (2.20)$$

$$= T_o + V_H + V_c + \underbrace{(V - V_H)}_{V_x} \quad (2.21)$$

$$= T_o + V_H + \underbrace{(V_x + V_c)}_{V_{xc}} \quad (2.22)$$

$$(2.23)$$

Here V_{xc} is the exchange-correlation energy functional. We don't know it formally, as it contains the difficult exchange and correlation contributions only. If we assume for a while that we do know V_{xc} , we can write explicitly the energy functional:

$$E_{V_{ext}}[\rho] = T_0[\rho] + V_H[\rho] + V_{xc}[\rho] + V_{ext}[\rho] \quad (2.24)$$

One could use now the second Hohenberg-Kohn theorem to find the ground state density, but then we would have won nothing by our transformation. Instead, one can interpret the above expression also as the energy functional of a non-interacting classical electron gas, subject to two external potentials: one due to the nuclei, and one due to exchange and correlation effects. The corresponding Hamiltonian (called the Kohn-Sham Hamiltonian) is

$$\widehat{H}_{KS} = \widehat{T}_0 + \widehat{V}_H + \widehat{V}_{xc} + \widehat{V}_{ext} \quad (2.25)$$

or

$$\widehat{H}_{KS} = -\frac{\hbar^2}{2m_e} \nabla_i^2 + \frac{e^2}{4\pi\epsilon_0} \int \frac{\rho(\vec{r}\vec{l})}{|\vec{r} - \vec{r}\vec{l}|} d\vec{r}\vec{l} + \widehat{V}_{xc} + \widehat{V}_{ext} \quad (2.26)$$

where, the exchange-correlation potential is given by the functional derivative

$$\widehat{V}_{xc} = \frac{\delta V_{xc}[\rho]}{\delta \rho} \quad (2.27)$$

The theorem of Kohn and Sham can now be formulated as follows: The exact ground-state density $\rho(\vec{r})$ of an N-electron system is

$$\rho(\vec{r}) = \sum_{i=1}^N \psi_i^*(\vec{r}) \psi_i(\vec{r}) \quad (2.28)$$

where, the single-particle wave functions $\psi_i(\vec{r})$ are the N lowest-energy solutions of the Kohn-Sham equation

$$\widehat{H}_{KS} \psi_i = \epsilon_i \psi_i \quad (2.29)$$

And now, we did won a lot. To find the ground-state density, one don't need to use the second Hohenberg-Kohn theorem any more, but one can rely on solving

familiar Schrödinger (like noninteracting single particle) equations. The alternative of using the regular Schrödinger equation, would have led to a far more difficult system of coupled differential equations, because of the electron-electron interaction. Be aware that the single-particle wave functions, $\psi_i(\vec{r})$, are not the wave functions of electrons. They describe mathematical quasi-particles, without a direct physical meaning. Only the overall density of these quasi-particles is guaranteed to be equal to the true electron density. Also the single-particle energies, ϵ_i , are not single-electron energies. Both the Hartree operator V_H and the exchange-correlation operator V_{xc} depend on the density $\rho(\vec{r})$, which in turn depends on the $\psi_i(\vec{r})$ which are being searched. This means that we are dealing with a self-consistency problem: the solutions, $\psi_i(\vec{r})$, determine the original equation (V_H and V_{xc} in H_{KS}), and the equation cannot be written down and solved before its solution is known. An iterative procedure (see Fig. 2.1) is needed to escape from this paradox. Some starting density ρ_o is guessed, and a Hamiltonian H_{KS1} is constructed with it. The eigenvalue problem is solved, and results in a set of ψ_i from which a density ρ_1 can be derived. Most probably ρ_o will differ from ρ_1 . Now ρ_1 is used to construct H_{KS2} , which will yield a ρ_2 , etc. The procedure can be set up in such a way that this series will converge to a density ρ_f which generates a H_{KSf} which yields as solution again ρ_f , this final density is then consistent with the Hamiltonian. The *Kohn – Sham* scheme described above was exact, apart from the preceding Born-Oppenheimer approximation, no

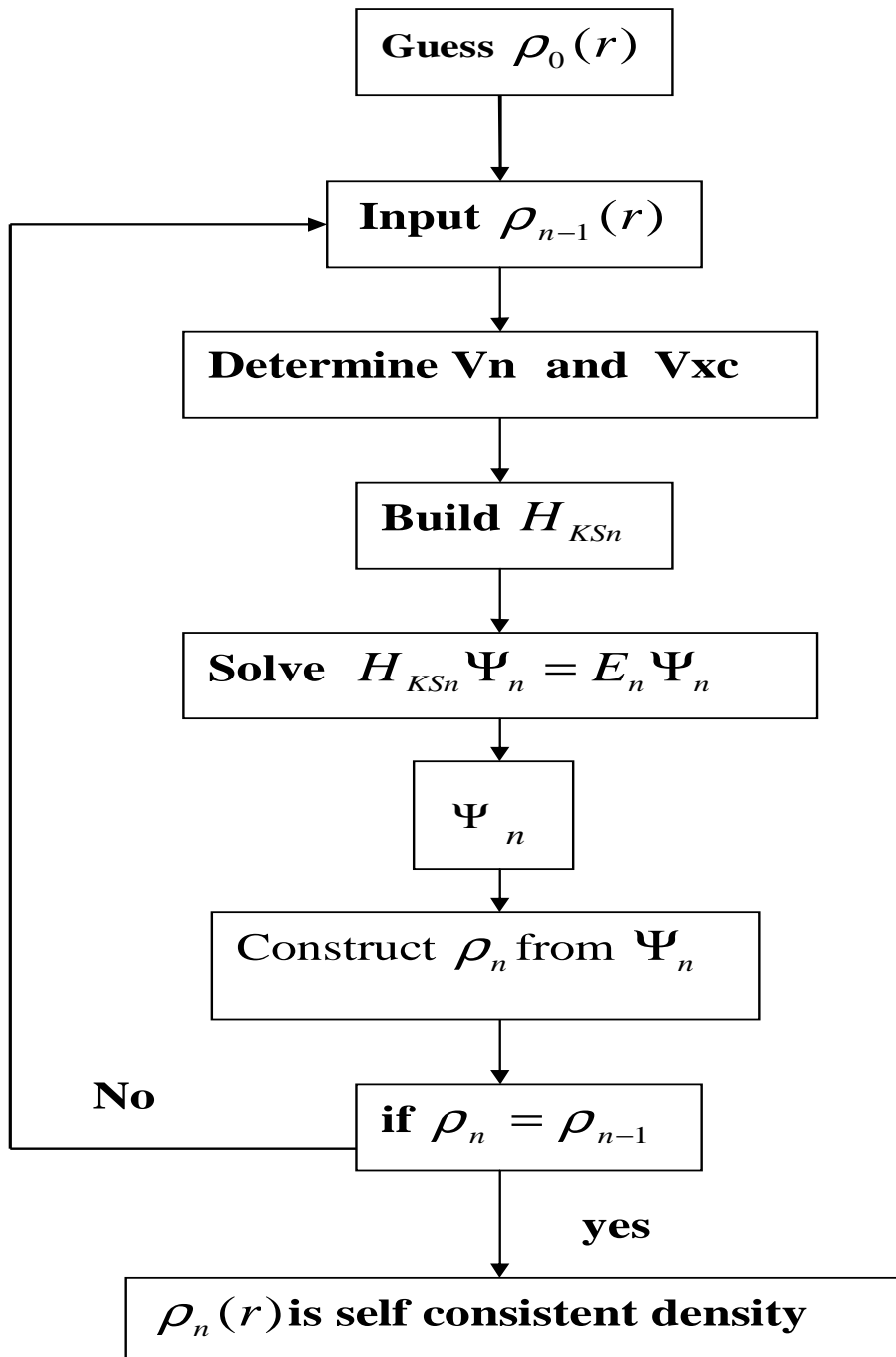


Figure 2.1: Flow chart for the n^{th} iteration in the self-consistent procedure to solve *Hartree – Fock* or *Kohn – Sham* equations

other approximations were made. But we neglected so far the fact that we do not know the exchange-correlation functional. It is here that approximations enter this theory. A widely used approximation - called the Local Density Approximation (LDA)- is to postulate that the exchange-correlation functional has the following form:

$$E_{xc}^{LDA} = \int \rho(\vec{r}) \epsilon_{xc}(\rho(\vec{r})) d\vec{r} \quad (2.30)$$

This postulate is somehow reasonable; it means that the exchange-correlation energy due to a particular density $\rho(\vec{r})$ could be found by dividing the material in infinitesimally small volumes with a constant density. Each such volume contributes to the total exchange correlation energy by an amount equal to the exchange correlation energy of an identical volume filled with a homogeneous electron gas, which has the same overall density as the original material has in this volume. No law of nature guarantees that the true E_{xc} is of this form, it is only a reasonable guess. By construction, LDA is expected to perform well for systems with a slowly varying density. But rather surprisingly, it appears to be very accurate in many other (realistic) cases too. A next logical step to improve on LDA is to make the exchange-correlation contribution of every infinitesimal volume not only dependent on the local density in that volume, but also on the density in the neighboring volumes. In other words, the gradient of the density will play a role. This approximation is therefore called the Generalized Gradient Approximation (GGA). Although GGA performs in general slightly better than

LDA, there are a few drawbacks. There is only one LDA exchange-correlation functional, because there is a unique definition for ϵ_{xc} . But there is some freedom to incorporate the density gradient, and therefore several versions of GGA exist (first drawback). Moreover, in practice one often fits a candidate GGA-functional with free parameters to a large set of experimental data on atoms and molecules. The best values for these parameters are fixed then, and the functional is ready to be used routinely in solids. Therefore such a GGA-calculation is strictly spoken not an ab-initio calculation, as some experimental information is used (second drawback). Nevertheless, there exist GGA's that are parameter free.

2.2.4 Level 4: Solving the equations

Irrespective whether one has used HF or DFT as level 2, 3 approximation, one ends up with an infinite set of one-electron equations of the following type:

$$\underbrace{\left(-\frac{\hbar^2}{2m_e} \nabla_m^2 + \frac{e^2}{4\pi\epsilon_o} \int \frac{\rho(\vec{r}')}{|\vec{r}' - \vec{r}|} d\vec{r}' + V_\alpha + V_{ext}\right)}_{\widehat{H}_{sp}} \psi_m(\vec{r}) = \epsilon_m \psi_m(\vec{r}) \quad (2.31)$$

here, m is an integer number that counts the members of the set, we call \widehat{H}_{sp} the single-particle Hamiltonian. For HF, V_α is the exchange operator. The ψ_m are true one-electron (or single-particle) orbital for HF. Exchange is treated exactly, but correlation effects are not included at all. They can be added only in elaborations on the HF-method. For DFT, V_α is the exchange-correlation operator, in the L(S)DA, GGA or another approximation. Exchange and correlation are both

treated, but both approximately. The ψ_m are mathematical single-particle orbital. The similarity between the Hartree-Fock and Kohn-Sham equations means that the same mathematical techniques can be used to solve them. ‘Solving’ in most methods means that we want to find the coefficients c_p^m needed to express ψ_m in a given basis set ϕ_p :

$$\psi_m = \sum_{p=1}^P c_p^m \phi_p \quad (2.32)$$

The wave functions ψ_m belong to a function space which has an infinite dimension, P is therefore in principle infinite. In practice one works with a limited set of basis functions. Such a limited basis will never be able to describe ψ_m exactly, but one could try to find a basis that can generate a function that is ‘close’ to ψ_m . Having chosen a basis (and hence a finite value for P) we realize that we can tackle the equations (2.31) as an eigenvalue problem. For a given m , substitute equation (2.32) in (2.31), and left-multiply with $\langle \phi_i |$ ($i = 1, \dots, P$).

$$\begin{pmatrix} \dots & \dots & \dots \\ \vdots & \langle \phi_i | \widehat{H}_{sp} | \phi_j \rangle - \epsilon \langle \phi_i | \phi_j \rangle & \vdots \\ \dots & \dots & \dots \end{pmatrix} \begin{pmatrix} c_1^m \\ \vdots \\ c_p^m \end{pmatrix} = \begin{pmatrix} 0 \\ \vdots \\ 0 \end{pmatrix} \quad (2.33)$$

We recognize here the matrix elements of the single-particle Hamiltonian in the basis states, and the overlap matrix elements S_{ij} . Remember that the overlap matrix is a unit matrix if the basis set is orthonormal. Diagonalization of the Hamiltonian matrix will lead to P eigenvalues and P sets of coefficients that

express each of the P eigenfunctions in the given basis (if more eigenfunctions are needed, P must be increased). The larger P , the better the approximation of the eigenfunction, but the more time-consuming the diagonalization of the matrix in equation (2.33).

2.3 Empirical Tight Binding Theory

The Empirical Tight-Binding method can be employed for calculating characteristics of both periodic and amorphous solids, as well as atomic clusters. The ETB approach works by replacing the many-body Hamilton operator with a parameterized Hamiltonian matrix and by solving the Schrödinger equation in an atomic-like set [47]. The set is not, in general, explicitly constructed, but it is atomic-like in that it has the same symmetry properties as the atomic orbitals. A small number of basis functions are usually used, those roughly corresponding to the atomic orbitals in the energy range of interest. For example, when modeling AlN , the 1s, 2s and 2p in Al and 1s in N can be neglected, and only 3s, 3p and 3d in Al , 2s and 2p in N orbitals can be considered. ETB approximation or Linear Combination of Atomic Orbitals (LCAO) is the method of solving the Schrödinger equation for a multiatomic system by expanding the electronic eigenstates of the effective one-electron Hamiltonian in a sum of atomic orbitals [47, 48]. In a periodic solid the use of Bloch's theorem [51] reduces the size of

the Hamiltonian to the number of orbitals per unit cell. This is a drastic simplification where the wave vector \vec{k} turns out to be a good quantum number. According to these facts the electron wave function can be written as follows:

$$|\psi_\mu(\vec{r})\rangle = \frac{1}{\sqrt{N}} \sum_{R_i} e^{i\vec{k} \cdot \vec{R}_i} |\phi_\mu(\vec{r} - \vec{R}_i)\rangle \quad (2.34)$$

where, $|\phi_\mu(\vec{r} - \vec{R}_i)\rangle$ is the atomic orbital at the i th atom at site R_i , μ corresponds to one of the atomic orbitals (s, p_x, p_y, p_z, \dots). This method enables the calculation of an approximate one-body Hamiltonian matrix whose eigenvalues are taken to approximate the allowed electronic energies and the eigenvectors are states. In the usual implementation of ETB calculations, the basis, $|\phi_\mu\rangle$, are taken to be orthonormal on the same site ($\langle\phi_\mu | \phi_\nu\rangle = \delta_{\mu\nu}$). The sum of the occupied energy eigenvalues is the attractive electronic contribution to the total energy. To compute the system (ions+electrons) energy a repulsive interaction must be added to the electronic part. ETB is the simplest approach enabling an estimate of the many-body forces characteristic of covalently bonded materials. Since ETB is simple and illustrative of many concepts in electronic structure of amorphous solids, it is considered to be good method to calculate the electronic band structure of ternary alloys. By considering a supercell module (large unit cell with periodic boundary condition) of an amorphous solid with N atoms and atomic coordinates, $(R_i)_{i=1}^N$, it is possible to view the $(R_i)_{i=1}^N$ as specifying a set of basis vectors for a crystal with a very large and topologically complex unit cell. Such a large unit cell possesses a band structure as does any periodic system.

But, since the cell is supposed to represent an amorphous system, it must be large to have credibility. The one body Hamiltonian matrix of the large system is then

$$H_{\mu\nu} = \frac{1}{N} \sum_{R_i, R_j} e^{i \vec{k} \cdot (\vec{R}_i - \vec{R}_j)} \langle \phi_\mu(\vec{r} - \vec{R}_i) | \widehat{H} | \phi_\nu(\vec{r} - \vec{R}_j) \rangle \quad (2.35)$$

where, \widehat{H} is the Hamiltonian operator. As the matrix elements in this representation depend in detail on the network topology, it is convenient to work with molecular coordinates specifying the interatomic hopping. The Hamiltonian matrix eigenvalue problem then reads the usual orthogonal eigenvalue problem as follows:

$$\widehat{H} | \psi_m \rangle = E_m | \psi_m \rangle \quad (2.36)$$

Where, the electronic eigenvalues are supposed to be approximated by E_m . For electronic density of state calculations or questions of the spectral signature of a defect, an exact diagonalization of Hamiltonian matrix is sufficient. But in general, since the orbitals on different sites are not orthogonal i.e. $\langle \phi_\mu | \phi_\nu \rangle \neq \delta_{\mu\nu}$, the Schrödinger equation (Eq. (2.36) leads to the secular determinant.

$$| H_{\mu\nu} - ES_{\mu\nu} | = 0 \quad (2.37)$$

For an energy value of E

$$S_{\mu\nu} = \langle \phi_\mu | \phi_\nu \rangle \quad (2.38)$$

is the overlapping matrices. For an arbitrary cluster of atoms the size of each of the matrices H and S is equal to the total number of orbitals. $H_{\mu\nu}$ and $S_{\mu\nu}$

become functions of \vec{k} and the solution of the secular equation generates the band structure $E(\vec{k})$.

In order to build the Hamiltonian matrix, the interactions between the orbitals (from Eq. 2.35 to Eq. 2.38) are obtained by either experimental measurements or first principles calculations as it is done in the present work. The solution of the secular equation given in Eq. 2.37 can easily produce the band structure of valence and conduction bands. One should keep in mind that the energy eigenvalues in the valence and conduction band regions should be equal to the corresponding eigenvalues, one got from the first principles calculations.

2.4 Computational Steps of the Work

In the present work, the total energy and the electronic band structure of *InN*, *InAs*, *InSb*, *AlN*, *AlAs*, *AlSb*, *GaN* and *GaAs* in zinc-blende phase has been calculated using first principles calculations based on DFT by means of full potential linearized augmented plane wave (FP-LAPW) method given in WIEN2k package [52]. In this method the unit cell is divided into (I) non-overlapping atomic spheres (muffin tin spheres (MT)) and (II) an interstitial region. In two types of regions different basis sets are used:

- Inside the atomic sphere, of radius R_{MT} , a linear combination of radial

functions times spherical harmonics $Y_{lm}(r)$ is used. In Eq. (2.32)

$$\phi_{K_n} = \sum_{lm} (A_{lm, K_n} u_l(r, E_l) + B_{lm, K_n} \dot{u}_l(r, E_l)) Y_{lm}(\hat{r}) \quad (2.39)$$

Where, $u_l(r, E_l)$ is the regular solution of the radial Schrödinger equation for energy E_l and the spherical part of the potential inside the sphere, $\dot{u}_l(r, E_l)$ is the energy derivative of u_l evaluated at the same energy E_l . A linear combination of these two functions constitute the linearization of the radial function; the coefficients A_{lm} and B_{lm} are functions of K_n determined by requiring that this basis function matches (in value and slope) each plane wave (PW) of the corresponding basis function of the interstitial region. The radial functions u_l and \dot{u}_l are obtained by numerical integration of the radial Schrödinger equation on a radial mesh inside the sphere.

- in the interstitial region a plane wave expansion is used.

$$\phi_{K_n} = \frac{1}{\sqrt{w}} e^{iK_n \cdot r} \quad (2.40)$$

Where, $\vec{K}_n = \vec{k} + \vec{K}_n$; \vec{K}_n are reciprocal lattice vectors and k is the wave vector inside the first Brillouin zone. Each plane wave is augmented by an atomic-like function in every atomic sphere.

The solutions to the Kohn-Sham equations are expanded in this combined basis set of LAPW's according to the linear variation method

$$\Psi_k = \sum_n c_n \phi_{K_n} \quad (2.41)$$

and the coefficients c_n are determined by the RayleighRitz variational principle. The convergence of this basis set is controlled by a cutoff parameter $R_{mt}K_{max}$ value, where R_{mt} is the smallest atomic sphere radius in the unit cell and K_{max} is the magnitude of the largest K vector in Eq. (2.41). In the present work, this parameter was taken to be 8–12. In the MT spheres, the l- expansion of the non-spherical potential and charge density is truncated at l= 12 for the wave function of the binary compounds studied in this work. The number of plane waves used in the expansion of Eq. 2.41 are 1240, 2300, 2799, 381, 2346, 1852, 1065 and 2150 for *InN*, *InAs*, *InSb*, *AlN*, *AlSb*, *AlAs*, *GaN* and *GaAs*, respectively. The iteration process of all the total energy calculation (Fig. 2.1) has been repeated until the calculated total energy of the considered compound converged to less than (0.1) mRy.

In the present work, the total energy of the system has been calculated as a function of the separation between the atoms and the positions of the electrons. The total energy has been defined in WIEN2k by the addition of the repulsion energy of nuclei to the total electronic energy. The variation of the total energy values with respect to the different sized unitcells has been fitted to Murnghan’s equation [53] to find out the equilibrium lattice constant of the structures considered in this work.

In this work, Eq. (2.31) has been solved in the muffin tin spheres and interstitial regions numerically using WIEN2k program. The continuity of the wave

function and its derivative for all the taken k vectors were satisfied at the boundary between the muffin tin spheres and interstitial regions. The resulted wave function has been used in the DFT cycle (Figure 2.1) until the SC wave function has been found. The band structure of the compounds considered in this work has been calculated by the final wave function of the SC cycle. It is widely used in the literature that the standard DFT calculations can produce the band structure of the semiconductor compounds correctly, but give smaller energy gaps at high symmetry points compared to experimental results. On the other hand, the time consuming is very important handicap in performing the first principles calculations on large systems and alloys. ETB is fairly straightforward and easy to implement for large systems and alloys. It provides reliable accuracy in a very short calculational time. In the present work, to study the band bowing of III (*In, Al*) - V (*N, As, Sb*) alloys the advantages of the DFT and ETB calculations have been considered to be combined. Therefore electronic structure calculations of compounds by DFT have been followed by ETB.

First, the band gaps of the compounds calculated by DFT/FP-LAPW-GGA have been corrected empirically using experimental values. Secondly, the ETB interaction energy parameters have been derived from the eigenvalues of DFT/FP-LAPW-GGA calculations.

Slater- Koster model of ETB was extensively used in the literature with minimal sp^3 [54] basis and interaction only between nearest neighbor atoms to find out

valence band energy dispersion of compounds correctly. But this model fails to calculate the indirect gap of semiconductors satisfactorily, especially at X point. The underestimated band structures calculated by ETB can be improved either including the interatomic interactions beyond the nearest neighbors (second nearest, etc..) or higher atomic states on each atom. In the present work, we are convinced that the second way is the most appropriate physically, and most useful practically in semiconductors. Adding distant interactions (like second nearest neighbor) introduces extra parameters for which we don't know the variations with distance (they don't follow the square distance law $1/d^2$), while the inclusion of higher states proceeds naturally. Vogl, *et al* [55] had found that supplementing the sp^3 basis by a single excited s- state on each atom, called the s^* -state, was sufficient to rectify this shortcoming of the conduction bands. On the other hand, the successfully reproduced indirect energy gaps of *III - V* compounds by pseudopotential method [56] showed that, the influence of the d orbitals to the lowest conduction state is large at Γ , X and L points. By considering this fact, in the present nearest neighbor ETB calculations, the excited first and second d orbitals, d_1 (d_{z^2}) and d_2 ($d_{x^2-y^2}$) are taken into account as well as sp^3 .

The Hamiltonian matrix of sp^3d^2 interaction orbitals with 12×12 dimension is given in Fig. 2.2. Since all the orbitals in sp^3d^2 set have the same symmetry group, the first nearest neighbor interactions between anion and cation are defined by

only thirteen different types of ETB energy parameters. They are E_{sa} , E_{pa} , E_{da} , E_{sc} , E_{pc} , E_{dc} , V_{ss} , V_{xx} , V_{xy} , V_{scpa} , V_{sapc} , V_{dapc} , V_{dcpa} . Here, the d-d and s-d orbital interaction energies (V_{dd} and V_{sd}) between the cation and the anion are considered to be small and neglected. In ETB Hamiltonian the interaction energy parameters are weighted by complex constants, g_0, g_1, g_2, g_3 , resulted from the tetrahedrally coordinated four nearest neighbor atoms in Eq. (2.35). The g_0, g_1, g_2 and g_3 can be formulated explicitly as follows:

$$\begin{aligned}
g_0(\vec{k}) &= \cos\left(\frac{k_x a}{4}\right) \cos\left(\frac{k_y a}{4}\right) \cos\left(\frac{k_z a}{4}\right) - i \sin\left(\frac{k_x a}{4}\right) \sin\left(\frac{k_y a}{4}\right) \sin\left(\frac{k_z a}{4}\right) \\
g_1(\vec{k}) &= -\cos\left(\frac{k_x a}{4}\right) \sin\left(\frac{k_y a}{4}\right) \sin\left(\frac{k_z a}{4}\right) + i \sin\left(\frac{k_x a}{4}\right) \cos\left(\frac{k_y a}{4}\right) \cos\left(\frac{k_z a}{4}\right) \\
g_2(\vec{k}) &= -\sin\left(\frac{k_x a}{4}\right) \cos\left(\frac{k_y a}{4}\right) \sin\left(\frac{k_z a}{4}\right) + i \cos\left(\frac{k_x a}{4}\right) \sin\left(\frac{k_y a}{4}\right) \cos\left(\frac{k_z a}{4}\right) \\
g_3(\vec{k}) &= -\sin\left(\frac{k_x a}{4}\right) \sin\left(\frac{k_y a}{4}\right) \cos\left(\frac{k_z a}{4}\right) + i \cos\left(\frac{k_x a}{4}\right) \cos\left(\frac{k_y a}{4}\right) \sin\left(\frac{k_z a}{4}\right) \quad (2.42)
\end{aligned}$$

where, the coefficients y and k present in front of some of the entries of the Hamiltonian matrix are $-\frac{1}{\sqrt{3}}$ and $\frac{2}{\sqrt{3}}$, respectively. The letters a and c in front of the orbitals and the energy parameters stand for anion and cation, respectively. In ETB calculations of compounds, the solution of the secular equation at Γ and X symmetry points gives nine independent equations:

$$\Gamma_{1c} + \Gamma_{1v} = E_{sa} + E_{sc} \quad (2.43)$$

$$\Gamma_{15c} + \Gamma_{15v} = E_{pa} + E_{pc} \quad (2.44)$$

$$V_{ss} = -\sqrt{\left(\left(\frac{\Gamma_{1c} - \Gamma_{1v}}{2}\right)^2 - \left(\frac{E_{sa} - E_{sc}}{2}\right)^2\right)} \quad (2.45)$$

$$V_{xx} = \sqrt{\left(\left(\frac{\Gamma_{15c} - \Gamma_{15v}}{2}\right)^2 - \left(\frac{E_{pa} - E_{pc}}{2}\right)^2\right)} \quad (2.46)$$

$$V_{xy} = \sqrt{\left(\left(\frac{X_{5c} - X_{5v}}{2}\right)^2 - \left(\frac{E_{pa} - E_{pc}}{2}\right)^2\right)} \quad (2.47)$$

$$V_{pcsa} = \sqrt{\left(\frac{(E_{sa} - X_{1c})(E_{sa} - X_{1v})(E_{pc} + E_{da} - X_{1v} - X_{1c})}{(E_{sa} - E_{da})}\right)} \quad (2.48)$$

$$V_{pasc} = \sqrt{\left(\frac{(E_{sc} - X_{3c})(E_{sc} - X_{3v})(E_{pa} + E_{dc} - X_{3v} - X_{3c})}{(E_{sc} - E_{dc})}\right)} \quad (2.49)$$

$$V_{d1apc} = \sqrt{\frac{3}{4} \left(\frac{(E_{da} - X_{1c})(E_{da} - X_{1v})(E_{pc} + E_{sa} - X_{1v} - X_{1c})}{(E_{da} - E_{sa})}\right)} \quad (2.50)$$

$$V_{d1cpa} = \sqrt{\frac{3}{4} \left(\frac{(E_{dc} - X_{3c})(E_{dc} - X_{3v})(E_{pa} + E_{sc} - X_{3v} - X_{3c})}{(E_{dc} - E_{sc})}\right)} \quad (2.51)$$

The interaction energy parameters of ETB have been derived from the eigenvalues of FP-LAPW studied for the compounds at the first stage of the work. The above equations have been solved for each compound by a simulating program which also finds the remaining four energy parameters (E_{sa} , E_{pa} , E_{da} , E_{dc}) by minimizing the difference between the eigenvalues of ETB and FP-LAPW. After finding the energy parameters, the ETB Hamiltonian matrix (Fig. 2.2) is built for sp^3d^2 basis and nearest neighbor interactions. The Hamiltonian matrix is diagonalized along the chosen directions to reproduce the band structure of the compounds.

Since the application of first principles calculational methods on large scaled systems such as alloys with different concentration of constituents is limited in

	sa	xa	ya	za	d1a	d2a	sc	xc	yc	zc	d1c	d2c
sa	Esa	0	0	0	0	0	Vss*g0	Vsapc*g1	Vsapc*g2	Vsapc*g3	0	0
xa	0	Epa	0	0	0	0	g1*-Vscpa	Vxx*g0	Vxy*g3	Vxy*g2	Vxad1c*g1	y\xad1c*g1
ya	0	0	Epa	0	0	0	g2*-Vscpa	Vxy*g3	Vxx*g0	Vxy*g1	g2*-Vxad1	y\xad1c*g2
za	0	0	0	Epa	0	0	g3*-Vscpa	Vxy*g2	Vxy*g1	Vxx*g0	0	k\xad1c*g3
d1a	0	0	0	0	Eda	0	0	Vd1axc*g1	g2*-Vd1axc	0	Vd1d1g0	0
d2a	0	0	0	0	0	Eda	0	y\vd1axc*g1	y\vd1axc*g2	k\vd1axc*g3	0	Vd1d1g0
sc	Vss*g0	g1*-Vscpa	g2*-Vscpa	g3*-Vscpa	0	0	Esc	0	0	0	0	0
xc	Vsapc*g1	Vxx*g0	Vxy*g3	Vxy*g2	Vd1axc*g1	y\vd1axc*g1	0	Epc	0	0	0	0
yc	Vsapc*g2	Vxy*g3	Vxx*g0	Vxy*g1	g2*-Vd1axc	y\vd1axc*g2	0	0	Epc	0	0	0
zc	Vsapc*g3	Vxy*g2	Vxy*g1	Vxx*g0	0	k\vd1axc*g3	0	0	0	Epc	0	0
d1c	0	Vxad1c*g1	g2*-Vxad1	0	Vd1d1g0	0	0	0	0	0	Edc	0
d2c	0	y\xad1c*g1	y\xad1c*g2	k\xad1c*g3	0	Vd1d1g0	0	0	0	0	0	Edc

Figure 2.2: The ETB Hamiltonian matrix for the sp^3d^2 model.

Figure 2.2: The ETB Hamiltonian matrix for the sp^3d^2 model.

time, the semiempirical or empirical methods are required to calculate the electronic band structure of alloys for full range of the compositions. In the present work, the electronic band structure of ($A_{1-x}B_xC$ and AB_xC_{1-x}) type ternary alloys composed of III-V elements has been calculated by ETB for the total range of x ($0 < x < 1$). The unit cells of the ternary alloys are defined by Vegard's law [57] as follows:

$$a_{AB_xC_{1-x}} = (x)a_{AB} + (1-x)a_{AC} \quad (2.52)$$

or

$$a_{A_{1-x}B_xC} = (1-x)a_{AC} + (x)a_{BC} \quad (2.53)$$

where, $a_{AB_xC_{1-x}}$, $a_{A_{1-x}B_xC}$, a_{AC} , a_{BC} and a_{AB} are the lattice constants of the alloys and compounds considered in this work, respectively. Since only the nearest neighbor interactions are taken into account, the self energy parameters (Esa, Esc, Epa, Epc, Eda, and Edc) of the corresponding III (*In, Al, Ga*) - V (*N, As, Sb*) group elements are included in the present ETB calculations directly. The other ETB energy parameters (Vss, Vxx, Vxy, Vscpa, Vsapc, Vdapc, Vdcpa) needed for the electronic band structure calculations of alloys have been obtained from those of corresponding compounds using Vegard's law [57]. The concentration dependent interaction energy parameters can be formulated by r^{-2} scaling method [48]; particularly, the Vss energy parameter can be written as follows:

$$V_{SSAB_xC_{1-x}} = \frac{(x)(d_{AB}^2 \times V_{SSAB}) + (1-x)(d_{AC}^2 \times V_{SSAC})}{d_{AB_xC_{1-x}}^2} \quad (2.54)$$

or

$$V_{ssA_{1-x}B_xC} = \frac{(1-x)(d_{AC}^2 \times V_{ssAC}) + (x)(d_{BC}^2 \times V_{ssBC})}{d_{A_{1-x}B_xC}^2} \quad (2.55)$$

where, d_{AC}^2 , d_{BC}^2 , d_{AB}^2 , $d_{AB_xC_{1-x}}^2$ and $d_{A_{1-x}B_xC}^2$ are the bond length square of the binary compounds and the alloys, respectively. The rest of the energy parameters of ETB for the alloys considered in this work are calculated using similar formulations. The ETB Hamiltonian matrix of the alloys is built for sp^3d^2 basis and nearest neighbor interactions using the same method defined for the compounds. The Hamiltonian matrix is diagonalized along the chosen directions to find out the concentration dependent eigenvalues of the alloys. Finally, the variation of the fundamental band gap energy (E_g^Γ) of the alloys has been studied as a function of concentration (x) because of the importance of the band gap engineering. The bowing parameter, b, which shows the deviation of the energy gap (E_g^Γ) from linearity has been calculated by the best fit of our results to the following expression:

$$E_{g_{AB_xC_{1-x}}}^\Gamma(x) = xE_{g_{AB}}^\Gamma + (1-x)E_{g_{AC}}^\Gamma - bx(1-x) \quad (2.56)$$

or

$$E_{g_{A_xB_{1-x}C}}^\Gamma(x) = xE_{g_{AC}}^\Gamma + (1-x)E_{g_{BC}}^\Gamma - bx(1-x) \quad (2.57)$$

Here, $E_{g_{AB}}^\Gamma$, $E_{g_{AC}}^\Gamma$, $E_{g_{AB_xC_{1-x}}}^\Gamma$ and $E_{g_{A_xB_{1-x}C}}^\Gamma$ are the fundamental band gap energies of the compounds and alloys considered in this work, respectively.

CHAPTER 3

THE ELECTRONIC STRUCTURE OF InN, InAs AND InSb COMPOUNDS

3.1 Introduction

There is currently considerable interest in compounds of *In* with Nitrogen, Arsenic and Antimony, because of their optical and high temperature device applications. Among these compounds, *InN* is a highly potential material for the fabrication of high speed heterojunction transistors [1] and low cost solar cells with high efficiency [2]. Pure *InN* was predicted to have the lowest effective mass for electrons in all the III-nitride semiconductors [1] which lead to high mobility and high saturation velocity. Recently, several groups have grown high quality hexagonal (*w-InN*) and zinc-blende (*c-InN*) structural *InN* films by modern growth techniques, such as metal organic chemical vapor deposition (MOVPE) and plasma - assisted molecular beam epitaxy (MBE) [58–63]. The *w-InN* and *c-InN* films have been mostly grown on sapphire and GaAs (or Si, GaP) substrates, respectively. In these works [58–62], a buffer layer, particularly, *AlN* or *InAs* has been usually grown on the substrate to improve the quality of the *InN*

films. In a very recent work [63], the *c-InN* has been grown on r-plane sapphire successfully without the use of additional buffer layer. The growth of *w-InN* and *c-InN* films have been characterized by many techniques such as, X-ray Diffraction, Raman spectra, reflection high energy electron diffraction (RHEED). The photoluminescence (PL) spectra of high quality *w-InN* films have illustrated that the band gap energy of *InN* is smaller than the commonly accepted value of 1.9 eV [64]; it is around 0.65-0.90 eV [58, 59]. The recent experimental works on *c-InN* have mainly focused on the characterization of the films [60, 61, 62, 63]. The band gap energy of *c-InN* films has not been reported experimentally, but it has been found around 0.44-0.74 eV by the results of ab-initio calculations [65, 66]. These newly reported values of *w-InN* and *c-InN* are compatible with the wavelength of the optical fiber. Therefore, the *w-InN* and *c-InN* films will have very important potential to fabricate high speed laser diodes (LDs) and photodiodes (PDs) in the optical communication systems.

The other two compounds of *In*, *InAs* and *InSb* are interesting narrow gap semiconductors from the point of view of optical spectroscopy and optoelectronic applications [15]. Since *InAs* has a high electron mobility it may prove an important material for use in high speed electronics [11, 12]. The high quality *InAs* material has been grown with certain advantages by different growth techniques such as liquid phase epitaxy (LPE) [67], MBE [67–70], and MOCVD [26, 67]. The quality of grown doped [67] and undoped [26, 68–70] *InAs* materials has been

appraised by mainly PL spectroscopy [26, 67–74] at different temperatures. In the works on undoped homoepitaxial *InAs* (i.e. *InAs* / *InAs*), the energy of the first PL peak which corresponds to the band gap of *InAs* has been reported in the range of 399-418 meV at low temperatures (T= 4.2- 10 K). The band gap of undoped heteroepitaxial *InAs* has been measured to be 416 meV and 399 meV at 4.6 K for the GaAs and Si substrates, respectively [68]. In Ref. [26], the energy of the first infrared-PL peak has been reported as 415 meV at 10 K. In an early work, Dixon and Ellis [75] measured the band gap of *InAs* as 420 meV at 18 K by transmission experiment. In another early work given in Ref. [76], the band gap of *InAs* is measured to be 0.41 eV at 0 K by direct interband magneto-optical transitions. The calculated band gap value of *InAs* by first principles [77] and empirical [78–82] methods are all in the range of 0.37-0.42 eV.

The other compound of *In*, *InSb*, calls attention to have the smallest energy gap of any of the binary III-V materials. This property often allows the fabrication of infrared imaging systems, free space communications, and gas phase detection systems [16, 17]. There are many reports on the growth of *InSb* by MBE [83] and MOCVD [26] techniques. In a recent work [84], good quality *InSb* has been also grown by LPE technique. *GaAs*, *Si* and *InSb* (bulk like) have been mostly used substrates in all growth works. The possible lattice-mismatching between *InSb* and substrate in heteroepitaxial growths has been tried to be removed by the growth of buffer layers such as *InSb* and *AlSb* [83] on the substrate. The

quality of grown homoepitaxial *InSb* (*InSb/InSb*) materials has been analyzed by mainly PL [26] and infrared spectra [84] measured at different temperatures. In Ref. [26] the energy of the first PL peak which corresponds to the band gap of *InSb* has been reported as 235 meV at 10 K. At the same temperature, the energy gap of *InSb* corresponds to infrared spectra has been measured to be 0.23 eV [84]. In Ref. [74], the direct band gap of *InSb* was given as 0.235 and 0.23 eV at 1.8 and 77 K, respectively. Rowell [85] measured the band gap value of *InSb* as 235 meV by infrared-PL at 5.1 K. In an early work given in Ref. [76], the band gap of *InSb* measured to be 0.24 eV at 0 K by direct interband magneto-optical transitions. In their experimental works, Littler and co-workers [86] measured the band gap energy of *InSb* as 0.2352 eV. In a very recent work [87], the direct band gap of *InSb* has been measured to be 0.18 eV. In the literature, the band gap of *InSb* has been calculated to be in the range of 0.18-0.26 eV by self consistent pseudopotential (PP) [88], nonlocal PP [78], tight binding [79], empirical pseudopotential (EPP) [80], relativistic self consistent linear muffin tin orbitals (LMTO) [89], density functional theory-local density approximation (DFT-LDA) [77, 90] and DFT-generalized Kohn Sham scheme [91] methods.

In the present work, the electronic band structures of *InN*, *InAs* and *InSb* have been calculated by empirical tight binding (ETB) method. The aim of this work is to derive the energy parameters of ETB providing well defined valence

bands and energy gaps for InN , $InAs$ and $InSb$. Therefore these energy parameters can be used for the electronic band structure calculations of large sized systems, such as the alloys of these compounds. The ETB energy parameters of the compounds based on the present first principles calculations are listed in Table 3.1. The electronic band structures of InN , $InAs$ and $InSb$ calculated by both DFT and ETB are separately discussed in the following sections and the results are concluded in the last chapter.

Table 3.1: Empirical matrix elements of the sp^3d^2 Hamiltonian in eV.

	InN	$InAs$	$InSb$
E_{sa}	-11.6558	-7.9244	-5.5942
E_{sc}	-2.6424	-2.8927	-3.2074
E_{pa}	4.6235	0.0000	0.0000
E_{pc}	4.8241	3.7660	2.8711
E_{da}	15.7403	9.3469	7.7705
E_{dc}	12.6942	7.7964	5.9425
V_{ss}	-5.8787	-5.1076	-4.4532
V_{xx}	5.0545	0.7172	0.2715
V_{xy}	7.3168	3.6286	2.9182
V_{pcsa}	0.8742	4.1592	4.0969
V_{pasc}	4.8020	3.4948	2.8601
V_{dapc}	4.1776	4.7535	4.1220
V_{dcpa}	0.0000	0.1638	0.2738

3.2 The results

3.2.1 InN

The zinc-blende structure of InN is characterized by the lattice constant, a . At the first stage of the work, the equilibrium value of a is determined by calculating total energy of InN by FP-LAPW for a set of volumes and fitting these to the Murnaghan equation [53]. We have adopted the value of 0.95 \AA for In and 0.87 \AA for N as the MT radii. The electronic configuration of InN is $In: Kr (4d^{10}5s^25p^1)$ and $N: He (2s^22p^3)$. In the calculations, the electrons of In in $(1s^22s^22p^63s^23p^63d^{10}4s^24p^64d^{10})$ are defined as the core electrons and distinguished from the valence electrons of In in $(5s^25p^1)$. Similarly, the inner shell electrons of N in $(1s^2)$ are distinguished from the valence band electrons of N in $(2s^22p^3)$ shell. The curve of the total energy versus the lattice volume is shown in Fig. 3.1. The equilibrium lattice constant of $c-InN$ is calculated to be 4.967 \AA . The present lattice constant of $c-InN$ is given in Table 3.2 together with the experimental and other calculated lattice constant values of $c-InN$ presented in the literature. The present lattice constant of $c-InN$ (4.967 \AA) is found to be very close to the experimental result of 4.97 \AA [60]; it is only 0.3% smaller than the other experimental results 4.98 [106] and 4.986 [63] \AA . On the other hand, our lattice constant is also close to the lattice constant values of 4.968 [105], 4.964 [104], 5.017 [66], and 5.004 [97] calculated by DFT-Local Density Approximation

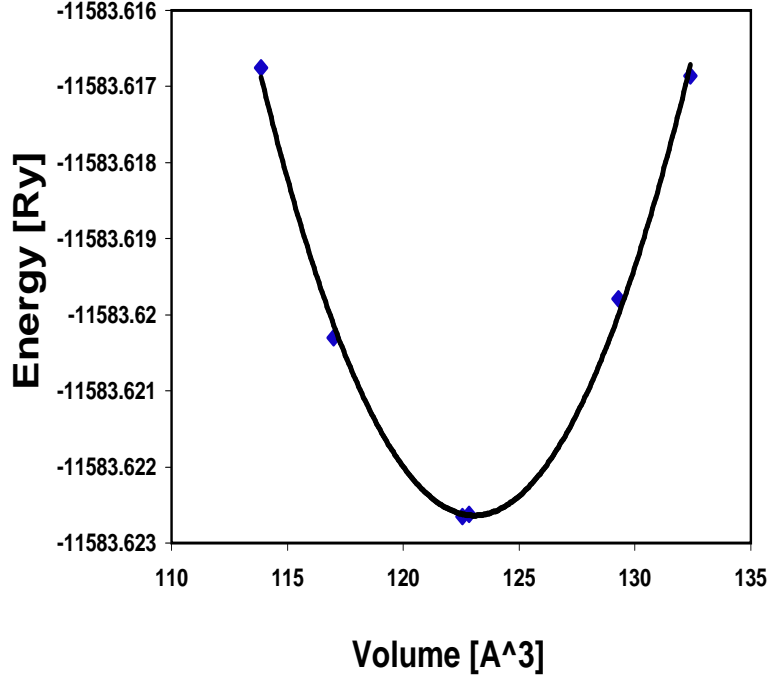


Figure 3.1: Total energy of *c-InN* versus the lattice volume.

(LDA). The present lattice constant is approximately 0.34% greater than the other value of 4.95 Å calculated by (LMTO) [92], and pseudopotential plane wave (PPPW)-GG approximation [65, 93]. Another lattice constant value of 5.067 Å [104] calculated by DFT within GGA is greater than the present value by 2%. The present lattice constant is less than the value (5.03 Å) [103] of FP-LAPW by 1.25%. With respect to the lattice constant values (4.92 and 4.929 Å) of FP-LMTO [96, 102] our result is high by (0.8-0.95)%. The values of a calculated by PP [94, 100] are very close to our result; the discrepancy is about (0.06-0.32)%. But the discrepancy is 0.7% with respect to the corrected lattice constant value of another PP calculations [95].

Table 3.2: The theoretical and experimental lattice constant values (a_{th}, a_{exp}) in \AA for InN , $InAs$ and $InSb$ in cubic phase.

<i>Compound</i>	a_{th}	a_{exp}
<i>InN</i>	4.967 ^a , 4.95 ^{b,c,d} (4.97, 5.05) ^e 4.932 ^f , 4.929 ^g 4.953 ^h , (5.004, 5.109) ⁱ 4.974 ^j , 5.01 ^k 4.983 ^l , 5.06 ^m 5.017 ⁿ , 4.92 ^o 5.03 ^p , (4.964, 5.067) ^r 4.968 ^s	4.98 ^t , 4.97 ^u 4.986 ^w
<i>InAs</i>	6.194 ^a , 5.906 ^{b'} , 5.85 ^{c'} (6.063, 5.94) ^{d'}	6.058 ^{e'} , 6.036 ^{f'} 6.06 ^{g'}
<i>InSb</i>	6.643 ^a 6.34 ^{b''} , 6.36 ^{c''} (6.34, 6.464) ^{d''} 6.42 ^{e''} , 6.478 ^{f''}	6.4782 ^{h''} , 6.47937 ^{i''} 6.49 ^{j''}

^apresent work, ^bRef. [92], ^cRef. [65], ^dRef. [93], ^eRef. [94], ^fRef. [95], ^gRef. [96],
^hRef.20 in Ref. [95], ⁱRef. [97], ^jRef. [98], ^kRef. [99], ^lRef. [100], ^mRef. [101],
ⁿRef. [66], ^oRef. [102], ^pRef. [103], ^rRef. [104], ^sRef. [105], ^tRef. [106], ^uRef.
[60], ^wRef. [63], ^{b'}Ref. [114], ^{c'}Ref. [116], ^{d'}Ref. [115], ^{e'}Ref. [111], ^{f'}Ref. [112],
^{g'}Ref. [113], ^{b''}Ref. [120], ^{c''}Ref. [114], ^{d''}Ref. [115], ^{e''}Ref. [121], ^{f''}Ref. [122],
^{h''}Ref. [117], ^{i''}Ref. [118], ^{j''}Ref. [119]

At the second stage of the work, the FP-LAPW method within the framework of the DFT has been employed to calculate the band structure of *c-InN*. Since, this work is planned to be extended the bowing parameter calculations of alloys correspond to *InN* in the next chapter, we have focused mainly on the energy gaps at high symmetry points. It is found that, band gap of *InN* is direct in zinc-blende phase. Furthermore, the variation of energy bands is in agreement with the results of previous reports [65, 66, 92, 97, 107]. The present band edge at Γ point is non parabolic as it was reported in these works. Since we are unaware of reports of experimental investigations of the electronic properties of *c-InN*, we couldn't compare the present band gap values with the experimental facts. But, the present band gap at Γ point (E_g^Γ) is found to be very small (-0.012 eV) with respect to the values given by first principles calculations [65, 66]. The similar negative direct band gap energies [95, 97, 101, 103] and small positive ones [92, 99] were reported before in the literature. In the present work, the calculated negative direct energy gap originated from DFT calculations has been adjusted to the value of 0.59 eV by addition of necessary energy corresponding to the effect which is not included in the calculations initially. The half of the energy difference between 0.59 eV and the present direct band gap is added to the conduction and valence band state energies equally in the same manner defined in Ref. [108]. Similarly, the negative value of E_g^Γ in Ref. [92] and the small value of E_g^Γ in Ref. [65] have been corrected by inclusion of some external potentials and

quasiparticle corrections, respectively. In the present work, the adjusted direct band gap value of 0.59 eV is taken from Ref. [65]. The same direct band gap value has been used in a very recent EPP calculations of InN [107]. The direct band gap value of 0.59 eV has been decided by the feedback calculations; the adjusted direct band gap of $c-InN$ has been tested by electronic band structure calculations of $c-In_xGa_{1-x}N$ alloys. The direct band gap of $In_xGa_{1-x}N$ alloy is calculated to be 3.198, 3.065, 2.967 and 2.647 eV for the In concentrations of 0.03, 0.07, 0.10 and 0.20, respectively. These present direct band gap values of $c-In_xGa_{1-x}N$ alloys are found to be very close to the direct band gap values of 3.2, 3.1, 3.0 and 2.875 eV which are measured by PL spectra of $c-In_xGa_{1-x}N$ films for the same concentrations of In at K [109]. In these feedback calculations, the ETB method has been employed and the corresponding energy parameters have been derived from the present eigenvalues of FP-LAPW with respect to the adjusted direct band gap of InN . The ETB energy parameters of GaN used in the present calculations are present in sec. 6.2.1.

Since the present energy parameters of ETB in feedback calculations produce the experimental direct band gap energies of $c-In_xGa_{1-x}N$ alloys for different concentration of In we have surely adjusted the direct band gap value of $c-InN$ to 0.59 eV. The adjusted energy band structure of $c-InN$ by FP-LAPW is shown in Fig. 3.2. Table 3.3 gives the important features of the present and previously reported band structures for $c-InN$ at high symmetry points. The energy gaps

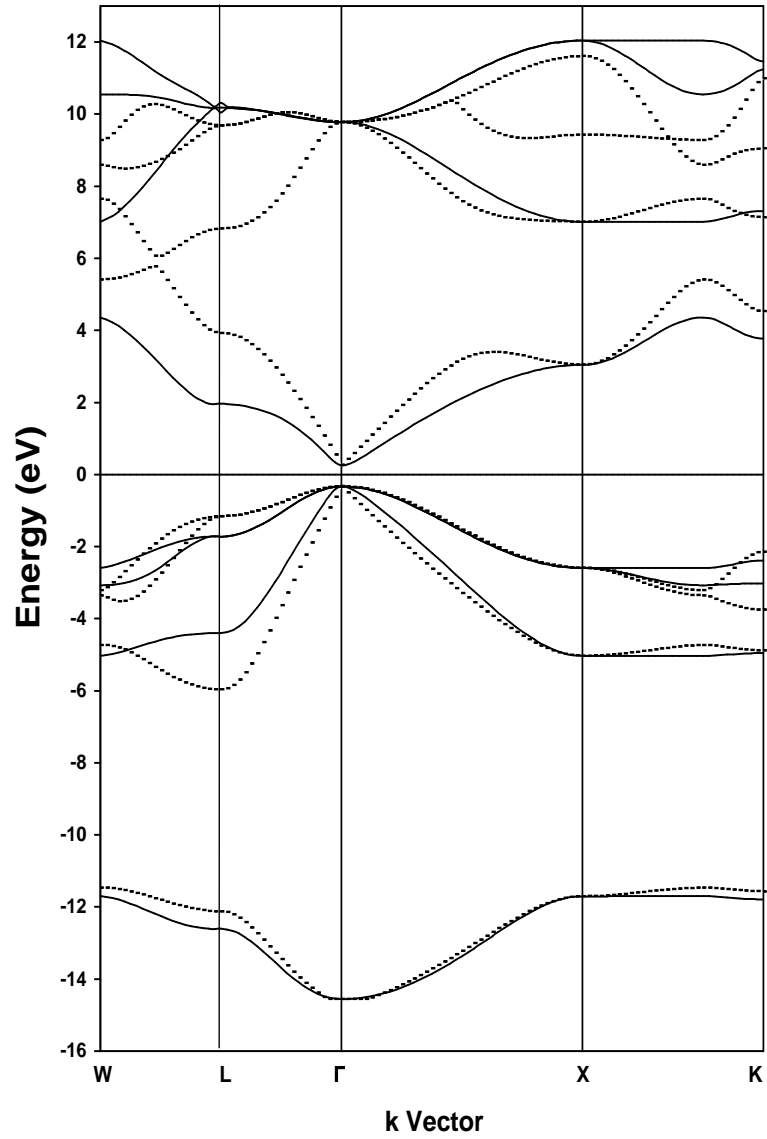


Figure 3.2: The energy band structure of *c-InN* by FP-LAPW(adjusted) (dotted line) and ETB (solid line).

at X and L (E_g^X , E_g^L) which are enlarged to the values of 3.375 and 4.249 eV are in good agreement with the results reported in Refs. [65, 66, 74] and [65, 66], respectively.

In the following step of the present work, the energy parameters of ETB have been derived for *c-InN* from the band structure of DFT (Fig. 3.2) by the fitting process explained in ch. 2. The band structure of *c-InN* recalculated by ETB is shown in Fig. 3.2. The imported features of the band structure at high symmetry points are listed in Table 3.3. In view of Fig. 3.2, we note that there is a close agreement between the band structure of *c-InN* by ETB and DFT at Γ and X points. Hence, the derived energy parameters of ETB can be used surely in the band structure calculations of *c-InN* and its alloys. The direct band gap of *c-InN* recalculated by ETB is exactly the same with the adjusted value of 0.59 eV in DFT calculations. The present direct gap of ETB is 20% smaller than the value of ab-initio self consistent calculations in which the experimental lattice constant value (4.98 Å) of *c-InN* was used within LDA and the Bagayoko, Zhao, Williams (BZW) implementation of the linear combination of atomic orbitals [66]. The present E_g^Γ is only 9.2% smaller than the value of 0.65 eV calculated by the theoretical lattice constant of *c-InN* in the same report [66]. The present direct band gap value of *c-InN* is exactly the same with its corrected value reported in Ref. [65]. The present E_g^Γ of *c-InN* is approximately 16% smaller than the value calculated by DFT-LDA [95] and LDA based semi-empirical methods [110]. On

Table 3.3: A summary of the important features, energy gaps and valance bandwidths of the present DFT (adjusted) and ETB band structure for *c-InN* compared to other experimental and theoretical calculational results. All energies are in eV.

	<i>DFT</i> ^a (<i>adjusted</i>)	<i>ETB</i> ^a	<i>theoretical</i>		
			<i>LDA – BZW</i> ^b	<i>EPP</i> ^c	<i>DFT – LDF</i> ^d
Γ_1^v	-14.557	-14.557	-14.179		
Γ_{15}^v	-0.332	-0.332	0.000	0.000	0.000
Γ_1^c	0.258	0.258	0.654	0.592	0.435
Γ_{15}^c	9.779	9.779	9.762	9.597	10.174
X_1^v	-11.704	-11.704	-11.309		
X_3^v	-5.031	-5.031	-4.750	-4.795	-4.687
X_5^v	-2.594	-2.594	-2.209	-1.481	-1.687
X_1^c	3.043	3.043	4.182	4.758	2.903
X_3^c	7.012	7.012	6.898	5.102	6.322
L_1^v	-12.127	-12.608	-11.762		
L_1^v	-5.969	-4.399	-5.571	-4.967	-5.229
L_3^v	-1.159	-1.718	-0.834	-0.460	-0.557
L_1^c	3.917	1.951	4.032	3.213	3.831
L_3^c	9.683	10.173	8.434	10.040	6.954
$\Gamma_{15}^v - \Gamma_1^c$	0.59	0.59	(0.738, 0.65) ^b 0.70 ^{e,f}	0.592 ^c	0.592 ^d
$\Gamma_{15}^v - X_1^c$	3.375	3.375	4.182 ^b 2.51 ^e	4.758 ^c	2.903 ^d
$\Gamma_{15}^v - L_1^c$	4.249	3.670	4.032 ^b 5.82 ^e	3.213 ^c	3.831 ^d
$\Gamma_1^v - \Gamma_{15}^v$	14.225	14.225	14.179 ^b	14.79 ^g	

^apresent work, ^bRef. [66], ^cRef. [107], ^dRef. [65], ^eRef. 20 in Ref. [95], ^fRef. [110], ^gRef. [103]

the other hand, exactly the same energy gap at X point is obtained for *c-InN* by both ETB and DFT calculations. The present band gap values at X and L points are closer to the corresponding values given in Refs. [65, 66, 74] and [65, 66, 107], respectively. It is found that the present band gap energies of *c-InN* by ETB at high symmetry points (Γ , X, L) are in more agreement with the results of the calculations based on DFT within LDA-quasi particle corrections [65]. In the present ETB calculations, the valence band width is calculated to be 14.225 eV which is very close to the value of 14.179 eV calculated by DFT within LDA-BZW implementation [66]. The present valence band width of *c-InN* is also close to the value of 14.79 eV, although, the direct band gap value was calculated to be -0.48 eV in the same work [103].

3.2.2 InAs

In the present work, the equilibrium value of the lattice constant for *InAs* is determined by the total energy calculations based on DFT /GGA-FPLAPW. The total energy calculations are carried on a set of volumes and fitted to Murnaghan equation [53]. We have adopted the value of 1.2 Å for *In* and 1.15 Å for *As* as the MT radii. The electronic configuration of *InAs* is *In*: Kr ($4d^{10}5s^25p^1$) and *As*: Ar ($3d^{10}4s^24p^3$). In the calculations, the electrons of *In* in ($1s^22s^22p^63s^23p^63d^{10}4s^24p^64d^{10}$) are defined as the core electrons and distinguished from the valence electrons of *In* in ($5s^25p^1$). Similarly, the inner shell

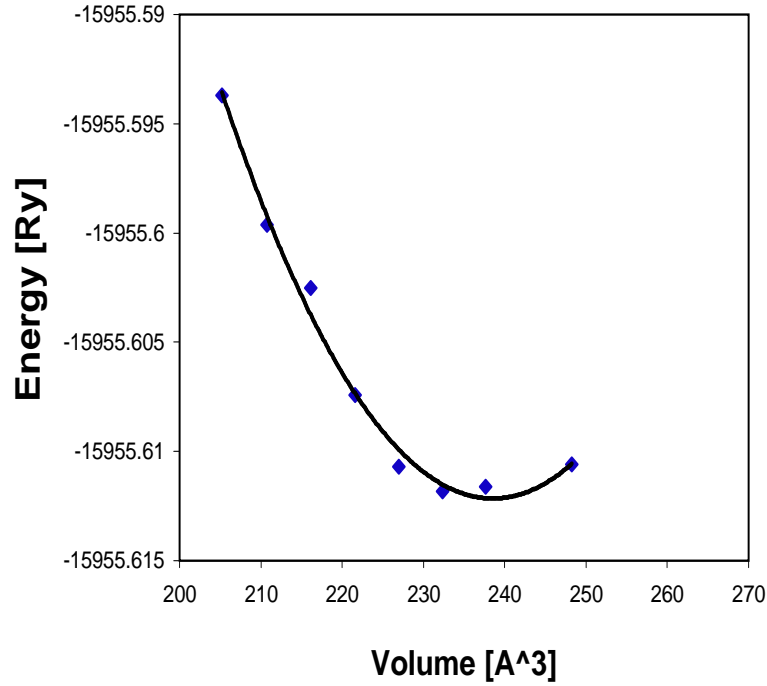


Figure 3.3: Total energy of *InAs* versus the lattice volume.

electrons of *As* in $(1s^2 2s^2 2p^6 3s^2 3p^6 3d^{10})$ are distinguished from the valence electrons of *As* in $(4s^2 4p^3)$. The curve of the total energy versus the unitcell volume is shown in Fig. 3.3. The equilibrium lattice constant of *InAs* is calculated to be 6.194 Å. The present lattice constant of *InAs* is given in Table. 3.2 together with the experimental and other calculated lattice constant values of *InAs* presented in the literature. In an early work [111], the lattice constant of *InAs* was measured to be 6.058 Å at room temperature. Another experimental lattice constant value of *InAs* was given as 6.036 Å in Ref. [112]. In a recent work [113], the value of 6.06 Å has been extracted from the reflectance difference spectra of the *InAs* grown on *InP*. The present lattice constant of *InAs* at 0 °K is about

2.2 - 2.6 % greater than these measured values at room temperature. The lattice constant values of both 5.906 and 5.94 Å have been calculated by ab-initio pseudo potentials [114, 115]. In another theoretical work, the lattice constant of *InAs* has been calculated as 5.85 Å by generalized density functional theory (GDFT) within LDA (GDFT/LDA) [116]. It is found that, the present equilibrium lattice constant value of 6.194 Å is in more agreement with the value of (6.063 Å) DFT/LDA-FPLAPW [115] than the values of ab-initio pseudopotential [114, 115] and GDFT/LDA calculations [116]. The difference is only 2.2%.

In the present work, the energy band structure of *InAs* has been calculated by DFT/FP-LAPW-GGA for the present equilibrium lattice constant value of *InAs*. We have concentrated mainly on the energy gaps at high symmetry points. It is found that, band gap of *InAs* is direct. The variation of energy bands is in agreement with the result of nonlocal PP calculations [78]. The present band structure of *InAs* is also very close to the band structure of ETB [55] except along $\Gamma - X$ direction. The band structure has a maximum point along $\Gamma - X$ direction in both present and nonlocal PP calculations [78], but in ETB calculational results [55] it approaches to X point constantly by passing through a point of inflection. In the present calculations, the energy values of the main features at high symmetry points ($\Gamma_1^V, X_1^V, X_3^V, X_5^V, L_3^V$) are in good agreement with the corresponding values measured by PL spectra [71]. But, the direct band gap of *InAs* (0.277 eV) is found to be smaller than its experimental values

reported in Refs. [68, 26, 72, 73, 74, 75, 76]. The present narrow direct band gap of *InAs* has been adjusted to the value of 417 meV which is recommended in Ref. [5], with respect to the available experimental values. The half of the energy difference between 417 meV and the present direct band gap is added to the first conduction and last valence band state energies equally in the same manner defined in Ref. [108]. The adjusted energy band structure of *InAs* by DFT/FP-LAPW-GGA is shown in Fig. 3.4. Table 3.4 gives the important features of the present and previously reported band structures for *InAs* at high symmetry points. The present energy gaps at X and L points are enlarged to 1.787 and 1.461 eV, respectively by adjustment.

In the following stage of the work, the energy parameters of ETB have been derived for *InAs* from the band structure of DFT (Fig. 3.4) by the fitting process explained in Ch. 2. The recalculated band structure of *InAs* by ETB is shown in Fig. 3.4. The important features of the band structure at high symmetry points are listed in Table 3.4. As it is observed in Fig. 3.4, the valence band structure of *InAs* by ETB follows that of DFT along both $\Gamma - X$ and $\Gamma - L$ directions closely. The variation of the first conduction band energy of *InAs* is similar in both ETB and DFT results along $\Gamma - L$ direction. The first state energies of the conduction band by ETB deviate from the present results of DFT along $\Gamma - X$ direction and approach to the X point constantly. The similar variation was plotted by ETB calculations for sp^3s^* interactions of *InAs* in Ref. [55]. The energy gaps

Table 3.4: A summary of the important features, energy gaps and valance bandwidths of the present DFT (adjusted) and ETB band structure for $InAs$ compared to other experimental and theoretical calculational results. All energies are in eV.

	DFT^a (adjusted)	ETB^a	<i>theoretical</i>			<i>experimental</i> PL^e
			DFT^b	TB^c	EPP^d	
Γ_1^v	-11.102	-11.102	-11.52	-12.69	-12.69	-12.3
Γ_{15}^v	-0.132	-0.132	0.00	0.00	0.0	
Γ_1^c	0.285	0.285	0.42	0.37	0.37	
Γ_{15}^c	3.898	3.898	3.68	4.39	4.39	
X_1^v	-9.419	-9.419	-9.39	-10.20	-10.20	-9.8
X_3^v	-5.230	-5.230	-6.16	-6.64	-6.64	-6.3
X_5^v	-2.205	-2.205	-2.41	-2.47	-2.47	-2.4
X_1^c	1.655	1.655	2.33	2.28	2.28	
X_3^c	2.331	2.331	2.77	2.66	2.26	
L_1^v	-9.875	-9.924	-10.03	-10.99	-10.92	
L_1^c	-5.237	-5.237	-6.03	-6.87	-6.23	
L_3^v	-1.003	-1.418	-1.01	-1.05	-1.26	-0.9
L_1^c	1.329	1.425	1.13	1.50	1.53	
L_3^c	4.601	3.614	5.20	5.84	5.42	
$\Gamma_{15}^v - \Gamma_1^c$	0.417	0.417	0.42 ^b 0.417 ^g	0.37 ^{c,d} 0.419 ^h	0.418 ^f	0.418 ^{i,j} , 0.416 ^{k,l} 0.420 ^m , 0.415 ⁿ
$\Gamma_{15}^v - X_1^c$	1.787	1.787	2.33 ^b 1.398 ^h	2.28 ^{c,d}	1.433 ^k	
$\Gamma_{15}^v - L_1^c$	1.461	1.587	1.13 ^{b,k} 1.110 ^h	1.50 ^c	1.53 ^d	
$\Gamma_1^v - \Gamma_{15}^v$	10.970	10.970	11.52 ^b	12.69 ^{c,d}		

^apresent work, ^bRef. [77], ^cRef. [79], ^dRef. [78], ^eRef. [71], ^fRef. [81], ^gRef. [5],
^hRef. [80], ⁱRef. [74], ^jRef. [71], ^kRef. [68], ^lRef. [72], ^mRef. [75], ⁿRef. [76]

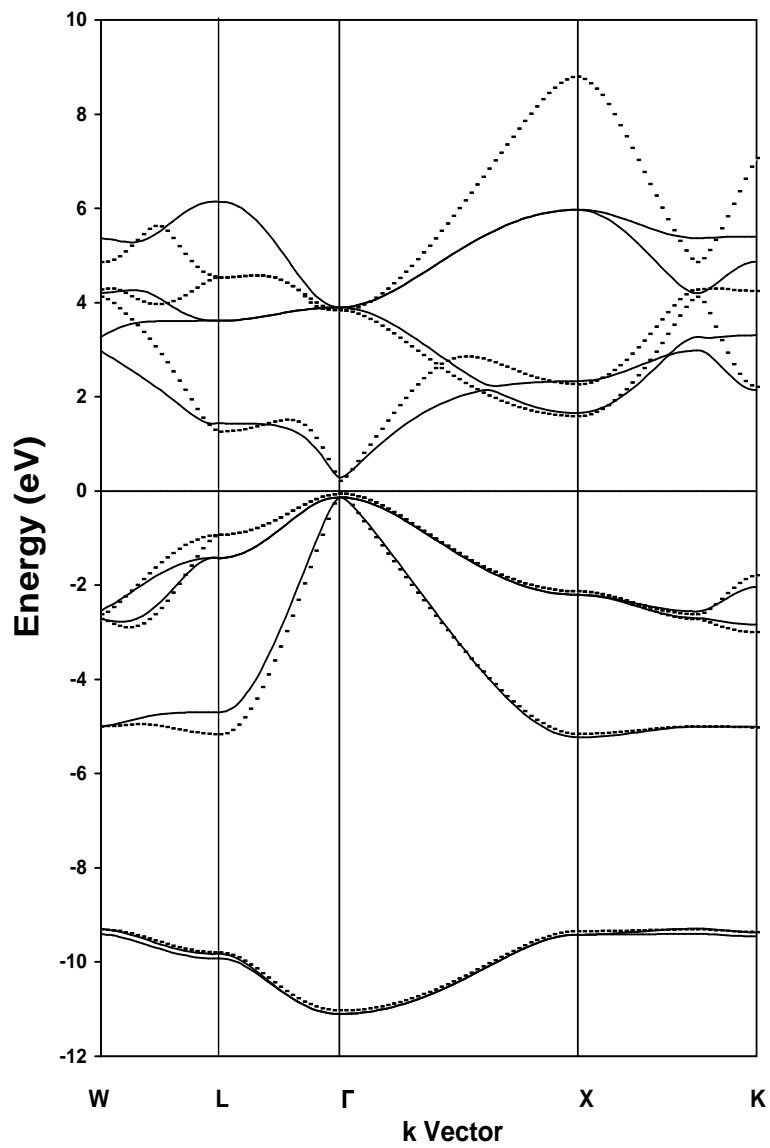


Figure 3.4: The energy band structure of *InAs* by FP-LAPW (adjusted) (dotted line) and ETB (solid line).

of *InAs* at Γ and X points are found to be exactly the same by both present ETB and DFT calculations. The present E_g^Γ value of 0.417eV is very close to the corresponding values of EPP [80] and ETB [81] calculations. The present E_g^Γ is only 0.71% smaller than the value of 0.42 eV calculated by DFT within LDA [77]. The present direct band gap of *InAs* is about 12.7% greater than the value reported by both tight binding calculations within Green's functional approach [79] and nonlocal EPP calculations [78]. The present E_g^X is in the range (1.394 - 2.33 eV) of the values calculated by different methods [68, 77–80]. The E_g^L of ETB is found to be closer to the corresponding values given by tight binding [79] and EPP [78] calculations than the values of DFT-LDA [77] and EPP [80] calculations. The width of the valence band is found to be the same by both present ETB and DFT/GG-FP-LAPW calculations; it is about (4.77- 13.55) % smaller than the values reported in Refs. [77–79].

3.2.3 InSb

The equilibrium lattice constant value of *InSb* is determined by total energy calculations based on DFT within GG approximation. The total energy for a set of volumes has been calculated by FP-LAPW method and fitted to the Murnaghan equation [53]. We have adopted the value of 1.058 Å for *In* and 1.058 Å for *Sb* as the MT radii. The electronic configuration of *InSb* is *In*: Kr ($4d^{10}5s^25p^1$) and *Sb*: Kr ($4d^{10}5s^25p^3$). In the calculations, the electrons of *In*

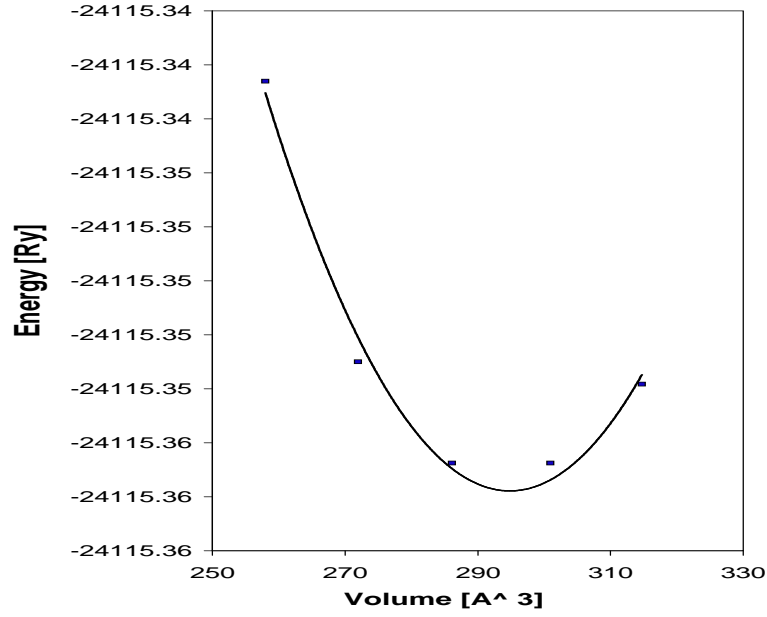


Figure 3.5: Total energy of *InSb* versus the lattice volume.

in $(1s^2 2s^2 2p^6 3s^2 3p^6 3d^{10} 4s^2 4p^6 4d^{10})$ are defined as the core electrons and distinguished from the valence electrons of *In* in $(5s^2 5p^1)$. Similarly, the inner shell electrons of *Sb* in $(1s^2 2s^2 2p^6 3s^2 3p^6 3d^{10} 4s^2 4p^6 4d^{10})$ are distinguished from the valence band electrons of *Sb* in $(5s^2 5p^3)$ shell. The total energy of *InSb* as a function of unit cell volume is shown in Fig. 3.5. The calculated total energy of *InSb* is found to be minimum with the lattice constant value of 6.643 \AA . The present lattice constant of *InSb* is given in Table. 3.2 together with the experimental and other calculated lattice values of *InSb* presented in the literature. In a very early work [117], the lattice constant of *InSb* was measured as 6.4782 \AA at room temperature by electron diffraction method. The similar experimental value (6.47937 \AA) was given in Ref. [118]. Besides, the temperature dependence of the lattice

constant of *InSb* was given also in Ref. [118] in the range of 10-60 °C. Another experimental lattice constant value of 6.49 Å was tabulated in Ref. [119] for *InSb*. The present lattice constant of *InSb* is about (2.3- 2.5)% greater than these measured values. In the literature, the first theoretical lattice constant values for *InSb* were given by ab-initio pseudopotential calculations [114, 115, 120]; they were 6.36 and 6.34 Å, respectively. The present lattice constant value of *InSb* is about (4.4 - 4.7)% greater than these pseudopotential calculational results. The first full potential calculations for *InSb* was also studied by Massidda *et al* [115]. They found that, the lattice constant of *InSb* by DFT/LDA-FP-LAPW calculations had better agreement with the experimental results than those of ab-initio pseudo potential calculations [114, 115, 120]. The following two lattice constant values (6.42 and 6.478 Å) in Table. 3.2 were again calculated by full potential calculations [121, 122]. The present equilibrium lattice constant value of 6.643 Å is found to be about (2.5 - 3.4)% greater then these first principles calculational results[121, 122].

In the present work, the energy band structure of *InSb* has been calculated by DFT/FP-LAPW-GGA for the present lattice constant of *InSb*. As it was aimed for the previous two compounds, *InN* and *InAs*, the band structure of *InSb* is evaluated mainly by the energy gaps at high symmetry points. In the present first principles calculations, the energy gap of *InSb* is found to be direct. The present order between the energy gaps, $E_g^\Gamma < E_g^L < E_g^X$, is the same as it

was reported in all previous theoretical works [77–80, 88–90, 121]. Besides, the variation of the bands is found to be similar with the results given in these works [77–80, 88–90, 121]. In both present and previously reported results [88–90, 121] the energy variation of the highest valance band and the lowest conduction band can be characterized by a very sharp slope at Γ point. The present energy of the first conduction band state has a maximum along Γ -X and Γ -L directions. This variation is exactly the same with the DFT/LDA-FP-LAPW results of Guo *et al* [121]. But in the other calculations [80, 88, 90], the energy of the first conduction band state approaches to L point with an approximately constant slope. In the present work, the E_g^Γ of *InSb* is found to be small (0.08 eV) as the uncorrected direct band gap values reported in the previous works [89, 90, 121]. The present semimetallic band structure of *InSb* at Γ point is corrected empirically. The E_g^Γ is shifted to its experimental value of 0.235 eV [26, 74, 85]. The half of the energy difference between the present direct band gap and 0.235 eV is added to the first conduction and last valence band state energies equally. The adjusted energy band structure of *InSb* by DFT/FP-LAPW-GGA is shown in Fig. 3.6. Table 3.5 gives the important features of the present and previously reported band structures for *InSb* at high symmetry points. The enlarged energy gaps at L and X points are very close to the values of 0.82 and 1.55 eV, respectively which were calculated by DFT/LDA-FP-LAPW [90].

In the present work, the energy parameters of ETB have been obtained for

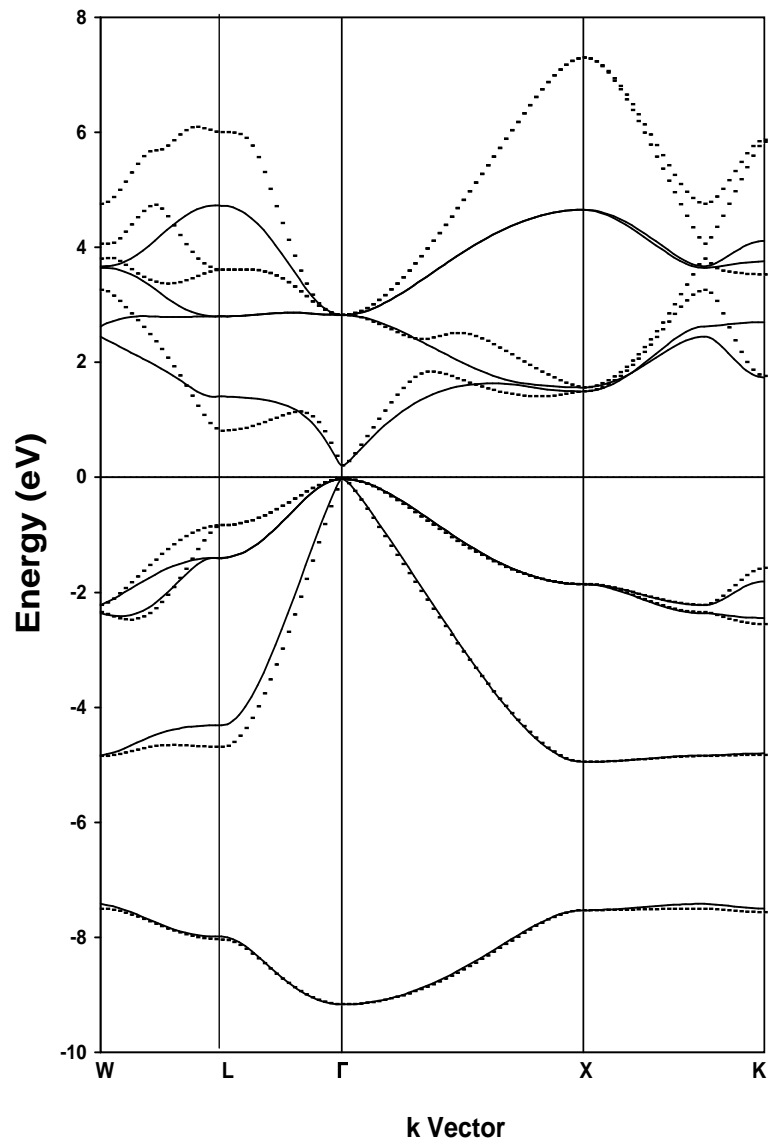


Figure 3.6: The energy band structure of *InSb* by FP-LAPW (adjusted) (dotted line) and ETB (solid line).

Table 3.5: A summary of the important features, energy gaps and valance bandwidths of the present DFT (adjusted) and ETB band structure for *InSb* compared to other experimental and theoretical calculational results. All energies are in eV.

	<i>DFT</i> ^a (adjusted)	<i>ETB</i> ^a	<i>theoretical</i>			<i>exp.</i> <i>PL</i> ^e
			<i>Non.PP</i> ^b	<i>DFT</i> ^c	<i>TB</i> ^d	
Γ_1^v	-9.167	-9.167	-11.71	-10.52	-11.71	-11.71
Γ_{15}^v	-0.029	-0.029	0.00	0.00	0.0	
Γ_1^c	0.206	0.206	0.25	0.24	0.25	
Γ_{15}^c	2.822	2.822	3.16	2.66	3.16	
X_1^v	-7.530	-7.530	-9.20	-8.54	-9.20	-9.0
X_3^v	-4.950	-4.950	-6.43	-5.84	-6.43	-6.4
X_5^v	-1.859	-1.859	-2.25	-2.52	-2.45	-2.4
X_1^c	1.493	1.493	1.71	1.71	1.71	
X_3^c	1.564	1.564	1.83	2.23	1.81	
L_1^v	-8.040	-7.986	-9.95	-9.13	-10.03	
L_1^v	-4.691	-4.315	-5.92	-5.79	-6.81	
L_3^v	-0.836	-1.398	-1.44	-1.08	-1.06	-1.05
L_1^c	0.810	1.401	1.03	0.70	0.99	
L_3^c	3.608	2.799	4.30	4.13	5.46	
$\Gamma_{15}^v - \Gamma_1^c$	0.235	0.235	0.25 ^{b,d} 0.18 ^h	0.24 ^{c,f} 0.21 ⁱ	0.235 ^g 0.26 ^j	0.235 ^{k,l,m} 0.235 ⁿ 0.24 ^o 0.18 ^p 0.23 ^r 1.79 ^o
$\Gamma_{15}^v - X_1^c$	1.522	1.522	1.71 ^{b,c,d} 1.82 ⁱ	0.6618 ^g	1.55 ^h	
$\Gamma_{15}^v - L_1^c$	0.839	1.430	1.03 ^b 0.9743 ^g	0.70 ^c 0.82 ^h	0.99 ^d 1.02 ⁱ	
$\Gamma_1^v - \Gamma_{15}^v$	9.138	9.138	11.71 ^{b,d} 10.9 ^s	10.52 ^c (10.83, 11.05) ^t	11.57 ^h	11.7 ^u 11.2 ^w

^apresent work, ^bRef. [78], ^cRef. [77], ^dRef. [79], ^eRef. [71], ^fRef. [89], ^gRef. [80], ^hRef. [90], ⁱRef. [91], ^jRef. [88], ^kRef. [26], ^lRef. [85], ^mRef. [74] ⁿRef. [86], ^oRef. [76], ^pRef. [87], ^rRef. [84], ^sRef. [121], ^tRef. [122], ^uRef. [123], ^wRef. [124]

InSb by the fitting process from the present band structure of DFT (Fig. 3.6). The recalculated band structure of *InSb* by ETB is shown in Fig. 3.6. The important features of the ETB band structure at high symmetry points are listed in Table 3.5. The valence band structure of *InSb* is found to be exactly the same by both present ETB and DFT calculations. The sharp and smooth variations of the band structure of *InSb* around Γ and X points, respectively have been produced successfully by the present ETB energy parameters. The energy gaps of *InSb* at Γ and X points are found to be exactly the same by both ETB and DFT calculations. The present E_g^Γ value of 0.235 eV is very close to the values calculated by EPP [80], DFT-LDA [77] and relativistic self consistent LMTO scheme [89]. The present E_g^Γ is about (6 - 9.6)% smaller than the corresponding value calculated by nonlocal PP [78], tight binding Green's functional approach [79] and self-consistent PP [88]. The corrected band gap energy values reported in Refs. [90, 91] are about (12-30)% smaller than the present E_g^Γ . The calculated band gap at X point is very close to the value of 1.55 eV which was obtained by the corrected results of DFT/LDA calculations [90]. The discrepancy between the present and the available experimental value [76] of E_g^X is about 15%. The ETB calculations of *InSb* give quietly high band gap energy at L point with respect to the values reported in literature [77–91]. On the other hand, the width of the valence band is the same for both present ETB and DFT calculations, but it is about (13-22)% smaller than the available experimental [123, 124] and theoretical

results [77–79, 90, 121, 122].

CHAPTER 4

THE ELECTRONIC BAND STRUCTURE OF InN_xAs_{1-x} ,

InN_xSb_{1-x} AND $InAs_xSb_{1-x}$ ALLOYS

4.1 Introduction

There is currently considerable interest in InN , $InAs$ and $InSb$ because of their optical and high temperature device applications. InN is a highly potential material for the fabrication of high speed heterojunction transistors [1] and low cost solar cells with high efficiency [2]. $InAs$ and $InSb$ are interesting narrow gap semiconductors from the point view of optical spectroscopy and optoelectronic applications [125]. Since $InAs$ has a high electron mobility, it may prove an important material for use in high speed electronics [11, 12]. $InSb$ calls the attention to have the smallest energy gap of any of the binary III-V materials. This property often allows the fabrication of infrared imaging systems, free space communications and gas phase detection systems [16, 17].

A new class of semiconductor alloys in which one of the constituent elements is replaced by an element with highly dissimilar properties has been discovered recently. These new ternary semiconductor alloys exhibit a range of unexpected

characteristics. Particularly, the addition of a small amount of nitrogen in $InAs$ and $InSb$ compounds leads to spectacular changes of the electronic properties [21, 22, 87, 126–132]. On the other hand, the substitution of a small amount of As in $InSb$ indicates the similar drastic changes on the electronic properties of $InSb$ compound [23–29, 133–136]. The most important effect of the substitutions in these InN_xAs_{1-x} , InN_xSb_{1-x} and $InAs_xSb_{1-x}$ alloys is large reduction of the fundamental band gap of $InAs$ and $InSb$. In the literature, the aim dependent reduction of fundamental energy band gap has been regulated by the substituent compositions in $InNAs$, $InNSb$ and $InAsSb$ [21–29, 87, 126, 129–133, 135] alloys grown by molecular beam epitaxy (MBE) [22, 24, 25, 27, 87, 130–132], metal organic chemical vapor deposition (MOCVD) [21, 26, 28, 126, 129], Bridgman [29] and hotwall epitaxy (HWE) [136] methods. Therefore these ternary alloys are potential materials for room temperature infrared detectors, gas sensors and lasers operating in near infrared (0.9-1.3 μm), mid - infrared (2-5 μm) and far infrared (8-12 μm) regions [21, 22, 24–29]. In the literature, the most of the work on InN_xAs_{1-x} , InN_xSb_{1-x} and $InAs_xSb_{1-x}$ alloys are experimental. To the best of author knowledge, there are a limited number of works [22, 87, 127, 128, 131, 132, 134, 135] in which the electronic structure of these ternary alloys has been studied theoretically. In most of these theoretical works, the ternary alloys were defined by only specific concentrations of N and As [22, 87, 127, 131, 132, 135].

In the present work, the electronic structure of InN_xAs_{1-x} , InN_xSb_{1-x} and

$InAs_xSb_{1-x}$ have been calculated by employing the empirical tight binding (ETB) method. The calculations have been performed on alloys to introduce the band gap bowing corresponding to the whole range of nitrogen and arsenic concentrations. The results of the alloys considered in this work are separately discussed in the following sections and concluded in Chapter 7.

4.2 Electronic structure of alloys

4.2.1 InN_xAs_{1-x}

In III-V semiconductors, the replacement of a few percent of the group V element by small, highly electronegative and isoelectronic nitrogen atoms results in a drastic reduction of the fundamental band gap of approximately 100 meV per atomic percent of nitrogen [137, 138]. This effect of N has been confirmed for InN_xAs_{1-x} alloys experimentally [21, 126, 130] with the concentration $x < 18\%$. The InN_xAs_{1-x} alloys with the N concentration range of $0 < x < 0.061$ have been grown by MOCVD for the first time by Naoi *et al* [126]. They indicated that, all their samples had direct transition band structures and the increase in nitrogen content made the band energy smaller, with a minimum band gap energy of 0.12 eV for $InAs_{0.939}N_{0.061}$ [126]. Therefore the band gap of $InAs$ was able to be decreased by approximately 260 meV with the inclusion of only 6.1% of nitrogen at room temperature. In another work [130], the photoluminescence (PL) peak energy was observed to be decreased with N composition in the $InAsN$ layer of

the *InAsN/InGaAsP* multiple quantum well; A 1% nitrogen increase in alloy composition caused a shrinkage of 31 meV on the transition energy at 10 K. The smallest transition energy was reported as 0.190 eV when the nitrogen content in *InAsN* wells was determined to be 18% for the *InNAs/GaAs* multiple quantum wells [21].

In theoretical side, the bowing parameter of the band gap as a function of x has been studied using tight-binding method by Yang *et al.* [127] for $x=0.25, 0.5$ and 0.75 ordered InN_xAs_{1-x} alloys defined within a unit cell. The band gap of *InAs* calculated in this work [127] was decreased by ~ 0.48 eV by the inclusion of 50% of nitrogen. In a recent work [128], the tight-binding calculations have been carried out both maximally *N*-rich and *As*-rich cluster configurations for InN_xAs_{1-x} alloys defined in a supercell. This study [128] has indicated that the band gap of InN_xAs_{1-x} decreased to zero when $x=0.17$ and $x=0.50$ for maximally *N*-rich and *As*-rich cluster configurations, respectively. In the same work [128], the variation of the band gap of these configurations in InN_xAs_{1-x} alloys was also studied for $x > 0.75$ but not for the metallic region.

In the present ETB work, the electronic band structure of InN_xAs_{1-x} has been calculated for the full range of nitrogen concentration ($0 < x < 1$). The lattice constant of the cubic unit cell (working cell) is defined for each gradually increased nitrogen concentration (x) by use of the equilibrium lattice constant values of *InAs* and *InN* in Vegard's law equation (Eq. 2.52). The present ETB

energy parameters for InN_xAs_{1-x} based on sp^3d^2 orbital set and nearest neighbor interactions are defined by r^{-2} law (Eq. 2.4). The ETB energy parameters of $InAs$ and InN used in this calculation are given in Table 3.1. The present ETB band structure results of InN_xAs_{1-x} alloys have been analyzed by the variation of both energy band gap and conduction band edge around Γ due to the increase of nitrogen concentration. Fig. 4.1 displays the present fundamental band gap (E_g^Γ) variation of $InNSb$ as a function of nitrogen concentration. The E_g^Γ starts to decrease from the bulk value of $InAs$ (0.417 eV at 0 K) and reaches to its minimum value at $x=0.46$. In Fig. 4.1, the E_g^Γ passes to negative values at $x=0.12$ (cross point). The overall bowing parameter has been calculated to be 4.06 eV.

Since the room temperature experimental results belong to the epitaxially grown $InNAs$ instead of bulk samples, we couldn't compare the present E_g^Γ values of 0 K with the PL peak energies directly for $x < 0.061$. In Ref. [126], the PL peak energies corresponding to the fundamental gap energies of InN_xAs_{1-x} were measured to be 0.34, 0.28 and 0.21 eV for $x= 0.014$, 0.019 and 0.034, respectively. Therefore the band gap of InN_xAs_{1-x} is decreased by 0.04, 0.1 and 0.17 eV, respectively with respect to the room temperature band gap value of $InAs$ (0.38 eV). In the present work, approximately the same amount of decreased band gap energies have been calculated for the same values of x except at $x=0.014$; they are 0.013, 0.08 and 0.15 eV with respect to the band gap energy of $InAs$ (0.417

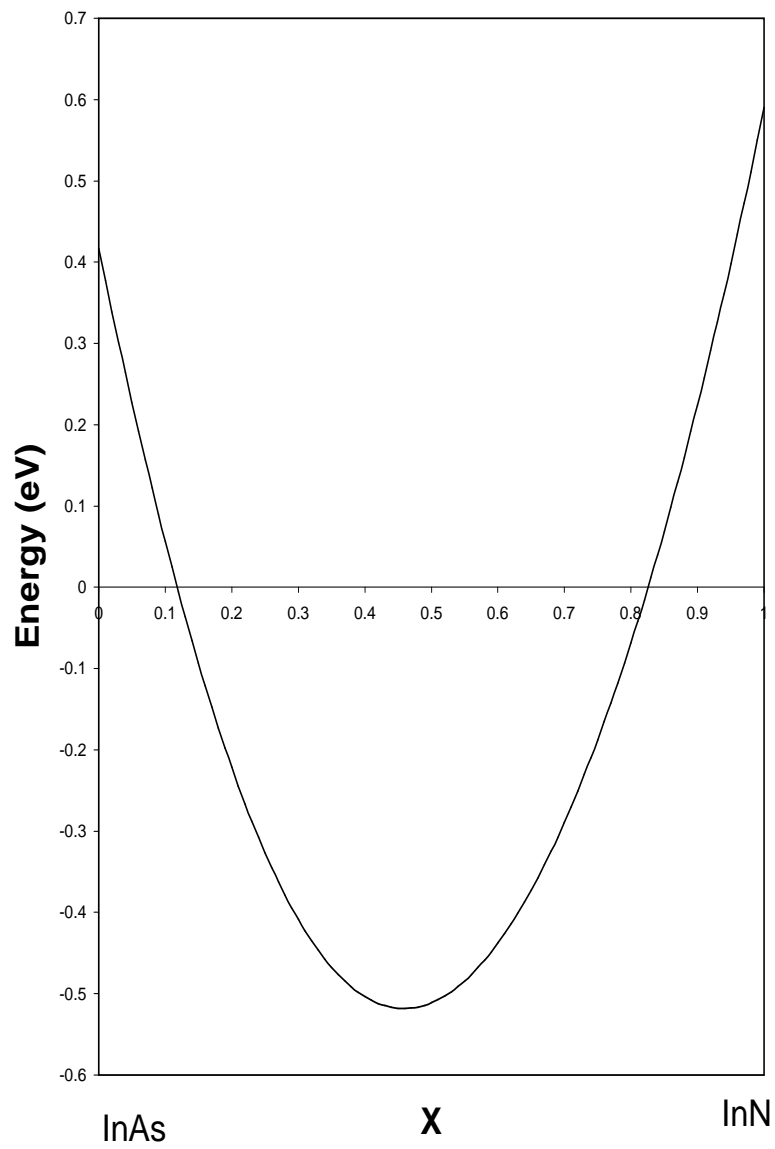


Figure 4.1: Band-gap energy vs composition (x) for InN_xAs_{1-x} alloys.

eV at 0 K) considered in this work. On the other hand, the present cross point of the bowing is more agreement with that (0.15) of the tight-binding calculations for maximally N -rich clusters in InN_xAs_{1-x} alloys [128] than that (0.5) of the ETB calculations for ordered $InNAs$ alloys [127]. The negative energy gaps of InN_xAs_{1-x} alloys obtained in the present work were not calculated in these works [127, 128], but they are predicted. The value of the overall bowing parameter calculated in this work is comparable with the value of 4.22 eV which was recommended in Ref. [139].

The calculated conduction band profiles of InN_xAs_{1-x} alloys for $x= 0.0, 0.02, 0.06$ and 0.12 are shown in Fig. 4.2. It is observed that the conduction band edge is nonparabolic for intrinsic $InAs$ as it was reported in the literature (sec. 3.2.2). In the view of Fig. 4.2, we note that the increase of N concentration decreases the values of conduction band edge and causes the interaction between the nitrogen level and the conduction band edge in InN_xAs_{1-x} alloys. Furthermore, the increase of N concentration ($x=0.02, 0.06$) in InN_xAs_{1-x} alloys increases the curvature of the conduction band edge around Γ point. Therefore a small amount of N concentration decreases the electron effective mass in InN_xAs_{1-x} alloys around Γ point.

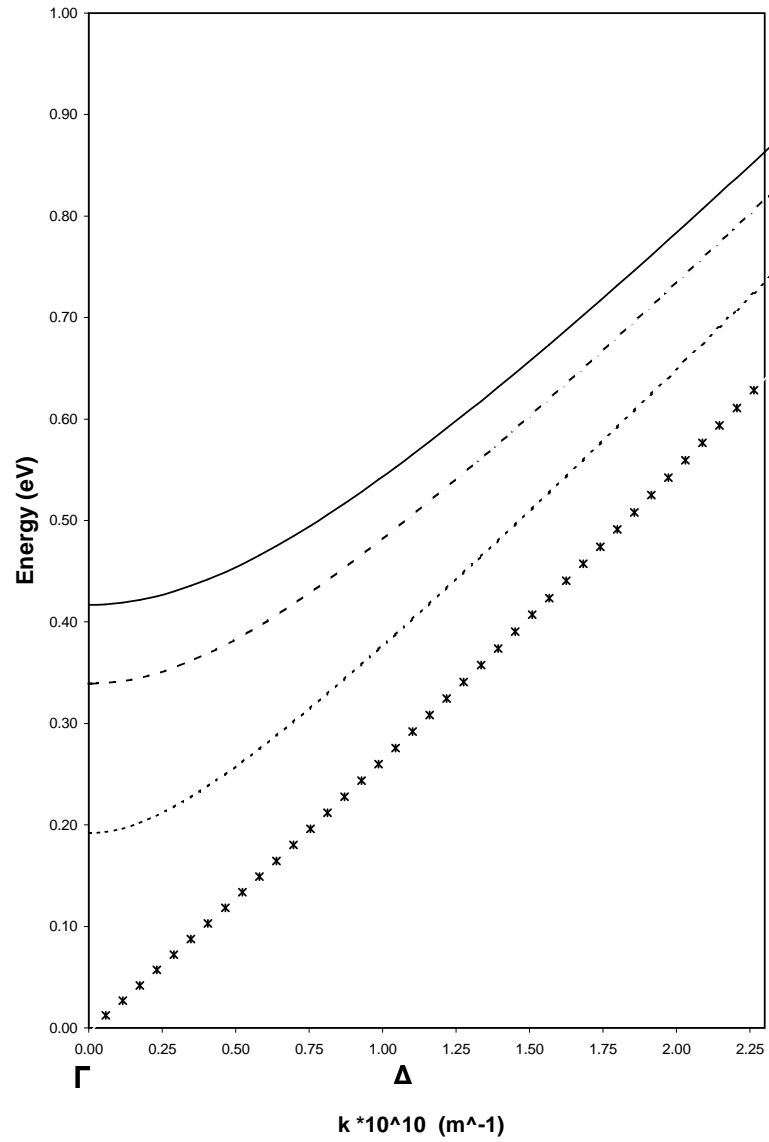


Figure 4.2: The conduction band dispersion calculated for InN_xAs_{1-x} alloys with $x = 0\%$ (solid line), 2% (dashed line), 6% (dotted line) and 12% (star line) around Γ point at 0 K.

4.2.2 InN_xSb_{1-x}

$InSb$ has the smallest band gap of any of the binary III-V semiconductors with an atmospheric transition window in the range of mid-infrared (3-5 μm). It was experimentally indicated that [22, 87, 131, 132], this atmospheric transition can access the range of (8-15 μm) when a small fraction of antimony is replaced by nitrogen in $InSb$. Time resolve optical measurement [131] have been used to observe an absorption edge of 15 μm at 290 K in an alloy with a nominal composition of $InN_{0.006}As_{0.994}$. In a recent work [22], the variation of the band gap of $InSb$ through incorporation of nitrogen was assessed optically by observation of the emission spectra from $InNSb$ LEDs and the transmission of light through the material. In the same work [22], the room temperature experimental results are modelled by $\vec{k} \cdot \vec{p}$ method and the sharp band gap decreasing of InN_xSb_{1-x} has been reported for nitrogen concentration in the range of $0 < x < 0.01$. The smallest band gap has been calculated to be 0.065 eV with respect to the nitrogen concentration of 0.01 [22]. On the other hand, the high-resolution electron energy loss spectroscopy (HREELS) of the nitrated layer in InN_xSb_{1-x} alloys indicated that a negative band gap alloy has been formed by the nitrogen-induced shift of the conduction band [87]. In the same work, the room temperature HREELS results of $InNSb$ alloy has been modelled by $\vec{k} \cdot \vec{p}$ model and the negative bowing of the band gap was obtained for a wider range of $0 < x < 0.1$ [87]. Besides, the $\vec{k} \cdot \vec{p}$ calculational results [87] have given negative band gap in the nitrogen

range of $0.02 < x < 0.1$; the conduction band minimum is below the valence band maximum indicating that the alloy is semimetallic.

In the present ETB work, the electronic band structure of InN_xSb_{1-x} alloys has been calculated for the full range of nitrogen concentration. The dimension of the unit cell (working cell) is calculated using the equilibrium lattice constant values of InN (4.967\AA) and $InSb$ (6.643\AA) (Table 3.2) in Eq. 2.52. The self interaction ETB energy parameters of compounds used in this work are taken from Table 3.1. The other ETB energy parameters are scaled for $InNSb$ alloys by r^{-2} law [48] as it is explained in sec. 2.4. In the present band structure study, we have concentrated on the variation of the fundamental gap energy and conduction band edge around the Γ point with respect to the increasing of the nitrogen concentration in $InNSb$ alloy. Fig. 4.3. displays the variation of the E_g^Γ due to the concentration of nitrogen for InN_xSb_{1-x} alloys. The variation gives a large bowing with the smallest energy gap value at $x=0.46$. The InN_xSb_{1-x} alloys are found to be metallic in the range of $0.14 < x < 0.76$. The calculated overall bowing parameter is 2.57 eV.

According to the recent resolved optical measurements [131], HREELS [87] and response wavelength measurements of LEDs [22], the band gap of the epitaxially grown InN_xSb_{1-x} alloys had a very sharp variation for small concentrations of nitrogen; the E_g^Γ decreased by ~ 100 meV with respect to the room temperature band gap value of $InSb$ (0.18 eV) in the nitrogen concentration range of

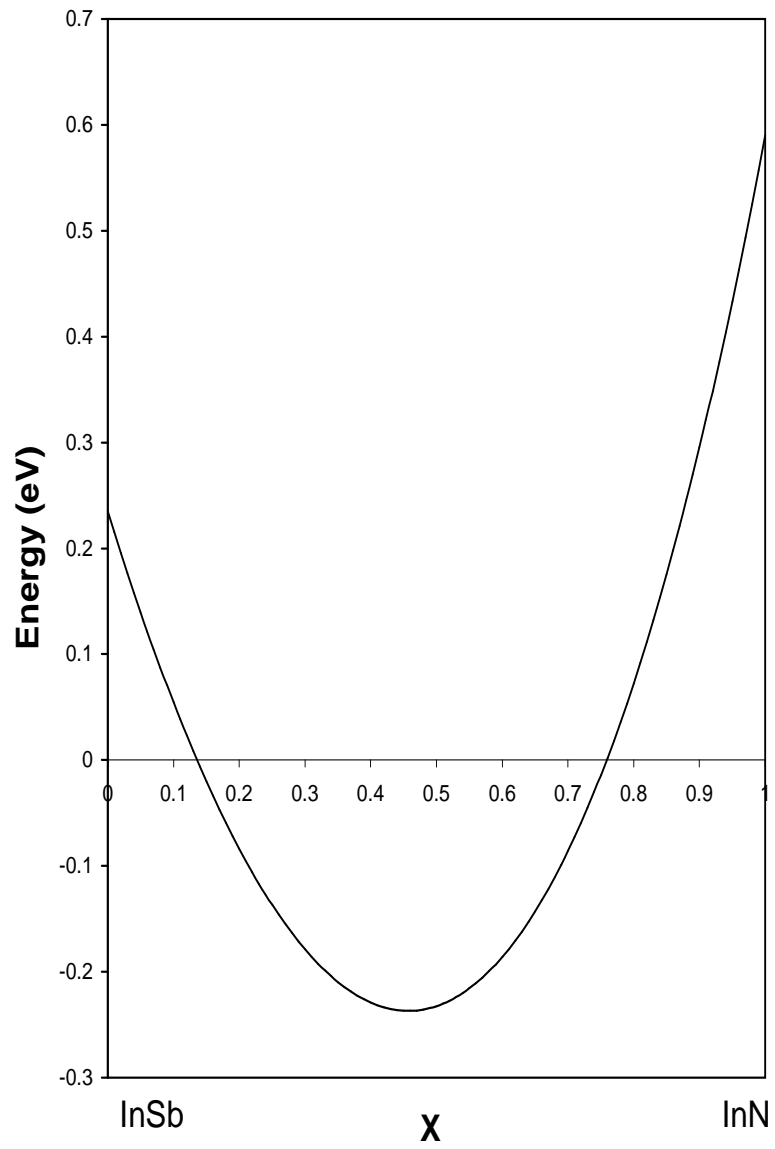


Figure 4.3: Band-gap energy vs composition (x) for InN_xSb_{1-x} alloys.

$0 < x < 0.006$. In the same range, the present reduction in the band gap is calculated to be only 15 meV with respect to the band gap value of *InSb* (0.235 eV) at 0 K. Therefore the $\vec{k} \cdot \vec{p}$ model calculations [22, 87] of the experimental band gap values give a cross point ($x=0.022, 0.011$) much smaller than ours ($x=0.14$) normally. On the other hand, the present ETB calculations give the smallest band gap value of -0.24 eV at $x=0.46$, but approximately twice of this band gap value was obtained in $\vec{k} \cdot \vec{p}$ model calculations [87] by the nitrogen concentration of 0.1. Fig. 4.4 displays the variation of the conduction band edge of *InN_xSb_{1-x}* alloys around Γ point for $x= 0.0, 0.02, 0.06$ and 0.14 . As it is reported above, Fig. 4.4 shows that the values of the conduction band edge are decreased in *InN_xSb_{1-x}* alloys with increase of nitrogen concentration. Furthermore the curvature of the conduction band edge is increased by increasing of nitrogen concentration ($x= 0.02, 0.06, 0.14$). Therefore a small amount of nitrogen concentration in *InN_xSb_{1-x}* alloys is sufficient to increase the speed of the conduction electrons. This result was also reported by $\vec{k} \cdot \vec{p}$ model calculations of *InN_xSb_{1-x}* alloys [131, 132].

4.2.3 *InAs_xSb_{1-x}*

InAs_xSb_{1-x} alloys with a small amount of *As* content have attracted considerable interest because of their potential for the fabrication of infrared sources and detectors. Although the energy gap of *InAs* (0.417 eV at 0 K) is larger than

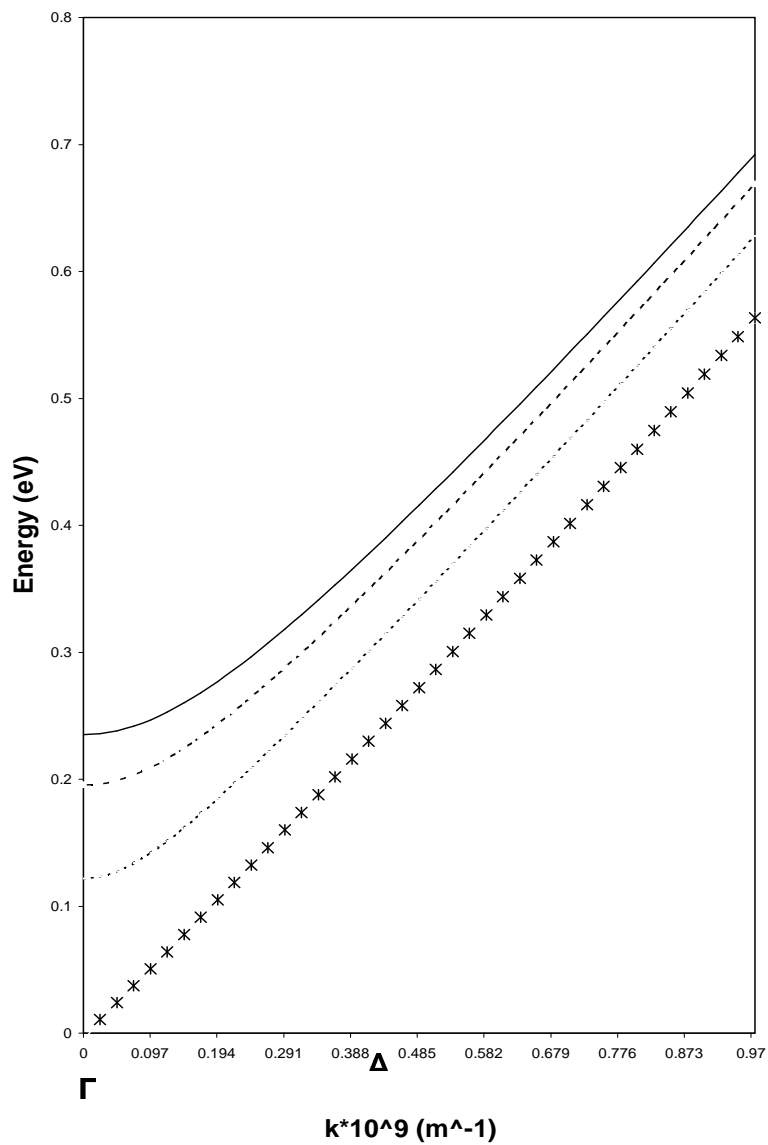


Figure 4.4: The conduction band dispersion calculated for InN_xSb_{1-x} alloys with $x = 0\%$ (solid line), 2% (dashed line), 6% (dotted line) and 14% (star line) around Γ point at 0 K.

that of *InSb* (0.235 eV at 0 K) by 0.18 eV, a small amount of *As* in *InSb* is sufficient to decrease the band gap of *InSb* to the values correspond to the long wavelengths in 8-12.5 μm spectral range. The variation of the optical properties of *InAs_xSb_{1-x}* was first investigated on bulk-grown polycrystalline samples by Woolley and Warner [133]. The lowest energy gap was measured to be 0.1 eV in this work [133], for $x = 0.35$. *InAs_xSb_{1-x}* materials over the complete composition range $0 < x < 1$ have been grown on *InAs* and characterized by X-ray diffraction and optical absorption measurements at room temperature and 10 K [24, 25]. The band gap energies of these materials correspond to the cutoff wavelengths of 12.5 and 8.7 μm were measured to be 0.099 and 0.14 eV for $x = 0.32$ at room temperature and 10 K, respectively [24, 25]. In Ref. [140], the lowest band gap of *InAs_xSb_{1-x}* has been reported to be 0.1 for $x = 0.4$. Huang *et al* [28] investigated the band gap variation of *InAs_xSb_{1-x}* alloys as a function of complete composition range by PL spectra and measured the lowest band gap of 0.14 eV for $x = 0.4$ at 10 K. In a recent work [29], the infrared transmission spectra of *InAs_xSb_{1-x}* alloys in single bulk crystal structure show a continuous decrease in optical energy gap with the increase of *As* content in *InSb*. In this work [29], the room temperature absorption edges correspond to the fundamental energy gaps were measured to be 0.16 and 0.15 eV for $x = 0.02$ and 0.05 , respectively. To the knowledge of authors, there are only two theoretical works [134, 135], in which the band gap bowing of the of *InAs_xSb_{1-x}* alloys has been predicted by empirical

pseudopotential calculations.

In the present ETB work, the electronic band structure of $InAs_xSb_{1-x}$ has been calculated for full composition range of As . The equilibrium lattice constant values of $InAs$ (6.194 Å) and $InSb$ (6.643 Å) (Table 3.2) have been used to calculate the dimension of the unit cell by Vegard's law equation (Eq. 2.52). The present lattice constant values have been compared by only the available room temperature lattice constant values of two alloys; [24, 29] the present lattice constant value of 6.62 and 6.48 Å for $x= 0.05$ and 0.35 are close to the measured lattice constant values of 6.4606 [29] and 6.3 Å [24] corresponding to the same As compositions, respectively. This similarity confirms the validity of Vegard's law in the lattice constant calculations of $InAs_xSb_{1-x}$ alloys.

In ETB band structure calculation of $InAs_xSb_{1-x}$ alloys, the nearest neighbor and sp^3d^2 orbital interactions are taken into account. The ETB energy parameters of $InAs$ and $InSb$ are given in Table 3.1. The self interaction ETB energies have been used in the calculations directly, but V_{ss} , V_{xx} , V_{xy} , V_{scpa} , V_{sapc} , V_{dapc} and V_{dcpa} have been scaled according to r^{-2} law [48] for $InAs_xSb_{1-x}$ alloys, as it is explained in sec. 2.4. In the present band structure study, we have investigated the variation of the fundamental band gap and conduction band edge with respect to the complete concentration range of As . Fig. 4.5 displays a variation of E_g^Γ as a function of x . In view of Fig. 4.5, we note that the overall bowing for Γ point transition is large and downward. The energy gap starts to decrease

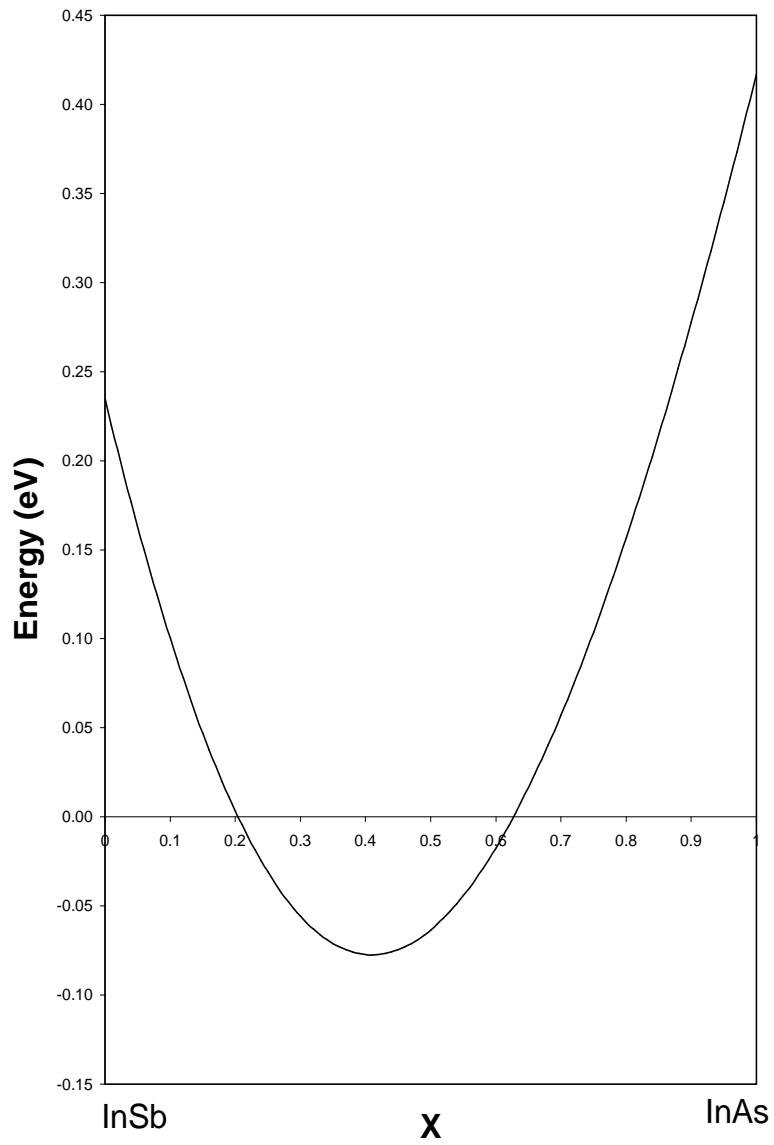


Figure 4.5: Band-gap energy vs composition (x) for $InAs_xSb_{1-x}$ alloys.

from the band gap value of *InSb* (0.235 eV at 0 K) and reaches to the lowest value at $x = 0.41$. Furthermore, *InAs_xSb_{1-x}* alloys are metallic in the range of $0.21 < x < 0.63$. The predicted bowing parameter by the best fit of our results to the expression given in Eq. 2.56 is 1.5649 eV.

In the literature, the bowing parameter was predicted to be 0.596 eV at room temperature by optical absorption [23]. The bowing parameter of *InAsSb* alloys estimated from low temperature PL measurements was reported to be higher than its value at room temperature; it was 0.6853 [25] and 0.672 eV [26] at 0 K. The bowing parameter predicted by EPP calculations for *InAs_{0.5}Sb_{0.5}* alloy were 0.7 [134] and 0.72 eV [135]. Since the present ETB energy parameters are adjusted to have the band gap values of bulk *InSb* and *InAs* at 0 K only, the present overall bowing parameter is found to be quiet high with respect to the reported values in the literature [25, 26, 135, 134, 23].

The present band gap values of *InAs_xSb_{1-x}* alloy have been compared with the PL spectra energies measured at $T = 10$ and 79 K for certain concentrations of *As*. the present band gap value of 0.163 eV is 19 % smaller than the PL value [25] of 0.20 eV for $x = 0.05$. The discrepancy increases to 39% when the concentration of *As* is 0.08 [25]. On the other hand, the present band gap value of 0.239 eV is 23 % smaller than the PL value of 0.31 eV for $x = 0.87$ (*As* rich *InAsSb* alloy) [25]. In this experimental study [25] the end point energy (at $x = 1$) corresponds to the band gap value of *InAs* was measured to be ~ 0.5 eV instead of ~ 0.4

eV. However, the present end point energy at $x = 1$ is in close agreement with the value of literature. The present band gap value of 0.04 for $x = 0.15$ is much smaller than the corresponding PL value [28] of 0.135 eV measured at 10 K. On the other hand, the calculated band gap value of 0.19 eV at $x = 0.83$ (*As* rich *InAsSb* alloy) is greater than the corresponding low temperature PL value of 0.13 eV [28]. The present band gap value of 0.303 eV for $x = 0.917$ is found to be 11% smaller than the measured value of 0.34 eV for the *InAs*_{0.917}*Sb*_{0.083} alloy grown on a lattice matched substrate (GaSb) at 79 K [27]. The PL peak energies of the *InAs*_{0.71}*Sb*_{0.29} and *InAs*_{0.85}*Sb*_{0.15} alloys at 10 K were reported to be 0.2 and 0.28 eV, respectively [26]. The corresponding values are found to be 0.066 and 0.22 eV by present ETB calculations.

In the present ETB calculations, the concentration of *As* ($x = 0.41$) corresponds to the lowest band gap of *InAs* _{x} *Sb*_{1- x} is very close to the value of 0.38 given by PL measurements [25].

Fig. 4.6 displays the variation of the conduction band edge of *InAs* _{x} *Sb*_{1- x} alloys around Γ point for $x = 0, 0.02, 0.06$ and 0.15 . It is found that the increase of the concentration of *As* in *InAs* _{x} *Sb*_{1- x} increases the curvature of the conduction band edge around Γ point relatively. Therefore a small amount of *As* concentration in *InAs* _{x} *Sb*_{1- x} alloys decreases the effective mass of the conduction electrons around Γ point.

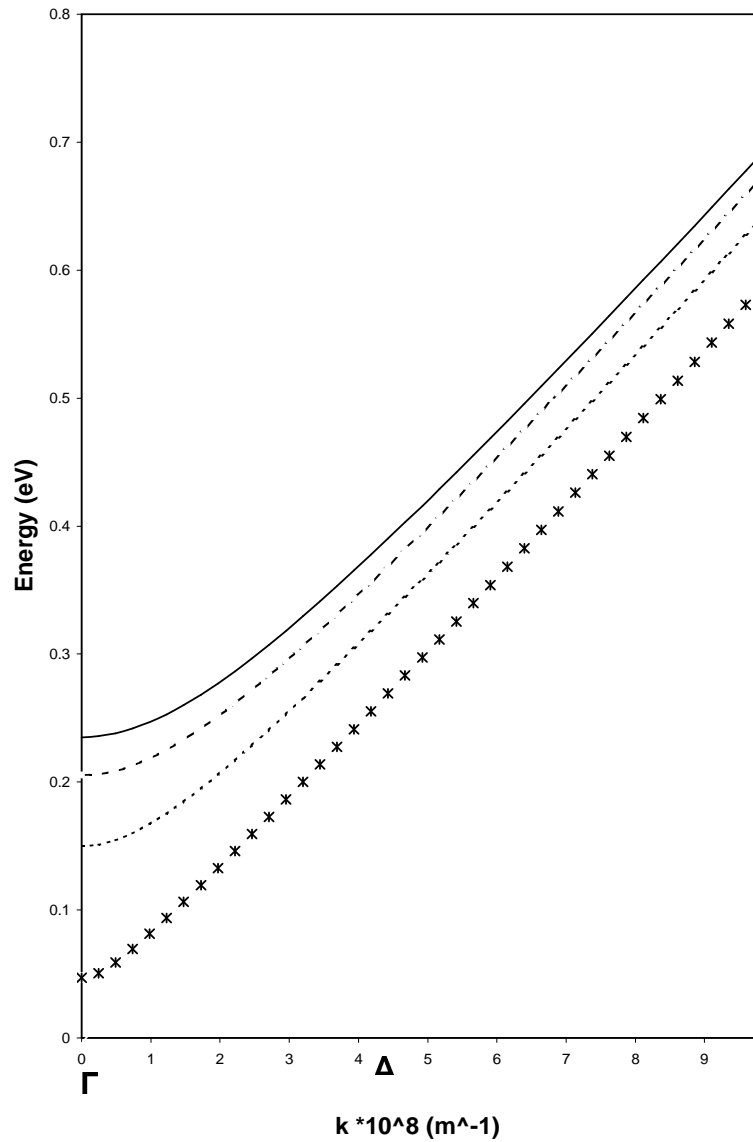


Figure 4.6: The conduction band dispersion calculated for $InAs_xSb_{1-x}$ alloys with $x = 0\%$ (solid line), 2% (dashed line), 6% (dotted line) and 15% (star line) around Γ point at 0 K.

CHAPTER 5

THE ELECTRONIC BAND STRUCTURE OF AlN , $AlSb$, $AlAs$ AND THEIR TERNARY ALLOYS WITH In .

5.1 Introduction

The III-V compounds, AlN , $AlSb$ and $AlAs$, are important for their several electronic and optoelectronic applications. For example, AlN is a candidate material for short wavelength light emitting diodes (LEDs), laser diodes (LDs) and optical detectors as well as for high temperature, high power and high frequency devices [6, 7, 8]. Because AlN has a wide band gap, a high melting point and a high thermal conductivity. The bulk $AlSb$ with its reported band gap of 1.7eV [141] has been considered as a potential material for infrared detectors and optical holographic memories [18, 19]. Epitaxial $AlSb$ has been used as a component of resonant tunneling diodes [20]. The third compound considered in this work, $AlAs$, has been widely used as a barrier material in modulation-doped heterostructures and quantum well of a lattice matched heterojunctions [13, 14].

In recent years, some of the ternary alloys of AlN , $AlSb$ and $AlAs$ with In have been investigated to find out the new potential materials for electronic and

optoelectronic devices. It has been reported [32] that the $Al_{1-x}In_xN$ alloys can have applications as a cladding layer or an active layer for LEDs and LDs emitting an extremely wide spectral region covering from deep ultraviolet (UV) to infrared. In another recent work [33], the $Al_{1-x}In_xN$ alloys have been considered as a potential material for thermoelectric power devices. The $AlAs$ based ternary $Al_{1-x}In_xAs$ alloys have been reported as an important buffer layer materials between $InAs$ and substrate in the technology of optoelectronic devices such as lasers and single electron transistors [34, 35]. Recently, $Al_{1-x}In_xAs$ alloys have been grown also for ultrafast switching device applications [36]. On the other hand the epitaxial growth of $AlInAs$ on $GaAs$ has been reported as a candidate material for triple function solar cells in a very efficiency [37]. The ternary $AlInSb$ alloys have been used as a buffer layer for multiple quantum lasers [38]. Recently, it has been reported that, $AlInSb$ alloys can be also a potential material to fabricate high efficiency low cost photovoltaic cells and photodetectors [39]. Because of the electronic and optoelectronic applications of AlN , $AlSb$ and $AlAs$ mentioned above, the electronic band structure of these binary semiconductors has been extremely studied in the literature theoretically by either first principles and empirical calculational methods [5, 55, 82, 92, 95, 82, 103, 116, 142–154]. In first principles calculations based on DFT [5, 92, 95, 97, 116, 143–146, 149, 152–154], the electronic band structure of binary compounds has been calculated to be very close to the experimental results by including certain approximations

such as local density (LD), generalized gradient (GG) and (GW) (dressed Green's function, G, and dynamical screened interaction, W). But the computational effort of these methods are still prohibitive for applications to systems containing a large number of atoms like alloys [152]. Actually, the first principles calculations have been limited by certain concentrations of constituents of alloys [152]. On the other hand, the empirical approaches such as empirical pseudopotential (EPP) and empirical tight binding (ETB) methods provide an attractive possibility for the electronic structure calculations of large sized systems with small sets of basic functions [142, 55, 82, 147, 150, 153]. By considering this fact, in the present calculations which extend to the electronic band structure of ternary alloys, we have used ETB method. The emphasis in those calculations was on describing well the valence bands and energy gaps. To establish the accuracy of the method and to obtain the necessary tight binding parameters, the electronic properties of the bulk AlN , $AlSb$ and $AlAs$ were studied first. The ETB energy parameters of the compounds based on the present first principles calculations are listed in Table 5.1. In the present chapter, the electronic band structure of compounds and the band gap bowing of $Al_{1-x}In_xN$, $Al_{1-x}In_xAs$ and $Al_{1-x}In_xSb$ alloys are separately discussed in the following sections and the results are evaluated in the last chapter.

Table 5.1: Empirical matrix elements of the sp^3d^2 Hamiltonian in eV.

	AlN	$AlAs$	$AlSb$
E_{sa}	-10.6965	-6.5244	-6.0802
E_{sc}	-0.1173	-2.7693	-1.8607
E_{pa}	3.8001	1.9987	0.2317
E_{pc}	8.5553	2.1653	2.6651
E_{da}	19.9097	9.2488	7.7373
E_{dc}	18.5374	9.0209	6.7137
V_{ss}	-9.0416	-6.8414	-5.8402
V_{xx}	6.8000	2.4485	1.2375
V_{xy}	8.6429	4.5432	3.6401
V_{pcsa}	6.8676	5.7843	4.2739
V_{pasc}	7.4512	4.3012	4.0837
V_{dapc}	9.2931	4.8533	4.0107
V_{dcpa}	0.0000	3.6816	3.6724

5.2 Electronic band structure of compounds

5.2.1 AlN

The zinc-blende structure of AlN is characterized by the lattice constant, a. At the first stage of the work, the equilibrium value of a is determined by calculating total energy of AlN by FP-LAPW for a set of volumes and fitting these to the Murnaghan equation [53]. We have adopted the value of 0.9 Å for Al and 0.846 Å for N as the MT radii. The electronic configuration of AlN is $Al: Ne (3s^2, 3p^1)$ and $N: He (2s^2 2p^3)$. In the calculations, the electrons of Al in $(1s^2 2s^2 2p^6)$ and in $(3s^2 3p^1)$ are defined as the core and valence band electrons, respectively. Similarly, the inner shell electrons of N in $(1s^2)$ are distinguished from the valence band electrons of N in $(2s^2 2p^3)$ shell. The equilibrium lattice

Table 5.2: The theoretical and experimental lattice constant values (a_{th} , a_{exp}) in Å for *AlN*, *ALAs* and *ALSb* in cubic phase.

<i>Compound</i>	a_{th}	a_{exp}
<i>AlN</i>	4.3956 ^a	4.365 ⁱ 4.38 ^j
	4.342 ^b	
	4.394 ^c	
	4.336 ^d	
	4.40 ^e	
	4.337 ^f	
	4.32 ^g	
	4.345 ^h	
<i>ALSb</i>	6.233 ^a	6.135 ⁿ
	6.06 ^{k,l}	
	6.127 ^m	
<i>ALAs</i>	5.738 ^a	5.652 ⁿ 5.660 ^t
	5.59 ^k	
	5.614 ^{l,o}	
	5.60 ^p	
	5.69 ^p	
	5.78 ^p	
	5.648 ^r	
	5.62 ^s	

^apresent work, ^bRef. [95], ^cRef. [97], ^dRef. [149], ^eRef. [103], ^fRef. [155], ^gRef. [101], ^hRef. [102], ⁱRef. [156], ^jRef. [157], ^kRef. [116], ^lRef. [159], ^mRef. [5], ⁿRef. [158], ^oRef. [168], ^pRef. [165], ^rRef. [166], ^sRef. [167], ^tRef. [164]

constant of c-*AlN* calculated in this work is given in Table 5.2 together with the experimental and other calculated lattice constant values of c-*AlN* presented in the literature.

The lattice constant of c-*AlN* obtained by the present volume optimization calculations seems to be accurate when compared with the available experimental value of 4.38Å [157]. The present lattice constant is approximately 0.68% greater than the other experimental value (4.365 Å) corresponds to X-ray diffraction

[156]. On the other hand, our lattice constant is very close to the lattice constant values of 4.394 Å [97] and 4.40 Å [103] calculated by plane wave pseudopotential (PWPP) and FP-LAPW methods, respectively. In both our and these calculations, the exchange correlation energy is defined by GG approximation. The present lattice constant of *c-AlN* is approximately (1.15 – 1.73)% greater than those calculated by FLMT0 [101, 102] and PWPP [95, 155] methods within LDA. The present value of *a* is also 1.36% greater than the lattice constant calculated by Hartree-Fock (HF) including density functional corrections [149].

At the second stage of the work, the FP-LAWP method within the frame work of the DFT has been employed to calculate the band structure *c-AlN*. Since the aim of this study extends to the calculation of the bowing parameters of ternary alloys correspond to *AlN*, we have focused mainly on the energy gaps at high symmetry points. It is found that, the band gap of *AlN* is indirect in zinc-blende phase, furthermore, the variation of energy bands is in agreement with the results of previous reports [95, 97, 143, 145, 146, 149, 152]. But, the present indirect band gap at X point (3.31 eV) is found to be narrower than its experimental value of 5.34 eV [151]. The same result was reported before [108]; the energy gaps calculated by DFT were found to be smaller than the corresponding experimental energy gaps. The present narrow energy gap of DFT at X point has been adjusted to the experimental indirect band gap of 5.34 eV [151] by addition of necessary energy corresponding to the effects which are not included in the calculations

initially. The adjusted energy band structure of *c-AlN* by FP-LAWP is shown in Fig. 5.1. Table 5.3. gives the important features of the present and previously reported band structures for *c-AlN* at high symmetry points. The energy gaps at Γ and L which are enlarged to the values 6.094 and 9.280 eV are in agreement with the results reported before [5, 143].

At the third stage of the work, the energy parameters of ETB have been derived for *c-AlN* from the band structure of DFT (Fig. 5.1) by the fitting process explained in sec. 2.4. The band structure of *c-AlN* recalculated by ETB is shown in Fig. 5.1. The important features of the band structure at high symmetry points are listed in Table 5.3. The close agreement between the band structure of *c-AlN* by ETB and DFT at Γ and X points (Fig. 5.1) carries out that, the energy parameters of ETB can be used surely to calculate the band structure of alloys corresponding to *c-AlN*. The present indirect energy gap which is fitted to the experimental value of 5.34 eV is close to the calculated values of 4.9 [143] and 5.49 eV [153]. In these theoretical works, the first principle quasiparticle GW calculations [143] and TB calculations [153] with $sp^3d^5s^*$ nearest neighbor model have been used for the band structure of *c-AlN*. In the present ETB work, the energy gaps are calculated to be 6.094, 5.34 and 8.150 eV at Γ , X and L symmetry points, respectively. The present energy gap value at Γ (E_g^Γ) is very close to the value of 6.00 eV calculated by first principles calculations with quasiparticle GW approach [143]. The present energy gap value at X (E_g^x) is 12.35% smaller than

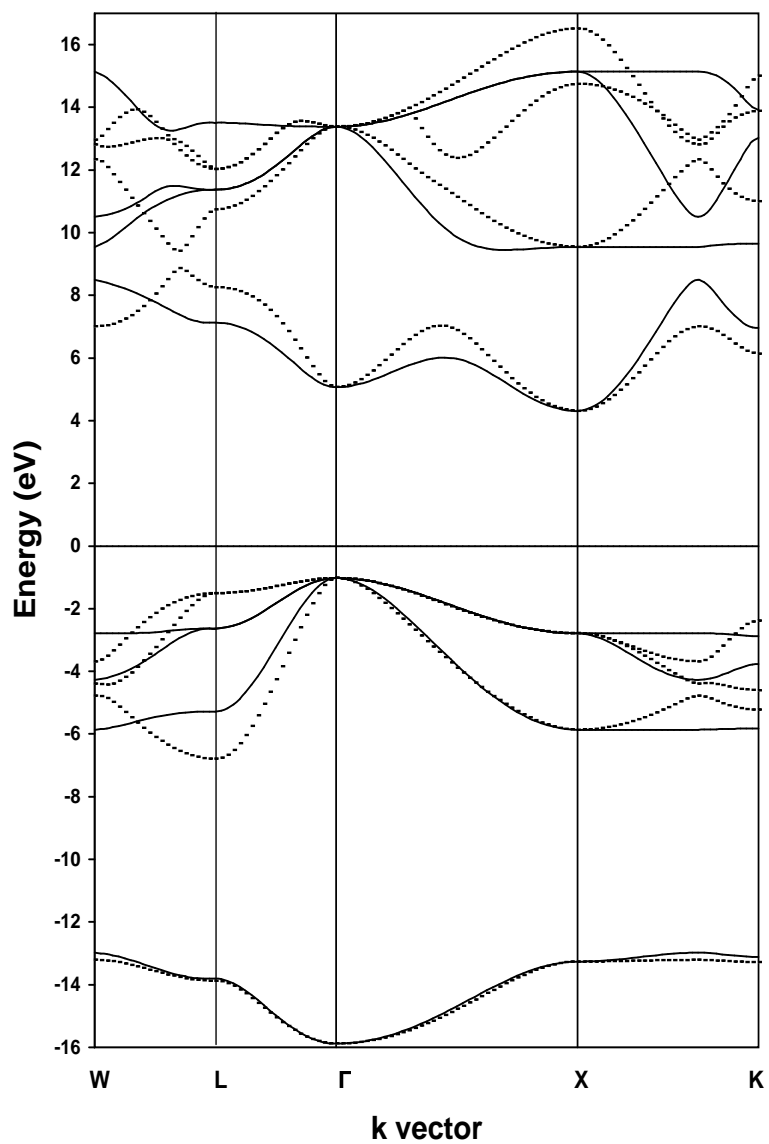


Figure 5.1: The energy band structure of *c-AlN* by FP-LAPW (adjusted) (dotted line) and ETB (solid line).

Table 5.3: A summary of the important features, energy gaps and valance bandwidths of the present DFT (adjusted) and ETB band structure for cubic AlN compared to other experimental and theoretical results. All energies are in eV.

	DFT^a (adjusted)	ETB^a	<i>theoretical</i>			<i>exp.</i>
			$LAPW^b$	LDA^c	GW^c	
Γ_1^v	-15.882	-15.882	-14.8	-15.1	-17.0	
Γ_{15}^v	-1.026	-1.026	0.01	0.0(3)	0.0(3)	
Γ_1^c	5.068	5.068	4.2	4.2	6.0	
Γ_{15}^c	13.381	13.381	12.3	12.3(3)	14.6(3)	
X_1^v	-13.266	-13.266	-12.0	-12.3	-14.3	
X_3^v	-5.862	-5.862	-4.9	-5.0	-5.6	
X_5^v	-2.786	-2.786	-1.8	-1.8(2)	-2.1(2)	
X_1^c	4.313	4.313	3.2	3.2	4.9	
X_3^c	9.545	9.545	8.4	8.4	10.5	
L_1^v	-13.885	-13.811	-12.7	-12.9	-14.9	
L_1^v	-6.798	-5.282	-5.9	-4.0	-6.7	
L_3^v	-1.506	-2.631	-0.5	-0.5(2)	-0.6	
L_1^c	8.254	7.124	7.3	7.3	9.3	
L_3^c	10.742	11.372	9.7	11.0(2)	13.2	
$\Gamma_{15}^v - \Gamma_1^c$	6.094	6.094	4.2 ^b 4.58 ^d 4.13 ^f	4.2 ^c 6.00 ^e	6.0 ^c 4.75 ^f	
$\Gamma_{15}^v - X_1^c$	5.34	5.34	3.2 ^b 3.40 ^d 4.35 ^h 4.5 ^k	3.2 ^c 4.45 ^g 3.31 ⁱ 6.2 ^k	4.9 ^{c,e} 4.26 ^g 5.49 ^j	3.38 ^d 5.34 ^l
$\Gamma_{15}^v - L_1^c$	9.280	8.150	7.3 ^b , 7.69 ^d	7.3 ^c	9.3 ^{c,e}	
$\Gamma_1^v - \Gamma_{15}^v$	14.856	14.856	14.8 ^b 15.01 ^g	15.1 ^c (14.83, 14.87) ⁱ	17.00 ^c 15.41 ^j	

^apresent work, ^bRef. [152], ^cRef. [143], ^dRef. [92], ^eRef. [5], ^fRef. [97], ^gRef. [149], ^hRef. [95], ⁱRef. [103], ^jRef. [153], ^kRef. [148], ^lRef. [151].

the corresponding value reported in Ref. [143]. In Vurgaftman *et al.* review paper [5] the energy gap of c-*AlN* at X and Γ points were recommended as 4.9 and 6.00 eV, respectively. The present energy gap values at Γ and L symmetry points are greater than the corresponding gaps calculated by DFT+LDA [143, 152], LMTO (linear muffin tin orbital)+LDA [92]. In the present work, the valance band width is calculated to be 14.856 eV which is very close to the values of 14.87 [103] and 14.8 eV [152] calculated by FP-LAPW method within the local density approach.

5.2.2 *AlSb*

AlSb which is always in the zinc-blende phase is characterized experimentally by the lattice constant value of 6.135 Å [158]. In the present work, the equilibrium lattice constant of *AlSb* is obtained by FP-LAPW following the same calculation steps defined in the previous section for *AlN*. In the FP-LAPW calculations, we have adopted the value of 0.9 Å for *Al* and 1.2 Å for *Sb* as the MT radii. The electronic configuration of *AlSb* is *Al*: *Ne* ($3s^2, 3p^1$) and *Sb*: *Kr* ($4d^{10}5s^25p^3$). The electrons of *Al* in ($1s^22s^22p^6$) and in ($3s^23p^1$) are defined as the core and valence band electrons, respectively. Similarly, the inner shell of *Sb* in ($1s^22s^22p^63s^23p^63d^{10}4s^24p^64d^{10}$) are distinguished from the valence electrons of *Sb* in ($5s^25p^3$). The equilibrium lattice constant of *AlSb* calculated in this work is given in Table 5.2 together with the experimental and other calculated lattice constant values given in the literature. The present lattice constant value

of 6.233 \AA is approximately 1.6% greater than the experimental value which is measured by X ray diffraction [158]. The lattice constant value of *AlSb* was given to be 6.06 \AA by PPPW calculations [159, 116]. The present value of *a* is also greater (2.85%) than the value of these theoretical works. On the other hand, the present value of *a* is 1.73 % greater than the recommended value given in Ref. [5].

The FP-LAPW method within the frame work of the DFT has been employed to calculate the band structure of *AlSb*. The band gap structure of *AlSb* is found to be indirect along $\Gamma - X$ direction. The variation of the bands is similar with the results given in the literature [82, 150, 154]. But, as it is obtained for *AlN*, the band gap of *AlSb* E_g^Δ by DFT is small (1.287 eV) with respect to its experimental value of 1.686 eV at 27 K [158, 160]. Similar result is found for the energy gap at Γ ; it is smaller than corresponding energy gap (2.384 eV) measured at 25 K [160]. In the present work, the calculated narrow indirect gap of *AlSb* along the $\Gamma - X$ is adjusted to the corresponding experimental value as it is explained in Ref. [108]. The adjusted band structure of *AlSb* is shown in Fig. 5.2. The adjusted energy gap is located at 0.825% of the way along $\Gamma - X$. The energy gaps at L and Γ are found to be 1.981 and 2.526 eV with respect to the broadened indirect energy gap, respectively. The order between the energy gaps, $E_g^\Gamma > E_g^L > E_g^\Delta$ is the same as it was reported in Refs. [147, 161, 162]. Table 5.4 gives the important features of the present and previously reported band structures for *AlSb* at high symmetry

points. In the present work, the ETB energy parameters needed for the band structure calculations of ternary alloys corresponding to *AlSb* have been derived from the adjusted DFT eigenvalues (Table 5.4) by a fitting process explained in sec. 2.4. The band structure of *AlSb* recalculated by ETB is shown in Fig. 5.2. The important features of the band structure are listed in Table 5.4. The energy gaps at Δ and Γ points (1.659 and 2.526 eV) are approximately the same for ETB and DFT, results. (Fig. 5.2). The present indirect energy gap with the value of 1.659 eV is located at $K_x = 0.45, K_y = K_z = 0$ along $\Gamma - X$ direction. The same position was obtained in Ref. [150] by TB calculations within the genetic algorithm. The present value of E_g^Δ by ETB calculations is (0.54-15.28)% smaller than the measured and calculated values reported in Ref. [141, 116, 160, 161, 158]. The present E_g^Δ is only 2.72% greater than the corresponding value of TB-genetic algorithm [150]. The present E_g^L is 21.28% greater than its experimental value of 2.33 eV [162]. On the other hand, the width of the present valence band (9.893 eV for both DFT and ETB) is closer to the corresponding values of DFT+LDA [77] and TB-genetic algorithm approaches [150] than that of the PP method given in Ref. [147].

5.2.3 AlAs

In the present work, the equilibrium lattice constant of *AlAs* corresponding to the total energy minimization has been found to be 5.738 Å by FP-LAPW

Table 5.4: A summary of the important features, energy gaps and valance bandwidths of the present DFT (adjusted) and ETB band structure for *AlSb* compared to other experimental and theoretical calculations results. All energies are in eV.

	DFT^a	ETB^a	<i>theoretical</i>			<i>exp.</i>
	(<i>adjusted</i>)		DFT^b	PP^c	TB^d	
Γ_1^v	-10.180	-10.180	-10.77	-11.10	-10.975	
Γ_{15}^v	-0.287	-0.287	0.00	0.00	0.00	0.00 ^e
Γ_1^c	2.239	2.239	2.05	2.23	2.3	2.38 ^e
Γ_{15}^c	3.184	3.184	3.50	3.52	5.075	3.740 ^e
X_1^v	-8.036	-8.036	-8.72	-9.09	-6.995	
X_3^v	-5.639	-5.639	-5.44	-6.01	-3.192	-2.80 ^f
X_5^v	-2.390	-2.390	-2.31	-2.54	-2.858	-2.40 ^f
X_1^c	1.573	1.573	2.08	1.64	1.632	1.69 ^e
X_3^c	1.579	1.579	3.02	1.84	2.614	
L_1^v	-8.085	-8.606	-9.30	-9.70		
L_1^v	-5.438	-4.697	-5.58	-5.91		
L_3^v	-1.165	-2.060	-0.90	-1.48		
L_1^c	1.695	2.539	1.94	1.84		
L_3^c	3.823	2.591	4.84	4.29		2.33 ^e
$\Gamma_{15}^v - \Gamma_1^c$	2.526	2.526	2.05 ^b 2.384 ^g 2.11 ⁱ	2.23 ^c 2.30 ^h	2.3 ^d 1.41 ⁱ	2.384 ^k 2.30 ^k
$\Gamma_{15}^v - \Delta$	1.685	1.659	1.615 ^d 1.06 ⁱ 2.009 ^j	1.686 ^g 1.53 ⁱ	1.57 ^h 1.956 ^j	1.686 ^k 1.62 ^k 1.65 ^l
$\Gamma_{15}^v - L_1^c$	1.981	2.826	1.94 ^b 2.327 ^g	1.84 ^c	3.476 ^d	2.33 ^e
$\Gamma_1^v - \Gamma_{15}^v$	9.893	9.893	10.77 ^b	11.10 ^c	10.975 ^d	

^a present work, ^b Ref. [77], ^c Ref. [147], ^d Ref. [150], ^e Ref. [162], ^f Ref. [163], ^g Ref. [141], ^h Ref. [82], ⁱ Ref. [154], ^j Ref. [116], ^k Ref. [158, 160], ^l Ref. [161].

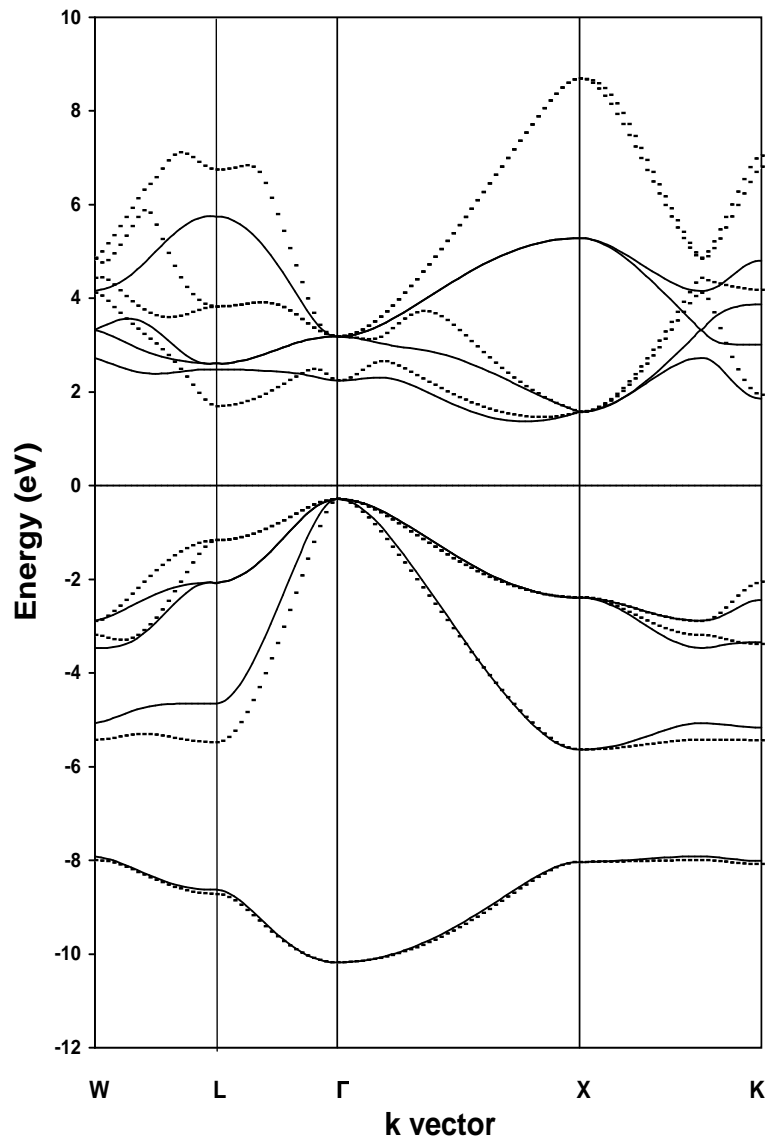


Figure 5.2: The energy band structure of *AlSb* by FP-LAPW(adjusted) (dotted line) and ETB (solid line).

calculations based on DFT within GG approximation. In FP-LAPW calculations, we have adopted the value of 0.85\AA for *Al* and 1.15\AA for *As* as the MT radii. The electronic configuration of *AlAs* is *Al*: $Ne (3s^2, 3p^1)$ and for *As*: $Ar (3d^{10}4s^24p^3)$. The electrons of *Al* in $(1s^22s^22p^6)$ and in $(3s^23p^1)$ are defined as the core and valence band electrons, respectively. Similarly, the inner shell of *As* in $(1s^22s^22p^63s^23p^63d^{10})$ are distinguished from the valence electrons of *As* in $(4s^24p^3)$. The experimental, present and other calculated lattice constant values of *AlAs* are given in Table. 5.2. The present lattice constant value is approximately 1.37 % and 1.52 % greater than the values of 5.6606\AA [164] and 5.652\AA [158] measured at $T=0^\circ\text{C}$ and $T=0\text{ K}$, respectively. On the other hand, the present value of a is $(0.84 - 2.64)\%$ greater than its calculated values reported in Refs. [116, 159, 165–168]. The present lattice constant is normally much closer to those of DFT within GGA functional of Perdew and Wang (PW) [165] and Hamprecht, Cohen, Tozer and Handy (HCTH) [165] than the values of DFT calculated by LD approximation [159, 165, 166].

In the present FP-LAPW calculations, the energy gap of *AlAs* is indirect at X point. In most of the theoretical works [108, 116, 147, 165, 168, 169, 170], the indirect energy gap of *AlAs* located at X point, but in Refs. [5, 150, 159], it located along $\Gamma - X$ direction. In the present work, the energy gap at L point is found to be larger than the direct gap (E_g^Γ); this result is consistent with some calculations [147, 166, 169, 170] and in disagreement with others [5, 147, 150, 168]

in which E_g^L is smaller than E_g^Γ . The present E_g^X (1.860 eV) and E_g^Γ (2.526 eV) are found to be smaller than the available experimental energy gaps [162, 170] at X and Γ points. As it is done for both *AlN* and *AlSb*, the discrepancy between the present and experimental energy gap of *AlAs* at X point has been lowered by fitting the present indirect energy gap to its experimental value of 2.25 eV [171].

Fig. 5.3 shows the band structure of *AlAs* with adjusted energy gaps at X, Γ and L points. The important features and adjusted energy gaps of DFT calculations for *AlAs* are given in Table 5.5.

In the present work, the ETB energy parameters necessary for the electronic band structure of ternary alloys correspond to *AlAs* have been derived from the present eigen values of DFT (adjusted), by least square fitting. The recalculated band structure of *AlAs* by ETB has been shown in Fig. 5.3. The important features and energy gaps of ETB calculations are listed in Table 5.5 together with the experimental and other calculational values for comparison. In both present ETB and adjusted DFT calculations, the energy gap at Γ point is found to be 2.815 eV. The value of the present direct band gap is (6.7 - 12.30)% smaller than the direct band gap values reported by TB calculations within generic [150], Slater-Koster [147] and semi-empirical [168] algorithms. On the other hand the present E_g^Γ is (0.89 - 12.6)% greater than the corresponding values given by ETB-orthogonal plane wave (OPW) [169] and DFT-LDA calculations [170]. The value of present E_g^L (3.566 eV) is approximately (0.75 - 1.2 eV) greater than

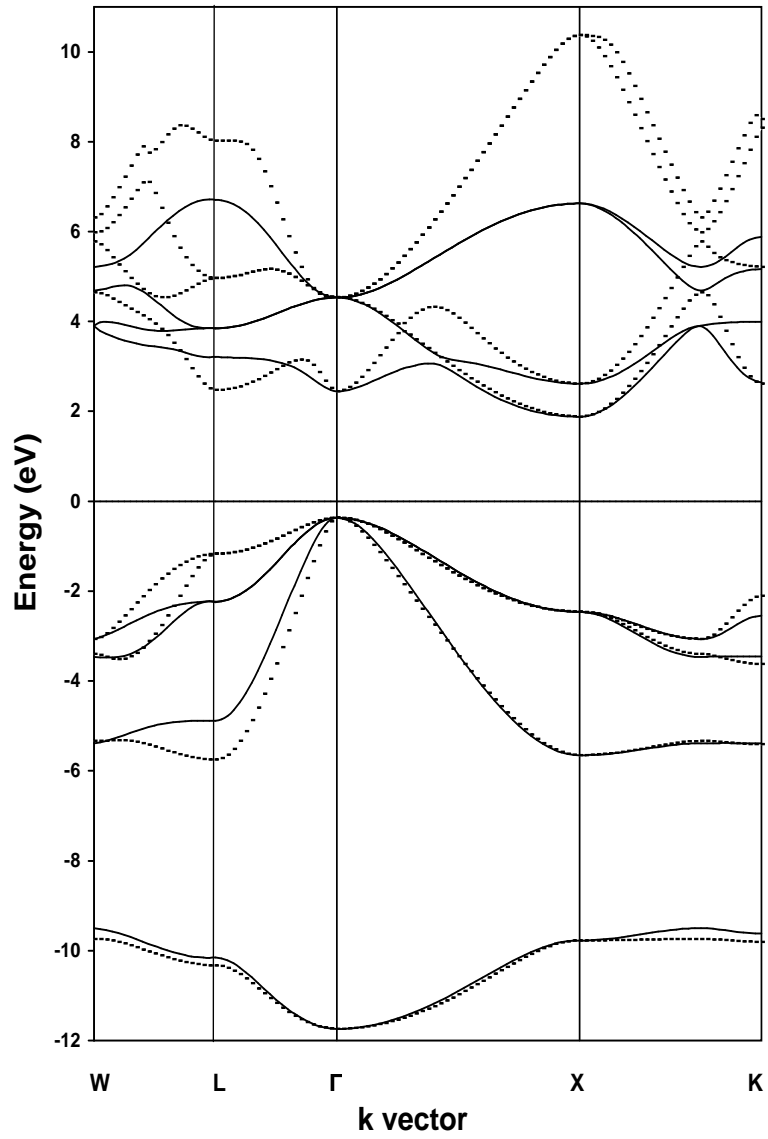


Figure 5.3: The energy band structure of *AlAs* by FP-LAPW (adjusted) (dotted line) and ETB (solid line).

Table 5.5: A summary of the important features, energy gaps and valance bandwidths of the present DFT (adjusted) and ETB band structure for *AlAs* compared to other experimental and theoretical calculations results. All energies are in eV.

	<i>DFT</i> ^a (adjusted)	<i>ETB</i> ^a	<i>theoretical</i>			<i>exp.</i>
			<i>ETB</i> ^b (<i>GF</i>)	<i>ETB</i> ^c	<i>DFT</i> ^d (<i>LCAO</i>)	
Γ_1^v	-11.741	-11.741	-11.66	-11.48	-11.95	
Γ_{15}^v	-0.369	-0.369	0.00	0.00	0.00	
Γ_1^c	2.448	2.448	3.21	2.50	2.79	
Γ_{15}^c	4.532	4.532	4.57	4.57	4.48	
X_1^v	-9.776	-9.776	-9.42	-9.61	-9.63	
X_3^v	-5.652	-5.652	-5.54	-5.20	-5.69	
X_5^v	-2.462	-2.462	-1.97	-2.01	-2.38	
X_1^c	1.882	1.882	2.25	2.38	2.37	
X_3^c	2.614	2.614	2.61	2.81	3.84	
L_1^v	-10.331	-10.159	-10.21	-10.14	-10.28	
L_1^v	-5.750	-4.880	-5.87	-5.22	-5.95	
L_3^v	-1.172	-2.230	-0.71	-0.80	-0.88	
L_1^c	2.512	3.198	2.73	2.57	2.81	
L_3^c	3.823	3.850	4.58	5.25	5.86	
$\Gamma_{15}^v - \Gamma_1^c$	2.815	2.815	3.21 ^b 3.018 ^e 2.048 ^g	2.50 ^c 3.130 ^f 2.9 ^h	2.79 ^d 2.88 ^f 3.14 ^h	3.13 ⁱ
$\Gamma_{15}^v - X_1^c$	2.25	2.25	2.25 ^b 2.171 ^{Δ,e} 2.23 ^{Δ,h} 1.32 ^k 1.81 ^k 2.32 ^m	2.38 ^c 2.223 ^f 2.25 ^{Δ,h} 1.42 ^k 1.66 ^k 2.543 ⁿ	2.37 ^d , 2.14 ^f 1.26 ^k 1.39 ^k 2.18 ^l	2.229 ⁱ 2.25 ^j
$\Gamma_{15}^v - L_1^c$	3.566	3.566	2.73 ^b 2.351 ^e 2.35 ^h	2.57 ^c 2.581 ^f 2.53 ^h	2.81 ^d , 2.91 ^f	
$\Gamma_1^v - \Gamma_{15}^v$	11.373	11.373	11.66 ^b 15.728 ^e	11.48 ^c 12.020 ^h	11.95 ^d 12.41 ^h	

^a present work , ^b Ref. [79], ^c Ref. [172], ^d Ref. [77], ^e Ref. [150], ^f Ref. [147], ^g Ref. [159], ^h Ref. [5], ⁱ Ref. [162], ^j Ref. [170], ^k Ref. [165], ^l Ref. [108], ^m Ref. [158] , ⁿ Ref. [116]

the corresponding values given in the literature [5, 147, 150, 168–170]. The discrepancies between the present and experimental [162] energy gaps at Γ and L points are approximately 10.0% and 40.0%, respectively. The present valence bandwidth value of 11.373 eV (Table 5.5) is very close to the values given by ETB-OPW [169], ETB-LCAO [168] and DFT-LDA [170] calculations. Therefore, the present ETB energy parameters of *AlAs* can be considered to be weak for the L point, but they are sufficiently strong to give the valence bandwidth and the energy gaps at X and Γ symmetry points.

5.3 Electronic structure of ternary alloys

5.3.1 $Al_{1-x}In_xN$

Although most of the work reported so far refers to the stable wurtzite phase of the $Al_{1-x}In_xN$ alloys, the metastable cubic modification arises as an alternative for device applications. The successful growth of cubic $Al_{1-x}In_xN$ films [171] was followed by the theoretical investigations on their thermodynamical structural and electronic properties [173–178].

In the present work, the electronic structures of $Al_{1-x}In_xN$ alloys in cubic phase have been calculated by ETB. Wright and Nelson [173] showed that Vegard’s law [57] is valid to define the unit cell of the $AlInN$ alloy; because the equilibrium unit cell volume was only 0.4% smaller than its average value. By considering this fact, here we simply used the Vegard’s law equation (Eq. 2.53)

to obtain the indium concentration (x) dependent lattice constant values (a_{av}) of $Al_{1-x}In_xN$ alloys corresponding to the lattice constant values of AlN (4.395\AA) and InN (4.967\AA) (present work, Table 5.2). Since only the nearest neighbor interactions are taken into account, the disposable interaction parameters of ETB obtained for AlN and InN are sufficiently used for the electronic structure calculations of $Al_{1-x}In_xN$ alloys as explained in sec. 2.4.

The variation of the direct and indirect band gap energies (E_g^Γ and E_g^X) as a function of In concentration (x) is plotted in Fig. 5.4 for $Al_{1-x}In_xN$ in zinc blende phase. Fig. 5.4 also comprises the average E_g^Γ and E_g^X values of concentration (x), by using the band gap energies of $Al_{1-x}In_xN$ alloys calculated as a function of AlN ($E_g^\Gamma = 6.094$ eV and $E_g^X = 5.34$ eV) and InN ($E_g^\Gamma = 0.59$ eV and $E_g^X = 3.375$ eV) (Table 3.3). The values of the E_g^Γ and E_g^X have been found to be deviated from the linear behavior of E_g^Γ (av) and E_g^X (av). In view of Fig. 5.4, we note that the overall bowing for both Γ and X point transitions are small and downward. The small deviation of E_g from linearity might be explained by small mismatching between the lattice constant values of AlN and InN . In the present work, the bowing parameter, b , which shows the deviation of E_g from linearity has been calculated by the best fit of our results to Eq. 2.57. The resulting bowing parameters for E_g^Γ and E_g^X of $Al_{1-x}In_xN$ alloy are given in Table 5.6. The corresponding bowing parameters reported in Refs. [101, 173, 174, 176, 178, 180–182] are listed in Table 5.6 for comparison. In general, the bowing parameters

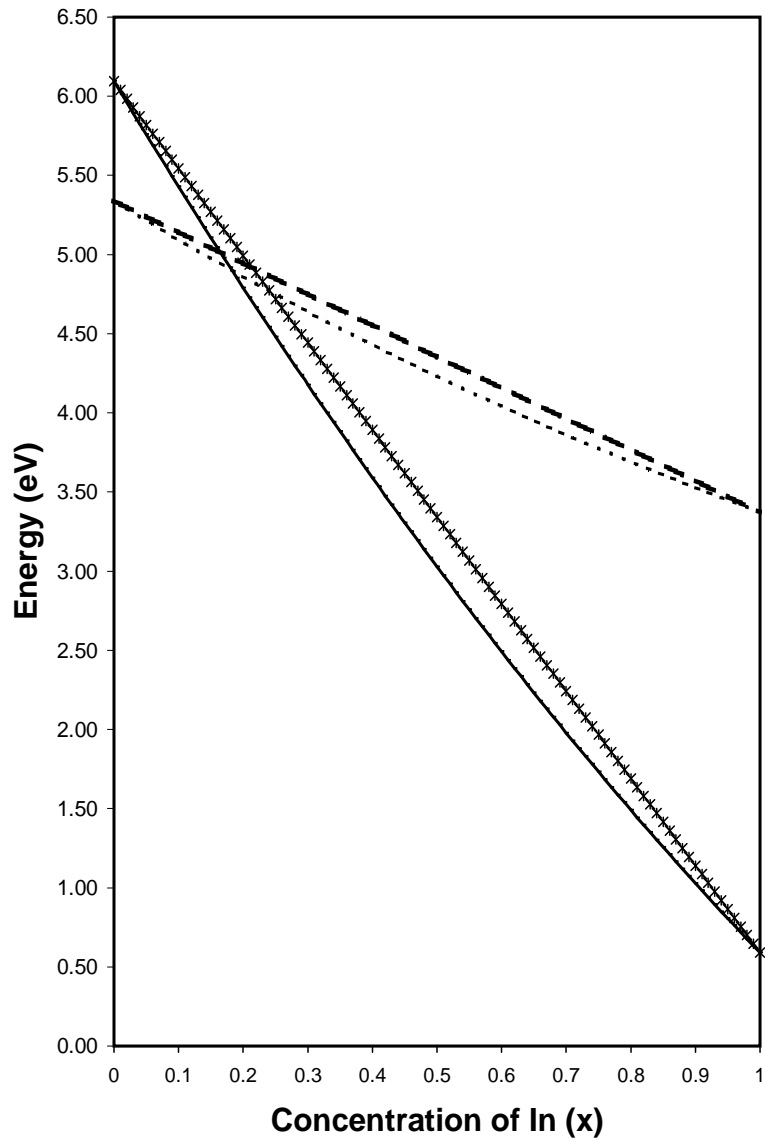


Figure 5.4: Dependence of E_g^Γ (solid line), E_g^X (dotted line), $E_g^\Gamma(av)$ (zig-zag line) and $E_g^X(av)$ (dashed line) of $Al_{1-x}In_xN$ on the In composition (x).

Table 5.6: The bowing parameters (in eV) for direct and indirect transitions of alloys at Γ and X symmetry points

<i>Alloys</i>	$b(E_g^\Gamma)$	$b(E_g^X)$
$Al_{1-x}In_xN$	1.2521 ^a 2.53 ^{b,c,d} 1.32 ^e 2.729 ^f 6.9 ^g 3.5 ^h 2.384 ⁱ 2.726 ^j 2.5 ^k	0.5051 ^a 1.45 ^b -0.51 ^e 3.624 ^f 0.61 ^k
$Al_{1-x}In_xSb$	0.578 ^a 0 - 0.43 ^l 0.445 ^j	0.609 ^a
$Al_{1-x}In_xAs$	2.664 ^a 0.729 ^j 0.24 - 0.74 ^l 0.52 ^m 0.74 ⁿ 0.24 ^o 0.86 ^p	3.324 ^a -0.5 - 0.0 ^l

^apresent work, ^bRef. [174], ^cRef. [173], ^dRef. [179], ^eRef. [176], ^fRef. [178], ^gRef. [180], ^hRef. [101], ⁱRef. [181], ^jRef. [182], ^kRef. [139], ^mRef. [190], ^lRef. [5], ⁿRef [188], ^oRef. [158], ^pRef. [189]

obtained previously at Γ and X points for $Al_{1-x}In_xN$ alloys are high because of using high energy gaps for both InN and AlN at the end points [101, 139, 173, 174, 176, 179–182]. The bowing parameters obtained for wurtzite $Al_{1-x}In_xN$ alloys by optical absorption spectroscopy [101, 181, 180, 183] are evidently larger than those of cubic $Al_{1-x}In_xN$ alloys studied by either empirical [174, 177] or first principles calculations [173, 175, 176, 178]. The present bowing parameter (1.252 eV) predicted for the energy gap along $\Gamma \rightarrow \Gamma$ of $Al_{1-x}In_xN$ alloy is close to the value of b (1.32 eV) predicted by the results of first principle calculations [176]. On the other hand, the energy gap calculated by optical absorption spectroscopy [184] for wurtzite $Al_{1-x}In_xN$ alloys was found to be 5.80, 5.48 and 5.26 eV for the concentrations ($x = 0.01, 0.04$ and 0.08), while in the present work, the calculated energy gap for the same concentrations ($x = 0.01, 0.04$ and 0.08) is found to be 5.315, 5.240 and 5.142 eV, respectively. The present energy gaps of *c*- $AlInN$ are normally smaller than those of wurtzite $AlInN$. The direct energy gaps calculated by pseudopotential formalism within Virtual Crystal Approximation (VCA) [174] were 5.29 and 4.87 eV for $Al_{0.92}In_{0.08}N$ and $Al_{0.83}In_{0.17}N$ alloys, respectively. The values are greater than the calculated values in this work by 0.95% and 1.1%, respectively. In the present work, the predicted bowing parameter of E_g^X is positive and its numerical value (0.505 eV) is close to the corresponding value of 0.61 eV reported in Ref. [139].

In the present work, the indirect to direct band gap transition has been examined and found that the X to Γ energy gap transition occurs at $x = 0.185$. Hence the cubic $Al_{1-x}In_xN$ is a direct band gap semiconductor when the In concentration x is greater than 0.185. This boundary of concentration was predicted to be 0.18 [173], 0.19 [176], 0.244 [178] and 0.5 [174] in other reports. Since the bowing parameter for E_g^Γ is similar with the corresponding value reported in Ref. [176], the indirect to direct band gap transition is occurred at approximately $x \approx 0.19$ by both calculations.

5.3.2 $Al_{1-x}In_xSb$

Although $Al_{1-x}In_xSb$ alloys have been well known potential materials for the fabrication of multiple quantum lasers [38], photovoltaic cells and photodetectors [39] they have not been extensively studied in the literature. However, to fully characterize these photonic and high speed electronic devices, it is necessary to know the energy band structure of $Al_{1-x}In_xSb$ as a function of either Al or In concentration accurately. In an early work [185], the variation of E_g^Γ as a function of x ranging from 0.10 to 0.60 measured by absorption spectroscopy for $Al_{1-x}In_xSb$ at 300 K. In subsequent electroreflectance measurement, the variation of E_g^Γ was given by Isomura *et al.* [186], for $InSb$ rich $Al_{1-x}In_xSb$ at 300 K. In a recent work [187], the fundamental energy gap has been determined for

$Al_{1-x}In_xSb$ alloy system in the Al concentration range from 0 to 0.25 by transmission spectroscopy at both 300K and 4.2 K. In another recent work [102], the optical band gap bowing has been calculated by a phenomenological model focusing to $x=0.5$ of $Al_{1-x}In_xSb$. According to the best knowledge of authors, there is not any systematical work in the literature studying the electronic band structure of $Al_{1-x}In_xSb$ alloy system theoretically, starting from the electronic band structure of constituents ($AlSb$ and $InSb$). In the present work, the unit cell volume of the $Al_{1-x}In_xSb$ has been defined [57] depending on In concentration x and the lattice constant values of $AlSb$ (6.233\AA) and $InSb$ (6.643\AA) (present work). The electronic band structure calculations of $Al_{1-x}In_xSb$ alloys system have been performed by ETB as explained in sec. 2.4. In electronic band structure calculations of $Al_{1-x}In_xSb$ alloys, the present energy parameters are used for $AlSb$ and $InSb$, respectively, for this purpose.

Fig. 5.5 displays the variation of the direct and indirect band gap energies as a function of In concentration x . In the same figure, the variation of average direct and indirect energy gaps are given as a function of In concentration x for comparison. In view of Fig. 5.5, we note that the overall bowing for Γ point transition is small and downward. Similarly, bowing for X point transition is downward but the values of E_g^x are highly deviated from the corresponding values of $E_g^X(av)$. The calculated bowing parameters by the best fit of our results to the expression

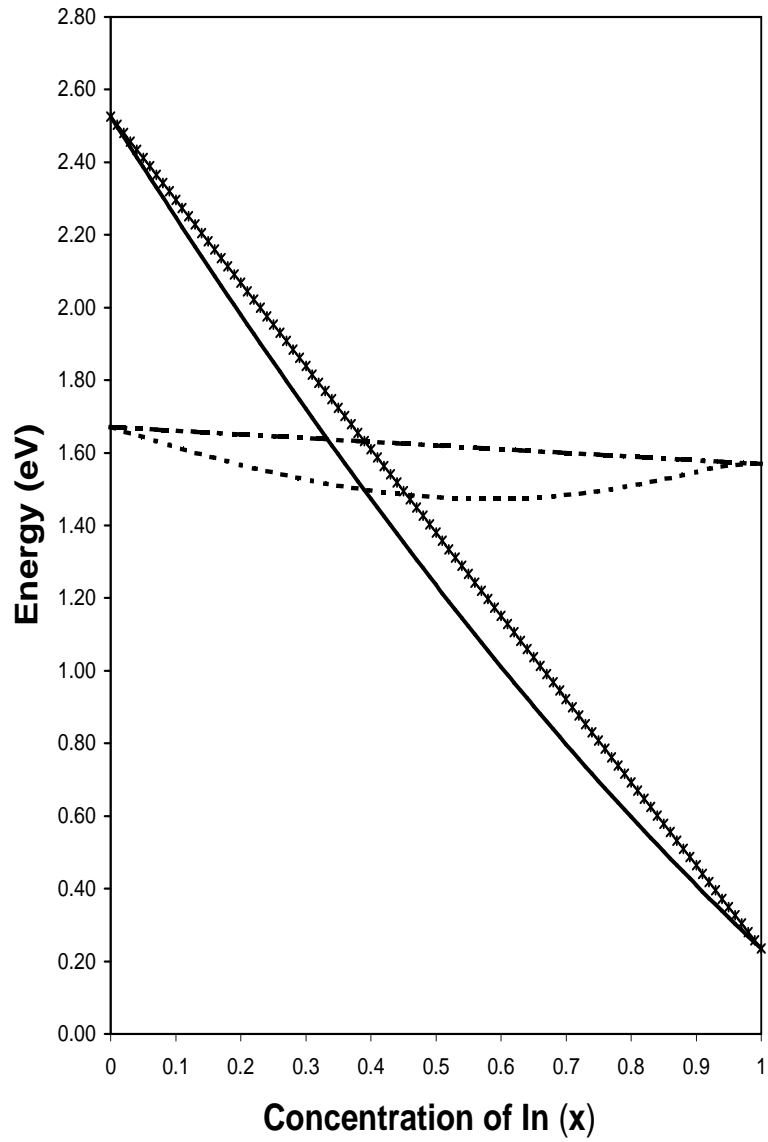


Figure 5.5: Dependence of E_g^Γ (solid line), E_g^X (dotted line), $E_g^\Gamma(av)$ (zig-zag line) and $E_g^X(av)$ (dashed line) of $Al_{1-x}In_xSb$ on the In composition (x).

given in Eq. 2.57 are 0.578 and 0.609 eV for E_g^Γ and E_g^X , respectively. The variation of E_g^Γ was exactly linear in the room temperature absorption measurements of *InSb* rich $Al_{1-x}In_xSb$ alloys [185, 187]. However, in the electroreflectance measurements [186], the variation of E_g^Γ deviated from the linear behavior with the bowing parameter of 0.43 eV. Since the electroreflectance measurements was considered to be more precise than the absorption measurements, the range of 0-0.43 eV was recommended for the bowing parameter of E_g^Γ in Ref. [5]. The present bowing parameter (0.578 eV) for the variation of E_g^Γ is not in this recommended range, and it is 30% greater than the bowing parameter given in Ref. [182]. Since the variation of E_g^X as a function of *In* concentration *x* was not studied in the literature, we are not able to compare our bowing parameter of E_g^x . The present bowing parameters for E_g^Γ and E_g^X of $Al_{1-x}In_xSb$ alloy are given in Table 5.6 together with the corresponding values given in the literature.

In view of Fig. 5.5, the X and Γ valleys cross at a composition of $x=0.39$. Therefore $Al_{1-x}In_xSb$ has direct transition after $x=0.39$. This composition is in good agreement with the crossover composition reported in Ref. [185].

5.3.3 $Al_{1-x}In_xAs$

The electronic band structure of $Al_{1-x}In_xAs$ alloy with the indium concentration around 0.52 has been intensively studied in the literature, because of its application in $Ga_{0.47}In_{0.53}As/Al_{0.48}In_{0.52}As$ heterostructure system that is lattice

matched to InP . Furthermore, the energy band gap variation of $AlInAs$ at Γ symmetry point has been also studied for the full range of the indium concentration both experimentally [5, 158, 188, 189] and theoretically [182, 190].

In the present work, the electronic band structure of $Al_{1-x}In_xAs$ alloys in cubic phase has been calculated by ETB as explained in sec. 2.4. The Vegard's law equation (Eq. 2.53) has been employed to calculate the In concentration (x) dependent lattice constant (a_{av}) values of $Al_{1-x}In_xAs$ alloys corresponding to the lattice constant value of $AlAs$ (5.738\AA) and $InAs$ (6.195\AA)(present work) binaries. The energy parameters used in the present ETB calculations (correspond to sp^3d^2 orbitals) are reported in the present work for $AlAs$ and $InAs$, respectively.

The variation of the direct and indirect band gap energies (E_g^Γ and E_g^X) as a function of In concentration x is plotted in Fig. 5.6 for $Al_{1-x}In_xAs$.

Fig. 5.6 also comprises the average band gap energies of $Al_{1-x}In_xAs$ alloys calculated as a function of concentration x , by using the band gap energies of $AlAs$ ($E_g^\Gamma = 2.815eV$ and $E_g^X = 2.25eV$)(Table 5.5) and $InAs$ ($E_g^\Gamma = 0.417eV$ and $E_g^x = 1.787eV$)(Table 3.4). In view of Fig. 5.6, we note that the overall bowing for both Γ and X point transition is large and downward. The predicted bowing parameters by the best fit of our results to the expression given in Eq. 2.57 are 2.664 eV and 3.324 eV for E_g^Γ and E_g^X , respectively. The present bowing parameters for E_g^Γ and E_g^X of $Al_{1-x}In_xAs$ alloy are given in Table 5.6 together with the corresponding values reported in Refs. [5, 158, 182, 188, 189, 190] for

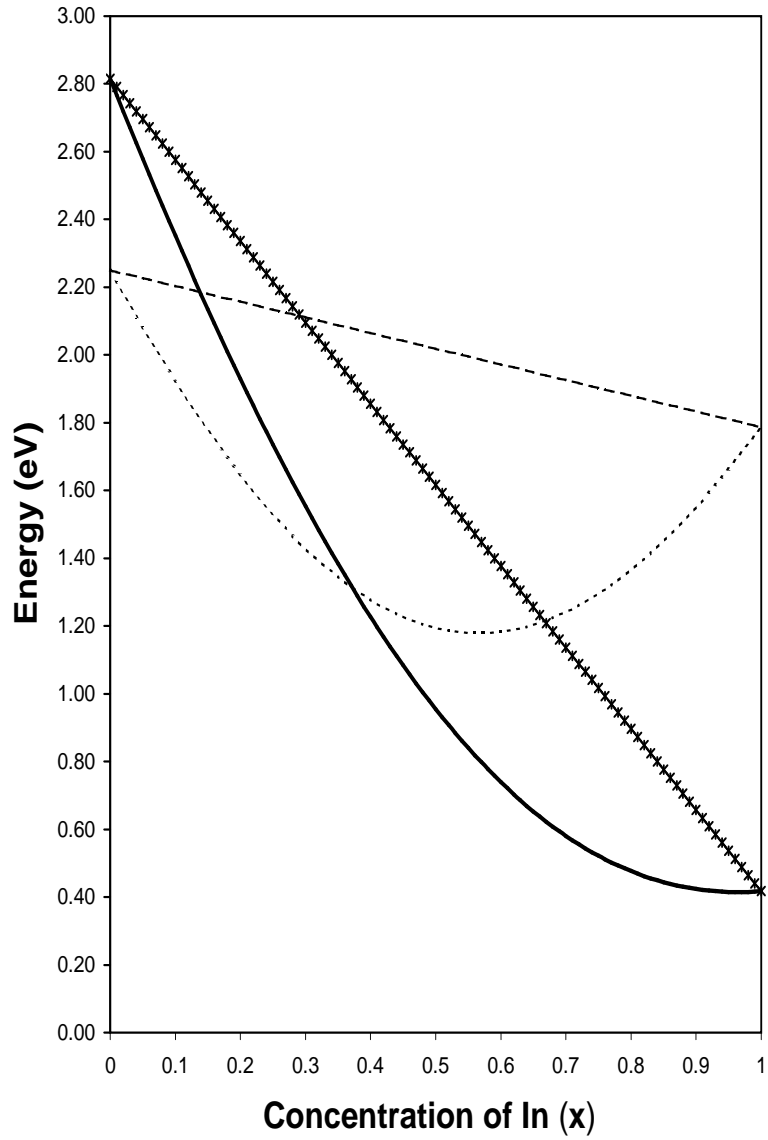


Figure 5.6: Dependence of E_g^Γ (solid line), E_g^X (dotted line), $E_g^\Gamma(av)$ (zig-zag line) and $E_g^X(av)$ (dashed line) of $Al_{1-x}In_xAs$ on the In composition (x).

comparison. The all bowing parameters of E_g^Γ predicted by theoretical results [182, 190] and experimental observations [158, 188] are in the range (0.24–0.74eV) recommended in Ref. [5]. But the bowing parameter of 0.86 eV predicted by ellipsometric study [189] is outside of this range. The present bowing parameter of $Al_{1-x}In_xAs$ for E_g^Γ has found to be also bigger than the recommended range.

In view of Fig. 5.6, the X and Γ valleys cross at a composition of $x = 0.38$. On the other hand the present bowing parameter of E_g^x is positive in contrast to the negative value of its recommended value given in Ref. [5]. Furthermore, the present calculated bowing parameter of E_g^X for each In concentration x is in the range of 3.072-3.296 eV.

CHAPTER 6

THE ELECTRONIC BAND STRUCTURE OF GaN AND GaAs COMPOUNDS

6.1 Introduction

Gallium nitride (*GaN*) is an attractive material for microelectronic and optoelectronic applications. *GaN* with the band gap of 3.1 - 3.5 eV is a very promising material for a large range of applications, such as emitters and detectors for visible and UV light, for high frequency, high temperature and power devices [6, 191–193]. The stable *GaN* has been grown in hexagonal (h) (wurtzite, α phase) structure. However, the production of *GaN* thin films of cubic (c) (zinc-blende, β phase) crystals has been satisfied by the recent progress in crystal growth techniques. Recently, the high quality pure *c-GaN* epilayers of several μm have been successfully grown on MgO (1 \times 1) [194], 3C-SiC(100) [195, 196, 197, 198, 199, 200, 201], GaAs (100)[198, 199, 202, 203], Si-doped GaAs (100) [204], and Si(100) [205] by gas phase and plasma assisted molecular beam epitaxy (MBE) [194–205] and metalorganic chemical vapor deposition (MOCVD) [202, 204].

The interest in *c-GaN* has been growing recently. Because the *c-GaN* has

some attractive advantages for device applications such as higher electron drift velocity [203] and lower band gap energy than w-*GaN* [194–200, 202]. The fundamental band gap of *c-GaN* was measured to be 3.35, 3.26 and 3.216 eV at room temperature by photoluminescence (PL) spectra reported in Refs. [197, 198, 202], respectively. The room temperature band gap value of *c-GaN* was 3.45, 3.272 and 3.2 eV in cathodoluminescence (CL) and optical absorption measurements reported in Refs. [195, 198, 203], respectively. In modulated photoreflectance measurements [194], the room temperature direct gap of *GaN* was 3.231 eV. Petalas *et al.* [205] measured the room temperature band gap as 3.17 eV by spectroscopic ellipsometry. All these band gap values are greater than 3.0 eV and smaller than the room temperature band gap values of w-*GaN* (3.5 eV) [167] measured in the same experimental setups. The discrepancies between the measured band gaps may originate from different crystal quality, such as background carrier concentrations and inhomogeneity of epilayers.

On the other hand, the fundamental band gap of *c-GaN* was measured to be 3.268, 3.291 and 3.302 eV at 10 K by PL [194, 202] and modulated photoreflectance [194] measurements, respectively.

In the literature, there are large theoretical efforts to properly describe the structural and electronic properties of *c-GaN* [92, 94, 97, 103, 143, 167, 205–214]. But yet, there is no fully consistent result, especially on the fundamental gap of the compound. The direct band gap values by density functional theory

(DFT) within local density approximation (LDA) were found to be smaller than the measured values; the difference is approximately 1.5 eV. The underestimated value of the band gap was improved by quasiparticle correction GW (dressed Green's function, G , and dynamical screened interaction, W) functional correction in Ref. [143] and the difference was decreased to ~ 0.2 eV. In Ref. [94] the improved band gap value of *c-GaN* was found to be 3.8 eV by self interaction and relaxation corrections. In both DFT - linear muffin thin orbital (LMTO) and DFT - full potential linear augmented plane wave (FP-LAPW) generalized gradient approximation (GGA) calculations, the band gap values were found around 2.4 eV [205, 210]. The empirical pseudopotential band structure calculations for *c-GaN* have predicted the room temperature band gap values which are 0.3 -0.1 eV less than that of *w-GaN* [206, 208].

GaAs is an ideal material for high speed and optoelectronic devices. Because the emission of light is very effective and the electron mobility is very high in *GaAs* compared to other semiconductors. Besides, due to the nearly perfect lattice match of *GaAs* to *AlAs*, it is possible to grow superlattices, heterostructures and alloys from *GaAs* and *AlAs* in order to create a new artificial materials with tunable electronic and optical properties. The structural and ground state electronic properties of bulk or epitaxially grown *GaAs* have been studied by X-ray photoemission [71, 215], electroreflectance [216], angle resolved photoemission [217], ellipsometry [218] and PL [219–221] measurements. *GaAs* is a direct

band gap material with $E_g^\Gamma < E_g^L < E_g^X$ ordering provided by a direct proof in electroreflectance measurements [216]. The fundamental band gap of *GaAs* was measured to be 1.632 eV at He temperature by angle-resolved photoemission [217], E_g^Γ was 1.5189 eV at 1.6 K with the scanning rotating analyzer ellipsometer [218]. In Refs. [220, 221], the PL spectra of *GaAs* were measured as a function of temperature and the direct band gap of *GaAs* were obtained as 1.5194 and 1.519 eV at 0 K.

The electronic energy band structure of *GaAs* has been also subject of many theoretical works [147, 150, 222–227]. The majority of the first principles band calculations employ the LDA for calculation of exchange-correlation effects. The direct band gap in *GaAs* is typically calculated (non relativistically) 1.1 -1.21 eV [222, 223] as opposed to the experimental value, 1.519 eV (T = 0 K). The discrepancy between the experiment and theory was found to be increased when the relativistic effects are included; the indirect band gap of *GaAs* was found (relativistically) to be in the range of 0.25 -0.64 eV [225, 226]. The underestimated values of E_g^Γ of DFT-LDA calculations are corrected to 1.47 [226] and 1.42 [227] eV by a quasi particle - GW approximations. In a recent work [147] the electronic band structure of *GaAs* was calculated by ETB with spds* basis. In this work, the band gap value of *GaAs* was fitted to its experimental value of 1.519 eV. In another recent work [150], the band gap of *GaAs* was calculated to be 1.424 eV by ETB - sps* calculations within a genetic algorithm approach.

Table 6.1: Empirical matrix elements of the sp^3d^2 Hamiltonian in eV.

	<i>GaN</i>	<i>GaAs</i>
E_{sa}	-9.4409	-7.1494
E_{sc}	-2.6598	-4.2967
E_{pa}	3.5174	1.7151
E_{pc}	6.5587	1.7851
E_{da}	19.2403	10.0743
E_{dc}	18.3328	7.8739
V_{ss}	-7.8046	-6.8523
V_{xx}	5.6790	1.9926
V_{xy}	8.2889	4.7066
V_{pcsa}	7.0460	5.5137
V_{pasc}	6.3688	4.3876
V_{dapc}	8.3554	4.9370
V_{dcpa}	0.0000	3.7868

In the present work, the electronic band structure of *GaN* and *GaAs* in zinc-blende phase has been calculated by empirical tight binding (ETB) method which is parameterized by the first principles calculational results of *GaN* and *GaAs*. The aim of this work is to derive the energy parameters of ETB providing well defined valence bands and energy gaps for *GaN* and *GaAs*. Therefore these energy parameters can be simply used in further calculations correspond to the electronic band structure calculations of ternary and quaternary alloys of *GaN* and *GaAs*. In the present work, the ETB energy parameters of sp^3d^2 for cubic *GaN* and *GaAs* are listed in Table 6.1. The electronic band structures of the compounds are separately discussed in the following sections and the conclusions are given in chapter 7.

6.2 The results

6.2.1 *c-GaN*

The zinc-blende structure of *GaN* is characterized by the lattice constant, a . The equilibrium value of a is determined by calculating the total energy of *c-GaN* using FP-LAPW for a set of volumes and fitting these to the Murnaghan equation [53]. We have adopted the value of 2.2 Å for *Ga* and 1.85 Å for *N* as the MT radii. The electronic configuration of *GaN* is *Ga*: Ar ($3d^{10}4s^24p^1$) and *N* : He ($2s^22p^3$). In the calculations, the electrons of *Ga* in ($1s^22s^22p^63s^23p^6$) are defined as the core electrons and distinguished from the valence electrons of *Ga* in ($3d^{10}4s^24p^1$). Similarly, the inner valence band electrons of *N* in ($1s^2$) are distinguished from the valence band electrons of *N* in ($2s^22p^3$) shell. The curve of the total energy versus the lattice constant is shown in Fig. 6.1. The equilibrium lattice constant of *c-GaN* is calculated to be 4.562 Å. The present lattice constant is given in Table. 6.2 together with the experimental and other calculated lattice constant values of *c-GaN* presented in the literature.

The present value of a for *c-GaN* is found to be very close to the result of 4.53 Å [196] measured by X-ray diffraction measurements. The present value of a is only (1.4 -1.6) % greater than other experimental results, 4.5 [203] and 4.49 Å [195]; they are measured by X-ray diffraction and optical absorption measurements, respectively. On the other hand, our lattice constant of *c-GaN* is also very

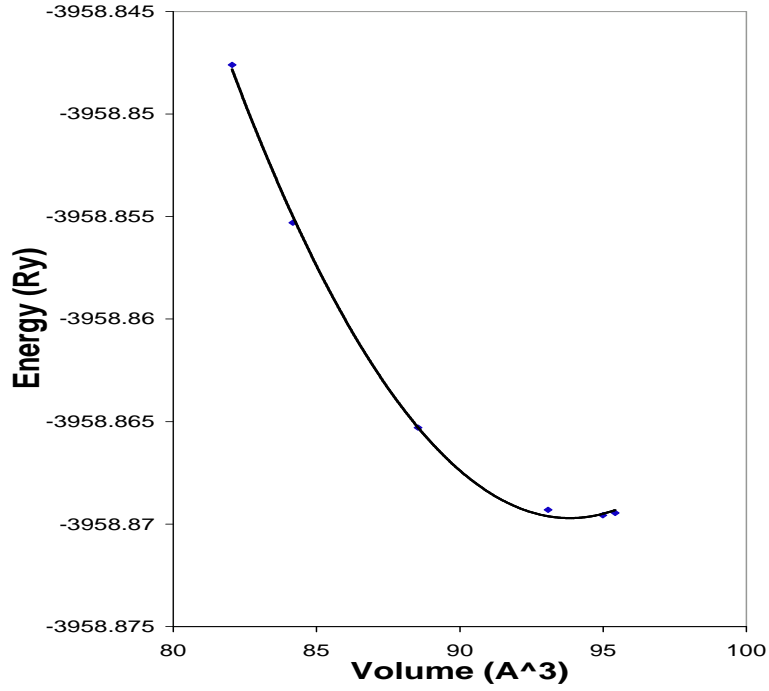


Figure 6.1: Total energy of *c-GaN* versus the lattice volume.

close to the values of 4.56 [94], 4.55 [209], 4.552 [103] and 4.59 [97] calculated by pseudopotential with self interaction correction (PP-SIC), DFT/FP-LAPW-GGA with quasi particle correction, DFT/FP-LAPW-LDA, and DFT/PPPW-GGA, respectively. The discrepancy between the present lattice constant and the one (4.518 Å) calculated by DFT/PPPW-LDA is only 0.97 %. The present lattice constant of *c-GaN* is (1.6 -3.14) % greater than the values calculated by FHI96MD, CASTEP, VASP codes [208], zero temperature Green's function formalism [211], non-corrected PP [94], self-consistent linear muffin tin orbital (SCLMTO) [92], and FP-APW-local orbitals methods [214].

Table 6.2: The theoretical and experimental lattice constant values (a_{th}, a_{exp}) in Å for GaN and $GaAs$ in cubic phase.

<i>Compound</i>	a_{th}	a_{exp}
<i>GaN</i>	4.562 ^a , 4.433 ^b (4.45, 4, 56) ^c (4.518, 4.59) ^d (4.423, 4.462, 4.452) ^e 4.55 ^f , 4.552 ^g , 4.49 ^h 4.4615 ⁱ	4.5 ^j 4.49 ^k 4.530 ^l
<i>GaAs</i>	5.632 ^a 5.570 ^m 5.6660 ⁿ , 5.6416 ^o 5.6518 ^p	5.65325 ^r

^apresent work, ^bRef. [92], ^cRef. [94], ^dRef. [97], ^eRef. [208], ^fRef. [209], ^gRef. [103], ^hRef. [211], ⁱRef. [214], ^jRef. [203], ^kRef. [195], ^lRef. [196], ^mRef. [223], ⁿRef. [150], ^oRef. [5], ^pRef. [222], ^rRef. [215]

We have employed DFT/FP-LAPW-GGA method in the band structure calculations of *c-GaN*. It is found that the band gap of *GaN* is direct in zinc-blende phase, furthermore, the band structure is in close agreement with the DFT-LDA results of previous reports [94, 103, 143, 213, 214]. The present DFT calculations within GG approximations do not give any new feature on the band structure of DFT-LDA, only the present E_g^Γ (2.25 eV) of *c-GaN* is slightly greater than the previously reported values of DFT-LDA [103, 104, 213, 214]. But the present fundamental band gap of *c-GaN* is still greater than the values reported by PL and modulated photoluminescence measurements [194, 202] at 10 K. This is a widely accepted result that the DFT-GGA (or LDA) electronic band structures are qualitatively in good agreement with the experiments in what concerns the

ordering of the energy levels and the shape of the bands, but whose band gap values are always smaller than the experimental data.

The present narrow direct band gap of *c-GaN* has been corrected empirically with respect to its experimental value of 3.3 eV [194]. The difference between the eigenvalues of the first conduction band and last valence band states calculated at the same k point is enlarged by an amount of the energy difference between the present direct band gap and 3.3 eV. Therefore the present fundamental band gap of *c-GaN* is improved without change of the ordering of the energy levels and the shape of the bands. The adjusted energy band structure of *c-GaN* by DFT/FP-LAPW-GGA is shown in Fig. 6.2. Since the *Ga* 3d orbitals are treated as valence orbitals in the calculations, the d bands are strongly hybridized with the bottom s-like valence bands (*N* 2s) which results in a large splitting away from Γ point. Therefore *Ga* 3d valence state electrons lead to increase of the valence bandwidth. On the other hand, p-d hybridization at the top of the valence band decreases the band gap of *c-GaN*. Table. 6.3 gives the important features of the present and previously reported band structures for *c-GaN* at high symmetry points. The present energy gaps at X and L points are also enlarged to 4.927 and 5.684 eV, respectively by direct band gap adjustment.

In the following stage of the work, the energy parameters of ETB have been derived for *c-GaN* from the present band structure of DFT/FP-LAPW-GGA (Fig. 6.2) by the fitting process explained in sec. 2.4. The recalculated band

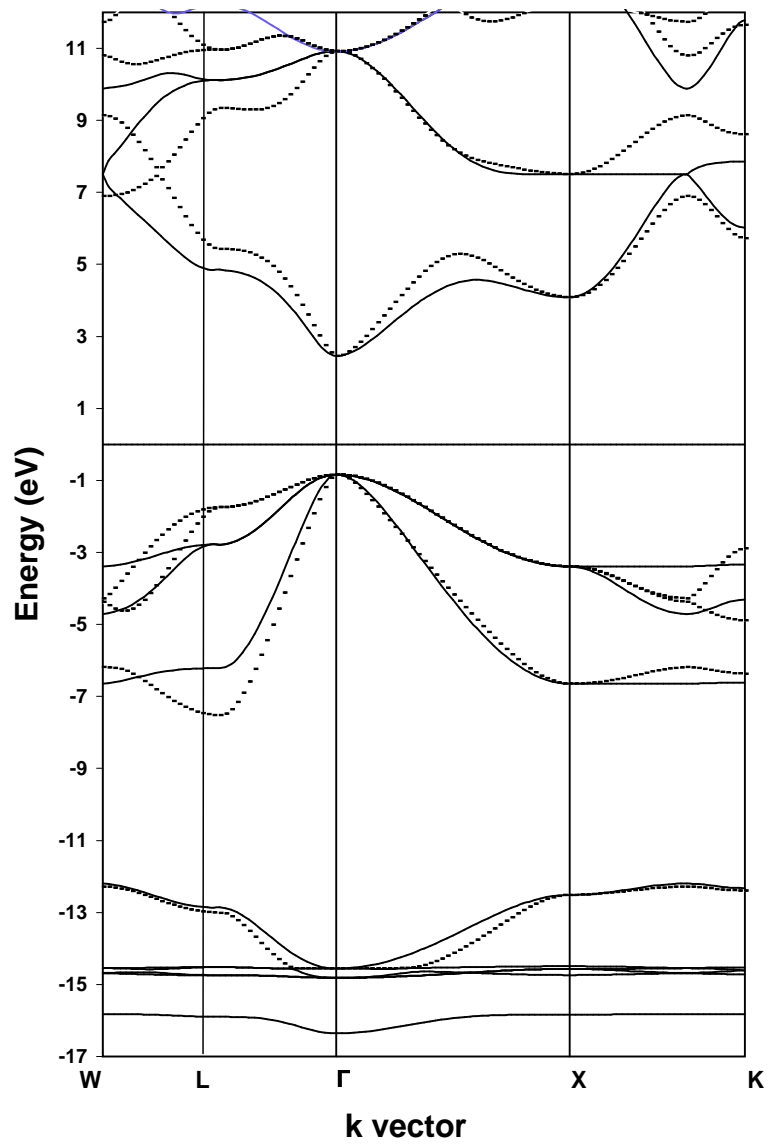


Figure 6.2: The energy band structure of *c-GaN* by FP-LAPW(adjusted) (dotted line) and ETB (solid line).

Table 6.3: A summary of the important features, energy gaps, and valence bandwidths of the present DFT (adjusted) and ETB band structure for *c-GaN* compared to other experimental and calculational results. All energies are in eV.

	<i>DFT^a</i> <i>adjusted</i>	<i>ETB^a</i>	<i>theoretical</i>				
			<i>DFT</i> <i>LDA^b</i>	<i>DFT</i> <i>LDA^c</i>	<i>DFT</i> <i>QP^c</i>	<i>EPP</i>	<i>EPP</i>
Γ_1^v	-14.560	-14.560	-15.7	-16.3	-17.8		
Γ_{15}^v	-0.841(3)	-0.841(3)	0.0(3)	0.0(3)	0.0(3)	0.000	0.000
Γ_1^c	2.459	2.459	1.9	2.1	3.1	3.308	3.213
Γ_{15}^c	10.917	10.917	10.2	10.6	12.2	10.098	10.248
X_1^v	-12.516	-12.516	-11.6	-13.0	-14.8		
X_3^v	-6.649	-6.649	-6.1	-6.5	-6.9	-6.294	-5.923
X_5^v	-3.389	-3.389	-2.7	-2.8	-3.0	-2.459	-2.086
X_1^c	4.086	4.086	3.2	3.2	4.7	4.428	4.585
X_3^c	7.507	7.507	6.7	6.9	8.4	6.010	6.265
L_1^v	-13.011	-12.864	-12.1	-13.8	-15.5		
L_1^v	-7.525	-6.217	-7.0	-7.4	-7.8	-6.812	-6.644
L_3^v	-1.748	-2.776	-1.0(2)	-1.0(2)	-1.1(2)	-0.834	-0.772
L_1^c	5.422	4.843	4.8	5.0	6.2	5.149	5.510
L_3^c	9.339	10.119	8.6	9.1	11.2	10.416	10.606
$\Gamma_{15}^v - \Gamma_1^c$	3.3	3.3	1.9 ^b	2.1 ^c	3.1 ^c	3.308 ^d	3.213 ^e
			1.8 ^f	2.18 ^g	2.33 ^g	3.383 ^h	1.6 ⁱ
			3.8 ⁱ	1.9 ^j	3.17 ^j	2.4 ^k	1.72 ^l
			2.41 ^m	1.93 ⁿ	1.6 ^o		
<i>exp.</i>			3.268 ^p	3.302 ^p	3.291 ^q		
$\Gamma_{15}^v - X_1^c$	4.927	4.927	3.2 ^b	3.2 ^c	4.7 ^c	4.428 ^d	4.585 ^e
			6.3 ^f	3.36 ^g	3.36 ^g	4.571 ^h	3.25 ⁿ
$\Gamma_{15}^v - L_1^c$	6.263	5.684	4.8 ^b	5.0 ^c	6.2 ^c	5.149 ^d	5.51 ^e
			5.8 ^f	4.93 ^g	4.99 ^g	5.636 ^h	4.73 ⁿ
$\Gamma_1^v - \Gamma_{15}^v$	15.515	13.718	15.7 ^b	16.3 ^c	17.8 ^c	13.6 ⁱ	16.7 ⁱ
			15.57 ^l	16.17 ⁿ			

^apresent work, ^bRef. [213], ^cRef. [143], ^dRef. [212], ^eRef. [207], ^fRef. [205], ^gRef. [92], ^hRef. [206], ⁱRef. [94], ^jRef. [208], ^kRef. [209], ^lRef. [103], ^mRef. [210], ⁿRef. [214], ^oRef. [97], ^pRef. [194], ^qRef. [202]

structure of *c-GaN* by ETB is shown in Fig. 6.2. The important features of the band structure at high symmetry points are listed in Table 6.3. As it is observed in Fig. 6.2, the valence band structure of *c-GaN* by ETB follows closely that of DFT along both Γ -X and Γ -L directions. The splitting of the top of the valence band position around W point in all DFT results is closed to X point in the present ETB calculations. The similar result was also obtained in EPP [206] and SCLMTO [92] calculations. The first state energies of the conduction band by ETB deviate from the present results of DFT around the mid point of Γ -X and X-K directions. But the energy gaps of *c-GaN* at Γ and X points are found to be exactly the same by both calculations. The present E_g^Γ value of 3.3 eV is very close to the values of DFT-LDA calculations corrected by a quasi particle, GW, and SIRC-PP [143, 94].

The present ETB band gap value of *c-GaN* is also very close to the values of 3.308, 3.213 and 3.383 eV calculated by EPP method [206, 207, 212]. The discrepancy between the present and uncorrected direct band gap values of *c-GaN* calculated by DFT-LDA [94, 97, 103, 143, 208, 209, 213, 214], SCLMTO [92] and zero temperature Green's function formalisms within random phase approximation [210, 211] is (0.9-1.7) eV. The present E_g^x is very close to the value of DFT-LDA calculations corrected by quasi particle and GW [143]. The value of E_g^x is (7.5-11.3) % greater than that of EPP calculations [206, 207, 212]. Since the present ETB calculations are parameterized with respect to the solution of

the secular equation at only Γ and X points, the present ETB results can not exactly give the result of the present DFT calculations at L point. The E_g^L of ETB is found to be smaller than that of the present DFT calculations. It is $\sim 8.3\%$ smaller than the value resulted in corrected DFT-LDA calculations [143]. On the other hand, the present E_g^L is very close to the values calculated by EPP [206, 207]. The present valence bandwidth of *c-GaN* calculated by ETB is smaller than that of the present and other DFT calculations [103, 143, 213, 214] in which *Ga* 3d orbitals are treated as the valence band orbitals. Although the present valence bandwidth is small compared to the result of SIRC-PP [94], it is very close to that of the PP calculations [94].

6.2.2 GaAs

The equilibrium lattice constant value of *GaAs* is obtained by total energy calculations based on DFT within GG approximation. The total energy for a set of volumes has been calculated by FP-LAPW method and fitted to the Murnaghan's equation [53]. We have adopted the value of 2.2 Å for Ga and 2.2 Å for As as the MT radii. The electronic configuration of *GaAs* is *Ga*: Ar ($3d^{10}4s^24p^1$) and *As*: Ar ($3d^{10}4s^24p^3$). In the calculations, the electrons of *Ga* in ($1s^22s^22p^63s^23p^63d^{10}$) are defined as the core electrons and distinguished from the valence electrons of *Ga* in ($4s^24p^1$). Similarly, the inner valence band electrons of *As* in ($1s^22s^22p^63s^23p^63d^{10}$) are distinguished from the valence band electrons of

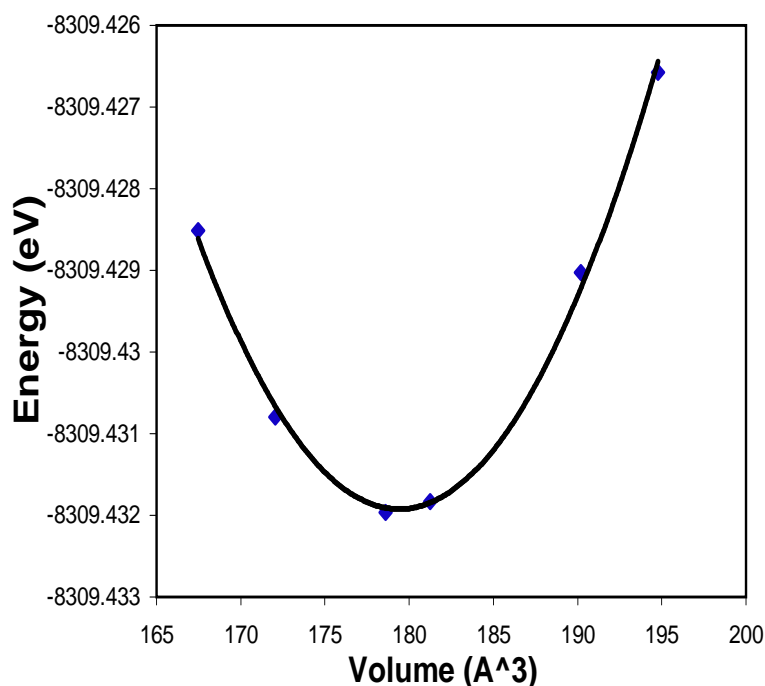


Figure 6.3: Total energy of *c-GaAs* versus the lattice volume.

As in ($2s^22p^3$) shell. The total energy of *GaAs* as a function of unit cell volume is shown in Fig. 6.3.

The calculated total energy of *GaAs* is found to be minimum with the lattice constant value of 5.632 Å. The present lattice constant value of *GaAs* is given in Table 6.2 together with the experimental and other calculated lattice constant values of *GaAs* presented in the literature. In an early work [215], the lattice constant of *GaAs* was measured to be 5.65325 Å by X-ray photoemission spectra. The present lattice constant of *GaAs* is very close to this measured value; the discrepancy is just 0.37 %. In linear combination of Gaussian orbitals (LCGO)-

LDA [222] calculations, the lattice constant of *GaAs*, was taken as 5.6518 Å. In PP-LDA [223] and ETB [150] calculations, the total energy was minimized with the lattice constant value of 5.570 and 5.6660 Å, respectively. The present lattice constant is closer to the recommended lattice constant value of 5.6416 Å [5] than those calculated by PP-LDA [223] and ETB-genetic algorithm [150].

The present electronic band structure of *GaAs* calculated by DFT/FP-LAPW-GGA is found to be similar with the results of LCGO-LDA [222], DFT-LDA (adjusted, relativistically) [224], PP-LDA (LMTO-LDA) [225] and ETB-spds* [147] calculations. As it is given in the literature, the ordering between the present energy gaps is $E_g^\Gamma < E_g^L < E_g^X$. The present energy gaps are all smaller than their measured values. As it is mentioned in the previous section, this is the weakness of the all DFT calculations; the variation of the band structure follows the measurements with small gaps at the high symmetry points. In the present work, the fundamental gap of *GaAs* is found to be 1.265 eV. This value is comparable with the corresponding values calculated by DFT-LDA [226], PP-LDA [223] and LMTO-LDA (non relativistically) [225]. The underestimated band gap values are corrected empirically by enlarging the gaps by an amount of energy equals to the difference between the present calculated and measured value of the fundamental band gap of *GaAs* (1.519eV). Therefore, the variation of the band structure of *GaAs* is held rigid, only the eigenvalues are changed equally. This correction is considered to be necessary before the derivation of ETB energy

parameters of *GaAs*. The adjusted energy band structure of *GaAs* by DFT/FP-LAPW-GGA is shown in Fig. 6.4. Table 6.4 gives the important features of the present and previously reported band structures for *GaAs* at high symmetry points. The value of E_g^x was measured to be 1.981 and 2.01 eV at 0 and 5 K by electroreflectance and PL measurement, respectively [216, 219]. In the same works [216, 219], the measured value of E_g^L was 1.815 and 1.84 eV. The present enlarged energy gap at X point (1.748 eV) is closer to its measured values (1.981 and 2.01 eV) than the ones calculated by DFT-LDA [226], PP-LDA [223], LCGO-LDA [222] and PP-GW [227]. Although the present E_g^L is not as close to the measurements [216, 217, 219] as the other corrected ones [147, 226, 227], it is quite corrected with respect to the results of standard DFT-LDA calculations [222, 223, 226].

In the following step of the work, the energy parameters of ETB have been derived for *GaAs* from the present eigenvalues of DFT (Fig. 6.4) by the fitting process explained in sec. 2.4. The band structure of *GaAs* recalculated by ETB is shown in the Fig. 6.4. The important features of the band structure at high symmetry points are listed in Table 6.4. In view of Fig. 6.4, we note that there is a close agreement between the band structure of *GaAs* by ETB and DFT around Γ and X points. The band gaps of *GaAs* at Γ and X points are found to be the same exactly in both present ETB and DFT/FP-LAPW-GGA calculations. As it is pointed out above, the present E_g^x is close to the measurements(1.98, 2.01

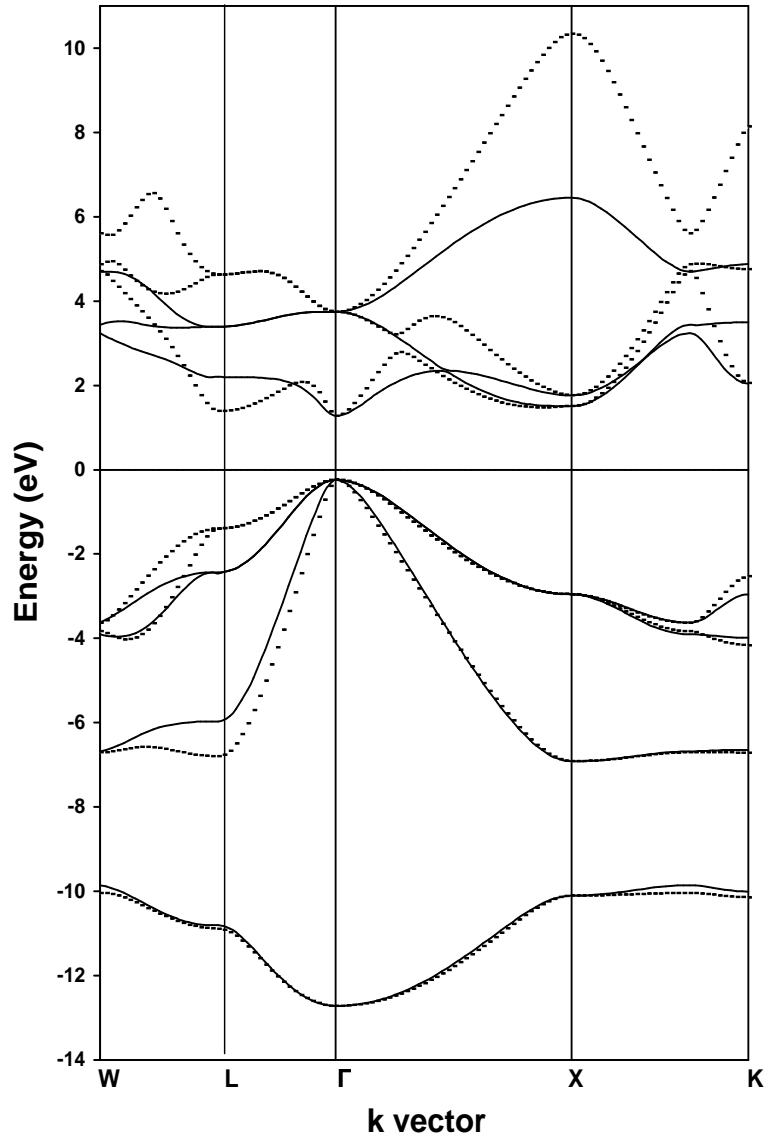


Figure 6.4: The energy band structure of *c-GaAs* by FP-LAPW(adjusted) (dotted line) and ETB (solid line).

Table 6.4: A summary of the important features, energy gaps and valance bandwidths of the present DFT (adjusted) and ETB band structure for *GaAs* compared to other experimental and calculational results. All energies are in eV.

	<i>DFT^a</i> <i>adjusted</i>	<i>ETB^a</i> <i>spd²</i>	<i>theoretical</i>				<i>ETB^e</i>	<i>exp.</i> <i>f</i>
			<i>DFT</i> <i>LDA^b</i>	<i>DFT</i> <i>GW^b</i>	<i>PP</i> <i>LDA^c</i>	<i>PP</i> <i>GW^d</i>		
Γ_1^v	-12.772	-12.722		-10.52	-11.71	-13.03	-12.910	-13.1
Γ_{15}^v	-0.243	-0.243	0.00	0.00	0.0	0.00	0.00	0.00
Γ_1^c	1.276	1.276	0.56	1.47	1.10	1.22	1.519	1.632
Γ_{15}^c	3.743	3.743	3.70	4.52		4.48	4.500	4.53
X_3^v	-6.919	-6.919			-6.62			-6.70
X_5^v	-2.957	-2.957	-2.66	-2.73	-2.61	-2.91	-2.929	-2.80
X_1^c	1.505	1.505	1.38	2.08	1.51	1.90	1.989	1.51
X_3^c	1.763	1.763	1.55	2.30		2.47	2.328	2.35
L_1^v	-6.804	-5.972			-6.46			-6.70
L_3^v	-1.397	-2.436	-1.07	-1.11	-1.11	-1.28	-1.084	-1.30
L_1^c	1.386	2.196	1.04	1.82	1.30	1.64	1.837	1.85
L_3^c	4.625	3.390	4.57	5.41		5.40	5.047	5.47
$\Gamma_{15}^v - \Gamma_1^c$	1.519	1.519	0.56 ^b 1.61 ^m	1.47 ^b	1.10 ^c	1.22 ^d	1.21 ^m	1.632 ^f 1.519 ^g 1.5189 ^j 1.5194 ^l 1.52 ^h
$\Gamma_{15}^v - X_1^c$	1.748	1.748	1.38 ^b 1.61 ^m	2.08 ^b	1.30 ^c	1.64 ^d	1.837 ^e	1.51 ^f 1.981 ^h 2.01 ⁱ
$\Gamma_{15}^v - L_1^c$	1.629	2.439	1.04 ^b 1.37 ^m	1.82 ^b	1.51 ^c	1.90 ^d	1.989 ^e	1.85 ^f 1.815 ^h 1.84 ⁱ
$\Gamma_1^v - \Gamma_{15}^v$	12.479	12.479	12.33 ^c	13.03 ^d	12.91 ^e	12.35 ^m		13.1 ^f

^apresent work, ^bRef. [226], ^cRef. [223], ^dRef. [227], ^eRef. [147], ^fRef. [217], ^gRef. [162, 167], ^hRef. [216], ⁱRef. [219], ^jRef. [218], ^kRef. [221], ^lRef. [220], ^mRef. [222]

eV) [216, 219]; the discrepancy is (12-13)%. Although the ETB valence band structure follows the present eigenvalues of DFT closely (Fig. 6.4) along Γ -X direction, it is deviated along Γ -L direction. On the other hand, the maximum seeing on the first conduction band state along Γ -X direction (Fig. 6.4) is shifted towards the X point in the result of ETB calculations. Along Γ -L direction the first conduction band state structure of ETB is quite different than the structure calculated by DFT. Since the present ETB energy parameters are adapted for only the external values at Γ and X points, E_g^L is not found to be close to that of DFT calculations. The width of the valence band is found to be the same in both present ETB and DFT calculations. The present valence bandwidth of both calculations is closer to its measured value of 13.1 eV [217] than the results of PP-LDA [223] and LCGO-LDA [222] calculations.

CHAPTER 7

CONCLUSIONS

In the present work, the electronic band structure of III (*In, Al, Ga*)- V (*N, As, Sb*) compounds and their ternary alloys have been investigated by DFT within GG approximation and ETB calculations, respectively.

The III-V compounds have been considered in zinc-blende phase defined by their equilibrium lattice constants obtained from the present calculations of total energy minimization. The lattice constants of *InAs*, *InSb*, *AlSb*, *AlAs* and *GaN* compounds have been calculated within a small discrepancy ($\leq 2.5\%$) compared to experimental values. An excellent agreement appears between the present calculated and available experimental values of lattice constant for *InN*, *AlN* and *GaAs* compounds.

The present DFT-GGA calculations have shown direct band gap structures in zinc-blende phase for *InN*, *InAs*, *InSb*, *GaN*, and *GaAs*. However, indirect band gap structures have been obtained for cubic *AlN*, *AlSb* and *AlAs* compounds; here, the conduction band minima of both *AlN* and *AlAs* are located

at X symmetry point, while that of *AlSb* is at a position lying along $\Gamma - X$ direction. The energy gaps found by the present DFT-GGA calculations for the above cited compounds at high symmetry points have the same ordering as the experimental gaps, but the calculated ones remain systematically smaller. This is a widely accepted result in the literature for all standard DFT calculations. These underestimated band gap values have been empirically corrected using the experimental ones for *InAs*, *InSb*, *AlN*, *AlSb*, *AlAs*, *GaN*, and *GaAs* compounds. Due to the lack of experimental results, the calculated direct band gap value of *InN* has been attempted to improve considering the gap value supplied by corrected DFT- local density approximation (LDA) calculations given in the literature.

An important part of this work consists of ETB calculations which have been parameterized for sp^3d^2 basis and nearest neighbor interactions to study the band gap bowing of III(*In, Al*)- V(*N, As, Sb*) ternary alloys. The energy parameters of ETB have been derived from the eigenvalues of the present DFT calculations carried on all compounds considered in this work. Since the band gap values of the compounds are responsible for the band gap engineering of their ternary and quaternary alloys, we have concentrated to have well defined band gaps for compounds at high symmetry points.

It is found that, the ETB energy parameters can reproduce the valence band

structure of InN , $InAs$ and $InSb$ satisfactorily. The ETB valence band structure of compounds follows the valence band structure of DFT/FP-LAPW-GGA closely. The valence bandwidth of the compounds is exactly the same for both present ETB and DFT calculations. Furthermore, they are comparable with the reported theoretical and experimental results. The energy variation of the first conduction band state of the compounds does not follow the corresponding energy variation of the present DFT calculations closely. However, the ETB energy band gap values of the compounds are exactly the same with those of DFT/FP-LAPW-GGA at Γ and X points. The present E_g^L of ETB is also very close to that of DFT for $InAs$. But for the other compounds, InN and $InSb$, the ETB energy parameters seem to be insufficient to give the present energy gap of DFT at L point. However, the calculated E_g^L values of the compounds by ETB are still comparable with the corresponding theoretical values given in the literature.

In the present work, the conduction band dispersion has been analyzed around Γ point for the alloys considered in this work with small contents (x). It is found that a small amount of N and As in InN_xAs_{1-x} , InN_xSb_{1-x} and $InAs_xSb_{1-x}$ alloys, respectively decreases the electron effective mass around Γ point. The decrease of the electron effective mass in InN_xSb_{1-x} is realized to be relatively greater than in InN_xAs_{1-x} alloys by a small increase of nitrogen concentration.

The ETB energy parameters of AlN , $AlSb$, $AlAs$ obtained from the present first principles calculations have been tested by recalculating the energy band

structure of the compounds. The band gap and the valence bandwidth values of *c-AlN* by ETB are found to be very close to the corresponding values given in the literature. The good agreement between the present and experimental equilibrium lattice constant values of *c-AlN* might have a contribution to obtain good band gap energies. In the present ETB calculations, the indirect band gap of *AlSb* is found to be close to its experimental value, but the direct band gap has a small discrepancy with its experimental value. A small discrepancy is also found between the present and reported valence bandwidth values of *AlSb*. In ETB calculations of *AlAs*, the indirect band gap is small (~ 0.3 eV) with respect to the largest discrepancy (~ 1 eV) belongs to a theoretical result reported before. The valence band width of *AlAs* is found to be close to the corresponding values given in the literature.

The ETB energy parameters of *GaN* and *GaAs* obtained from the present first principles calculations have been also tested by recalculating the energy band structure of the compounds. Since the present ETB equations are formulated only at Γ and X points, they are defective in the calculation of E_g^L for *c-GaN* and *GaAs*. But, it is found that the ETB energy band gap values of the compounds are exactly the same with those of DFT/FP-LAPW-GGA at Γ and X points.

In the literature, the first optical transition of the ternary and quaternary alloys of the semiconductor compounds was generally defined at either Γ or X point. Since the present ETB energy parameters successfully reproduce the band

structures of the compounds at Γ and X symmetry points, they are considered reliable for the band gap bowing calculations of the InN_xAs_{1-x} , InN_xSb_{1-x} , $InAs_xSb_{1-x}$, $Al_{1-x}In_xN$, $Al_{1-x}In_xSb$ and $Al_{1-x}In_xAs$. The ETB energy parameters of compounds have been scaled by r^{-2} and used in Vegard's law to find out the interaction energy parameters of the alloys considered in this work.

The calculated fundamental band gap values of these ternary alloys for different concentration of N and As have been compared with the available room or low temperature PL peak energies of the corresponding samples grown epitaxially on the substrate. According to the knowledge of authors, this is the first study that calculates the band structure of bulk InN_xAs_{1-x} , InN_xSb_{1-x} and $InAs_xSb_{1-x}$ alloys for complete range of contents.

The present bowing of the band gap has been found to be sharp for small N concentration in InN_xAs_{1-x} alloys as it was resulted by the room temperature PL measurements. The calculated bowing parameter is close to the value recommended in the literature. Since InN_xAs_{1-x} alloys have not been investigated in the large range of N , the metallic characteristics of them found in the present work was not observed experimentally, but it was predicted both experimentally and theoretically. The present band gap bowing of InN_xSb_{1-x} alloys has not found to be as sharp as the room temperature reported results for small concentrations of N . Because of this the cross point found in the present work is much greater than that of the $\vec{k} \cdot \vec{p}$ calculations which model the room temperature

PL measurements.

In the present work, the change of the band gap for small concentrations of *As* in InN_xSb_{1-x} alloys has found to be small with respect to the variation of the PL peak energies of the corresponding samples at low temperatures. The present ETB calculations showed that InN_xSb_{1-x} alloys have a large band gap bowing and metallic character in the range of $0.4 < x < 0.63$. In the literature, the bowing parameter of InN_xSb_{1-x} alloys at low temperature was reported to be high with respect to its room temperature values. The present bowing parameter has been found to be also greater than the bowing parameters measured at 10 K and room temperature. Since the band structure of the materials depend on temperature, we couldn't find the close agreement between the present band gap values calculated at 0 K and the band gap values measured at low and room temperatures. But, it is found that the present ETB energy parameters of bulk InN , $InAs$ and $InSb$ are able to supply the general feature of the band gap bowing for InN_xAs_{1-x} , InN_xSb_{1-x} and $InAs_xSb_{1-x}$ alloys.

In the present work, the band structure of $Al_{1-x}In_xN$, $Al_{1-x}In_xSb$ and $Al_{1-x}In_xAs$ have been calculated and the variation of E_g^Γ and E_g^X has been investigated with respect to the *In* concentration *x*. The present bowing for Γ and X point transitions is found to be downward for all $Al_{1-x}In_xN$, $Al_{1-x}In_xSb$ and $Al_{1-x}In_xAs$ alloys. This result is the same in most of the theoretical reports given in the literature. But, the numerical value of the bowing parameter for E_g^Γ

and E_g^X of alloys is various in the literature. The difference between the calculated bowing parameters of E_g^Γ and E_g^X for the same alloys might be originated from both different energy gaps and lattice constant values of the compounds used in their calculations.

REFERENCES

- [1] S. N. Mohammad and H. Morkoç, *Prog. Quantum Electronic* **20**, 361 (1996).
- [2] A. Yamamoto, M. Tsujino, M. Ohkubo and A. Hashimoto, *Sol. Energy Mater. Sol. Cells.* **35**, 53 (1994).
- [3] S. Nakamura and G. Fasol, *The blue laser diodes* (Springer, Berlin 1997).
- [4] A. Dagar, J. Christen, T. Riemann, S. Richler, J. Blassing, A. Diez, A. Krost, A. Alam and M. Heuken, *Appl. Phys. Lett.* **78**, 2211 (2001).
- [5] I. Vurgaftman, J. R. Meyer, and L. Ram-Mohan, *J. Appl. Phys.* **89**, 5815 (2001). and references cited therein.
- [6] *Wide band gap semiconductors, proceeding of the Seventh Trieste Semiconductors Symposium, 1992*, edited by C. G. Van de Walle (North Holland, Amsterdam 1993).
- [7] J. F. Kaeding, Y. Wu, T. Fujii, R. Sharma, P. T. Fini, J. S. Speck, and S. Nakamura, *J. Crystal Growth.* **272**, 257 (2004).
- [8] T. Kawashima, A. Miyazaki, H. Kasugai, S. Mishima, A. Honshio, Y. Miyake, M. Iwaya, S. Kamiyama, H. Amano, and I. Akasaki, *J. Crystal Growth.* **272**, 270 (2004).
- [9] O. Aktas, Z. F. Fan, S. N. Mohammad, A. E. Botchkarev, H. Morkoc, *Appl. Phys. Lett.* **69**, 3872 (1996).
- [10] K. Wang, R. R. Reber, *Appl. Phys. Lett.* **79**, 1602 (2001).
- [11] L. F. Luo, R. Beresford, and W. I. Wang, *Appl. Phys. Lett.* **53**, 2320 (1998).
- [12] C. R. Bolognesi, M. W. Dvorak, and D. H. Chow, *J. Vac. Sci. Technol. A* **16**, 843 (1998).
- [13] T. P. Smith III, W. I. Wang, F. F. Fang, and L. L. Chang, *Phys. Rev. B* **35**, 9349 (1987).
- [14] T. S. Lay, J. J. Heremans, Y. W. Suen, M. B. Santos, K. Hirakawa, M. Shayegan, and A. Zrenner, *Appl. Phys. Lett.* **62**, 3120 (1993).

- [15] H. C. Casey and M. B. Panish, Heterostructure lasers (Academic, New York, 1978), and references therein.
- [16] C. E. Volin, J. P. Garcia, E. L. Dereniak, M. K. Descour, T. Hamilton, and R. McMillan, *Appl. Opt.* **40**, 4501 (2001).
- [17] B. J. Kirby and R. K. Hanson, *Appl. Opt.* **41**, 1190 (2002).
- [18] B. Brar, L. Samoska, H. Kroemer, and J. H. English, *J. Vac. Sci. Tech. B* **12**, 1242 (1994).
- [19] J. M. McKenna, D. D. Nolte, W. Walukiewicz, and P. Becla, *Appl. Phys. Lett.* **68**, 735 (1996).
- [20] D. H. Chow, H. L. Dunlap, W. Williamson, S. Enquist, B. K. Gilbert, S. Subramaniam, P. M. Lei, and G. H. Bernstein, *IEEE Electron Device Lett.* **17**, 69 (1996).
- [21] M. Osiński, *Opto-electro. Rev.* **11**, 321 (2003).
- [22] T. Aschley, T. M. Burhe, G. J. Pryce, A. R. Adams, A. Andreev, B. N. Murdin, E. P. O'Reilly, and C. R. Pidgeon, *Sol. State Elec.* **47**, 387 (2003).
- [23] G. B. Stringfellow and P. E. Greene, *J. Electrochem. Soc.* **118**, 805 (1971).
- [24] M. Y. Yen, B. F. Levine, C. G. Bethea, K. K. Choi, and A. Y. Cho, *Appl. Phys. Lett.* **50**, 927 (1987).
- [25] M. Y. Yen, R. People, K. W. Wecht, and A. Y. Cho, *Appl. Phys. Lett.* **52**, 489 (1988).
- [26] Z. M. Fang, K. Y. Ma, D. H. Jaw, R. M. Cohen, and G. B. Stringfellow, *J. Appl. Phys.* **67**, 7034 (1990).
- [27] S. Elies, A. Krier, I. R. Cleverley, and K. Singer, *J. Phys. D* **26**, 159 (1993).
- [28] K. T. Huang, C. T. Chiu, R. M. Cohen, and G. B. Stringfellow, *J. Appl. Phys.* **75**, 2857 (1994).
- [29] V. K. Dixit, B. Bansal, V. Venkataraman and H. L. Bhat, *Appl. Phys. Lett.* **81**, 1630 (2002).
- [30] M. Weyers, M. Sato, and H. Ando, *Jpn. J. Appl. Phys. Part 2* **31**, L853 (1992).
- [31] M. Weyers and M. Sato, *Appl. Phys. Lett.* **62**, 1396 (1993).

- [32] S. Yamaguchi, M. Kariya, S. Nitta, T. Takeuchi, C. Wetzel, H. Amano, and I Akasaki, *Appl. Phys. Lett.* **76**, 876 (2000).
- [33] S. Yamaguchi, Y. Iwamura, and A. Yamamoto, *Appl. Phys. Lett.* **82**, 2065 (2003).
- [34] O. B. Shchekin, J. Ahn, and D. G. Deppe, *Electron Lett.* **38**, 712 (2002).
- [35] G. Yusa and H. Sakaki, *Appl. Phys. Lett.* **70**, 345 (1997).
- [36] M. Udhayasankar, J. Kumar, and P. Ramasamy, *J. Crystal Growth.* **268**, 389 (2004).
- [37] S. Sinharoy, M. A. Stan, A. M. Pal, V. G. Weizer, M. A. Smith, D. M. Wilt, and K. Reinhardt, *J. Crystal Growth.* **221**, 683 (2000).
- [38] E. A. Pease, L. R. Dawson, L. G. Vaughn, P. Rotella, and L. F. Lester, *J. Appl. Phys.* **93**, 3177 (2003).
- [39] P. S. Dutta, *J. Crystal Growth.* xx, xxx (2004).
- [40] P. Hohenberg and W. Kohn, *Phys. Rev.* **136**, B864 (1964).
- [41] W. Kohn and L. J. Sham, *Phys. Rev.* **140**, A1 133 (1965).
- [42] J. P. Perdew and Y. Wang, *Phys. Rev. B* **45**, 13244 (1992).
- [43] D. R. Hartree, *Proc. Cambridge Phil. Soc.* **25**, 225, 310 (1927).
- [44] M. Cardona, *J. Phys. Chem. Solids*, **24**, 1543 (1963).
- [45] M. Cardona, *J. Phys. Chem. Solids*, **26**, 1351 (1965).
- [46] W. A. Harrison, *Phys. Today*, **22**, 23 (1969).
- [47] J. C. Slater and G. F. Koster, *Phys. Rev.* **94**, 1498 (1954).
- [48] W. A. Harrison, *Elementary Electronic Structure* (World Scientific Publishing 1999).
- [49] V. Fock, *Z. Phys.* **61**, 126 (1930).
- [50] J. C. Slater. *Phys. Rev.* **81**, 385, (1951).
- [51] F. Bloch, *Z. Physik*, **52**, 555 (1928).

- [52] P. Blaha, K. Schwarz, G.K.H. Madsen, D. Kvasnicka, J. Luitz, WIEN2K, An Augmented-Plane-Wave + Local Orbitals Program for Calculating Crystal Properties, Karlheinz Schwarz, Techn. Wien, Austria, 2001, ISBN 3-9501031-1-2.
- [53] F. D. Murnaghan, Proc. Natl. Acad. Sci. U. S. A. **30**, 244 (1944).
- [54] D. J. Chadi and M.L.Cohen, Phys. Stat. Sol. (b)**68**, 405 (1975).
- [55] P. Vogl, P. H. P. Hjalmarson and J. D. Dow, J. Phys. Chem. Solids, **44**, 365 (1983).
- [56] S. L. Richardson and M. L. Cohen, Phys. Rev. B **35**, 1388 (1987).
- [57] L. Vegard, Z. Phys. **5**, 17 (1921).
- [58] J. Wu, W. Walukiewicz, K. M. Yu, J. W. Ager III, E. E. Haller, H. Lu, W. J. Schaff, Y. Saito, and Y. Nanishi, Appl. Phys. Lett. **80**, 3967 (2002).
- [59] T. Matsuka, H. Ohamoto, M. Nakao, H. Harima, and E. Kurimoto, Appl. Phys. Lett. **81**, 1246 (2002).
- [60] A. Tabata, A. P. Lima, L. K. Teles, L. M. R. Scolfaro, J. R. Leite, V. Lemos, B. Schöttker, T. Frey, D. Schikora, and K. Lischka, Appl. Phys. Lett. **74**, 362 (1999); A. P. Lima, A. Tabata, J. R. Leite, S. Kaiser, D. Schikora, B. Schöttker, T. Frey, D. J. As, and K. Lischka, J. Crystal Growth **202**, 396 (1999).
- [61] G. Kaczmarczyk, A. Kaschner, S. Reich, A. Hoffmann, C. Thomasen, D. J. As, A. P. Lima, D. Schikora, K. Lischka, R. Averbeck, and H. Riechert, Appl. Phys. Lett. **76**, 2122 (2000).
- [62] V. Lemos, E. Silveira, J. R. Leite, A. Tabata, R. Trentin, L. M. R. Scolfaro, T. Frey, D. J. As, D. Schikora, and K. Lischka, Phys. Rev. Lett. **84**, 3666 (2000).
- [63] V. Cimalla, J. Pezoldt, G. Ecke, R. Kosiba, O. Ambacher, L. Spieb, G. Teichert, H. Lu, And W. J. Schaff, Appl. Phys. Lett. **83**, 3468 (2003).
- [64] Q. Guo and A. Yoshida, Jpn. J. Appl. Phys. Part1 (**33**), 2453 (1994).
- [65] F. Bechstedt, and J. Furthmüller, J. Crystal Growth **246**, 315 (2002).
- [66] D. Bagayoko, L. Franklin, and G. L. Zhao, J. Appl. Phys. **96**, 4297 (2004).
- [67] M. Fisher and A. Krier, Infrared Phys. and Technol. **38**, 405 (1997).

- [68] R. D. Grober, H. D. Drew, J. Chyi, S. Kalem and H. Morkoc, *J. Appl. Phys.* **65**, 4079 (1989).
- [69] X. Marcadet, A. Rakouska, J. Prevot, G. Glastre, B. Vinter, and V. Erger, *J. Crystal Growth* **227**, 609 (2001).
- [70] G. H. Kim, J. B. Choi, J. Y. Leem, J. Y. Leem, J. I. Lee, S. K. Noh, J. S. Kim, S. K. Kang, and S. I. Ban, *J. Crystal Growth* **234**, 110 (2002).
- [71] L. Ley, R. A. Pollak, F. R. McFeely, S. P. Kowalczyk, and D. A. Shirley, *Phys. Rev. B* **9**, 600 (1974).
- [72] Z. M. Fang, K. Y. Ma, R. M. Cohen, and G. B. Stringfellow, *Appl. Phys. Lett.* **59**, 1446 (1991).
- [73] Y. Lacroix, C. A. Tran, S. P. Watkins, and M. L. W. Thewalt, *J. Appl. Phys.* **80**, 6416 (1996).
- [74] *Semiconductors - Basic Data*, edited by: O. Madelung, (Berlin; Springer, 1996). ISBN 3-540-60883-4.
- [75] J. R. Dixon and J. M. Ellis, *Phys. Rev.* **123**, 1560 (1961).
- [76] W. A. Harrison, *Electronic structure and the properties of solids* (Freeman, San Fransisco, 1980).
- [77] M. Huang and W. Y. Ching, *J. Phys. Chem. Solids Vol.* **46**, 977 (1985).
- [78] J. R. Chelikowsky and M. L. Cohen, *Phys. Rev. B* **14**, 556 (1976).
- [79] D. N. Talwar and C. S. Ting, *Phys. Rev. B* **25**, 2660 (1982).
- [80] N. Bouarissa and H. Aourag, *Infrared Phys. and Technol.* **38**, 153 (1997).
- [81] J. P. Loehr and D. N. Talwar, *Phys. Rev. B* **55**, 4353 (1997).
- [82] G. Theodorou and G. Tsegas, *Phys. Rev. B* **61** 10782 (2000).
- [83] T. D. Mishima and M. B. Santos, *J. Vac. Sci. Technol.* **B22**, 1472 (2004).
- [84] V. K. Dixit, B. Banial, V. Venkataraman, H. L. Bhat, G. N. Subbanna, K. S. Chandrasekharan, and B. M. Arora, *Appl. Phys. Lett.* **80**, 2102 (2002).
- [85] N. L. Rowell, *Infrared Phys. and Technol.* **28**, 37 (1988).
- [86] C. L. Littler and D. G. Seiler, *Appl. Phys. Lett.* **46**, 986 (1985).

- [87] T. D. Veal, I. Mahboob, and C. F. McConville, *Phys. Rev. Lett.* **92**, 136801 (2004).
- [88] E. J. Mele and J. D. Joannopoulos, *Phys. Rev. B* **24**, 3145 (1981).
- [89] M. Alouani, L. Brey, and N. E. Christensen, *Phys. Rev. B* **37**, 1167 (1988).
- [90] R. Asahi, W. Mannstadt, and A.J. Freeman, *Phys. Rev. B* **59**, 7486 (1999).
- [91] A. Seidl, A. Görling, P. Vogl, J. A. Majewski, and M. Levy, *Phys. Rev. B* **53**, 3764 (1996).
- [92] N. E. Christensen and I. Gorczyca, *Phys. Rev. B* **50**, 4397 (1994).
- [93] M. Fuchs, J. L. F. Da Silva, C. Stampfl, J. Neugebauer, and M. Scheffler, *Phys. Rev. B* **65**, 245212 (2002).
- [94] D. Vogel, P. Krüger, and J. Pollmann, *Phys. Rev. B* **55**, 12836 (1997).
- [95] A. F. Wright and J. S. Nelson, *Phys. Rev. B* **51**, 7866 (1995).
- [96] A. Muñoz and K. Kunc, *J. Phys.: Condens. Matter* **5**, 6015 (1993).
- [97] C. Stampfl and C. G. Van de Walle, *Phys. Rev. B* **59**, 5521 (1999).
- [98] A. Satta, V. Fiorentini, A. Bosin, F. Meloni, and D. Vanderbilt, in *Gallium Nitride and Related Compounds*, edited by R. D. Dupuis, J. A. Edmond, F. Ponce, and S. Nakamura, MRS Symposia Proceedings, No. 395 (Materials Research Society, Pittsburgh, 1996), p. 515.
- [99] M. Buongiorno Nardelli, K. Rapcewicz, E. L. Briggs, C. Bungaro, J. Bernholc, in *III-V Nitrides*, edited by F. A. Ponce, T. D. Moustakas, I. Akasaki, and B. A. Monemar, MRS Symposia Proceedings No. 449 (Materials Research Society, Pittsburgh, 1997), p. 893.
- [100] C. -Y. Yeh, Z. W. Lu, S. Froyen, and A. Zunger, *Phys. Rev. B* **46**, 10086 (1992).
- [101] M. Van Schilfgaarde, A. Sher, and A.-B. Chen, *J. Crystal Growth* **178**, 8 (1997).
- [102] K. Kim, W. R. L. Lambrecht, and B. Segall, *Phys. Rev. B* **53**, 16 310 (1996).
- [103] L. E. Ramos, L. K. Teles, L. M. R. Scolfaro, J. L. P. Castineira, A. L. Rosa, and J. R. Leite, *Phys. Rev. B* **63**, 165210 (2001).

- [104] A. Zoroddu, F. Bernardini, P. Ruggerone, and V. Fiorentini, *Phys. Rev. B* **64**, 045208 (2001).
- [105] J. Serrano, A. Rubio, E. Hernández, A. Muñoz, and A. Mujica, *Phys. Rev. B* **62**, 16612 (2000).
- [106] D. Chandrasekhar, D. J. Smith, S. Strite, M. Lin, and H. Morkoç, *J. Crystal Growth* **152**, 135 (1995).
- [107] D. Fritsch, H. Schmidt, and M. Grundmann, *Phys. Rev. B* **69**, 165204 (2004).
- [108] R. W. Godby, M. Schlüter, and L. J. Sham, *Phys. Rev. B* **37**, 10159 (1988).
- [109] D. A. As, D. Schikora, and K. Lischka, *Phys. Stat. Sol. (c)* **6**, 1607 (2003).
- [110] S. Huai Wei, X. Nie, I. G. Batyrev, and S. B. Zhang, *Phys. Rev. B* **67**, 165209 (2003).
- [111] J. V. Ozolin'sh, G. K. Averkieva, A.F. Ilvin'sh, and N. A. Goryunova, *Sov. Phys. Cryst.* **7**, 691 (1963).
- [112] R. W. G. Wyckoff, *Crystal structures*, (John Wiley and Sons Inc, New York, London, Sydney, 1963).
- [113] C. H. Lin, Y. Sun, S. B. Visbeck, D. C. Law, and R. F. Hicks, *Appl. Phys. Lett.* **81**, 3939 (2002).
- [114] S. B. Zhang and Marvin L. Cohen, *Phys. Rev. B* **35**, 7604 (1987).
- [115] S. Massidda, A. Continenza, A. J. Freeman, T. M. de Pascale, F. Meloni, and M. Serra, *Phys. Rev. B* **41**, 12079 (1990).
- [116] I. N. Remediakis and E. Kaxiras, *Phys. Rev. B* **59**, 5536 (1999).
- [117] S. A. Semiletov and M. Rozsibal, *Kristallografiya*, **2**, 287 (1957).
- [118] M. E. Straumanis and C. D. Kim, *J. Appl. Phys.* **36**, 3822 (1965).
- [119] *Numerical Data and Functional Relationship in Science and Technology, Crystal and Solid State Physics*, Vol. **17** a. of Landolt Börnstein edited by O. Madelung (Springer, Berlin 1984).
- [120] D. Singh and Y. P. Varshni, *Phys. Rev. B* **32**, 6610 (1985).
- [121] G. Y. Guo, J. Crain, P. Blaha, and W.M. Temmerman, *Phys. Rev. B* **47**, 4841 (1993).

- [122] S. Bei der Kellen and A. J. Freeman, *Phys. Rev. B* **54**, 11187 (1996).
- [123] *Numerical Data and Functional Relationship in Science and Technology*, New series, group III Vol. **23** a. edited by A. Goldman, and E. E. Koch (Springer, Berlin 1989).
- [124] D. E. Eastman, W. D. Grobman, J. L. Freeouf, and M. Erbudak, *Phys. Rev. B* **9**, 3473 (1974).
- [125] H. C. Casey, Jr. and M. B. Panish, *Heterostructure Lasers, Part A: Fundamental Principles* (Academic, New York, 1978).
- [126] H. Naoi, Y. Naoi, and S. Sakai, *Solid State. Electricity.* **41**, 319 (1997).
- [127] T. Yang, S. Nakajima, and S. Sakai, *Jpn. J. of Appl. Phys.* **36**, L320 (1997).
- [128] N. Tit and M. W. C. Dharma-Wardana, *Appl. Phys. Lett.* **76**, 3576 (2000).
- [129] H. Naoi, D. M. Shaw, Y. Naoi, G. J. Collins, S. Sahai, *J. Crystal Growth* **222**, 511 (2001).
- [130] J.-S. Wang, H-H. Lin, L-W. Song, and G-R. Chen, *J. Vac. Sci. Technol. B* **19**, 202 (2001).
- [131] B. N. Murdin et al., *Appl. Phys. Lett.* **78**, 1568 (2001).
- [132] I. Mahboob, T. D. Veal, and C. F. McConville, *Appl. Phys. Lett.* **83**, 2169 (2003).
- [133] J. C. Woolley and J. Warner, *Can. J. Phys.* **42**, 1879 (1964).
- [134] J. A. Van Vechten and T. K. Bergstresser, *Phys. Rev. B* **1**, 3351 (1970).
- [135] R. Magri and A. Zunger, *IEEE Proc. Optoelectron.* **150**, 409 (2003).
- [136] S. Nakamura, P. Jayavel, T. Koyama, M. Kumagama, Y. Hayakawa, *J. Crystal Growth* **274**, 362 (2005).
- [137] W. Shan, W. Walukiewicz, J. W. Ager III, E. E. Haller, J. F. Geisz, D. J. Friedman, J. M. Olson, and S. R. Kurtz, *Phys. Rev. Lett.* **82**, 1221 (1999).
- [138] C. W. Tu, *J. Phys. Condens. Matter*, **13**, 7169 (2001).
- [139] I. Vurgaftman and J. R. Meyer, *J. Appl. Phys.* **94**, 3675 (2003).
- [140] C. E. A. Grigorescu and R. A. Stradling, *Handbook of thin Film Devices*, edited by M. H. Francombe (Academic, NewYork, 2000) Vol. 2 p27.

- [141] C. Alibert, A. Joullié, A. M. Joullié, and C. Ance, Phys. Rev. B **27**, 4946 (1983).
- [142] M. L. Cohen and T. K. Bergstresser, Phys. Rev. **141**, 789 (1966).
- [143] A. Rubio, J. L. Corkill, M. Cohen, E. Shirley, and S. G. Louie, Phys. Rev. B **48**, 11810 (1993).
- [144] J. L. Corkill, A. Rubio, and M. L. Cohen, J. Phys: Condens. Matter. **6**, 963 (1994).
- [145] S. H. Wei and A. Zunger, Appl. Phys. Lett. **69**, 2719 (1996).
- [146] D. Vogel, P. Kruger, and J. Pollmann, Phys. Rev. B **55**, 25 (1997).
- [147] J. M. Jancu, R. Scholz, F. Beltram, and F. Bassani, Phys. Rev. B **57**, 6493 (1998).
- [148] Properties, processing and applications of GaN and related semiconductors, edited by J. H. Edgar, S. Strite, I. Akasaki, H. Amano and C. Wetzel, EMIS Data reviews series No: **23** 1999.
- [149] M. G. M. Armenta, A. R. Serrato, and M. A. Borja, Phys. Rev. B **62**, 4890 (2000).
- [150] G. Klimeck, R. C. Bowen, T. B. Boykin and T. A. Cwik, Superlatt. and Microstruct. **27**, 519 (2000).
- [151] M. P. Thompson, G. W. Auner, T. S. Zheleva, K. A. Jones, S. J. Simko, and J. N. Hilfiker, J. Appl. Phys. **89**, 3321 (2001).
- [152] F. Litimein, B. Bouhafs, Z. Dridi, and P. Ruterana, New J. of Phys. **4**, 64 (2002).
- [153] J. -M. Jancu, F. Bassani, F. D. Sala, and R. Scholz, Appl. Phys. Lett. **81**, 4838 (2002).
- [154] S. H. Rhim, M. Kim, and A. J. Freeman, Phys. Rev. B **71**, 045202 (2005).
- [155] K. Karch and f. Bechstedt, Phys. Rev. B **56**, 7404 (1997).
- [156] M. Ueno, A. Onodera, O. Shimomura, and K. Takemura, Phys. Rev. B **45**, 10123 (1992).
- [157] I. Petrov, E. Majab, R. C. Powell, J. E. Greene, L. Hultman, and J. -E. Sundgren, Appl. Phys. Lett. **60**, 2491 (1992).

- [158] Semiconductors: Physics of Group IV Elements and III-V Compounds, edited by K. -H. Hellewege , O. Madelung and Landolt-Bornstein, New Series, Group III, Vol. 17, pt. a. (Springer-Verlag, Berlin 1982).
- [159] S. Q. Wang and H. Q. Ye, Phys. Rev. B **66**, 235111 (2002).
- [160] Physics of Group IV elements and III-V Compounds, edited by K. -H. Hellewege , O. Madelung and Landolt-Bornstein, New Series, Group III, Vol. 17, pt. a. (Springer Verlag, Berlin 1991).
- [161] K. Strössner, S. Ves, C. K. Kim, and M. Cardona, Phys. Rev. B **33**, 4044 (1986).
- [162] Semiconductors, Intrinsic properties of Group IV elements and III-V, II-VI and I-VII compounds, edited by K. -H. Hellewege , O. Madelung and Landolt-Bornstein, New Series, Group III, Vol. 22, pt. a. (springer-Verlag, Berlin 1987).
- [163] D. H. Ehlers, F. U. Hillebecht, C. T. Lin,. E. Schönherr, and L. Ley, Phys. Rev. B **40**, 3812 (1989).
- [164] M. Ettenberg and R. J. Pfaff, J. Appl. Phys. **41**, 3926 (1970).
- [165] P. P. Rushton, S. J. Clark, and D. J. Tozer, Phys. Rev. B **63**, 115206 (2001).
- [166] B. I. Min, S. Massida, and A. J. Freeman, Phys. Rev. B **38**, 1970 (1988).
- [167] Physics of Group IV Elements and III-V Compounds of Landolt-Bornstein, numerical data and Functional Relationships in Science and Technology: Newseries, Group III, Vol. 17. a, edited by O. Madelung, M. Schultz and H. Weiss (Springer, Newyork, 1982).
- [168] G. S. Spencer, A. C. Ho, J. Menéndez, R. Droopad, H. Fathollanejad, and G. N. Maracas, Phys. Rev. B **50**, 14125 (1994).
- [169] G. C. Osbourn and D. L. Smith, Phys. Rev. B **19**, 2124 (1979).
- [170] M. Guzzi, E. Grilli, S. Oggioni, J. L. Staelhi, C. Bosio, and L. Pavesi, Phys. Rev. B **45**, 10951 (1992).
- [171] S. J. Pearton, J. W. Lee, J. D. Mackenzie, C. R. Abernathy, and R. J. Shui, Appl. Phys. Lett. **67**, 2329 (1995).
- [172] D. J. Stukel and R. N. Euwema, Phys. Rev. **188**, 1193(1969).

- [173] A. F. Wright and J. S. Nelson, *Appl. Phys. Lett.* **66**, 3465 (1995).
- [174] S. Bounab, Z. Charifi, and N. Bouarissa, *Physica B* **324**, 72 (2002).
- [175] L. K. Teles, L. M. R. Scolfaro, J. Furthmüller, F. Bechstedt, and J. R. Leite, *Phys. Stat. Sol. (b)* **234**, 956 (2002); *J. Appl. Phys.* **92**, 7109 (2002).
- [176] L. K. Teles, J. Furthmüller, L. M. R. Scolfaro, A. Tabata, J. R. Leite, F. Bechstedt, T. Frey, D. J. As, and K. Lischka, *Physica E* **13**, 1086 (2002).
- [177] D. N. Talwar, D. Sofranko, C. Mooney, and S. Tallo, *Mat. Sci. and Engineering B* **90**, 269 (2002).
- [178] W. W. Lin, Y. K. Kuo, and B. T. Liou, *Jpn. J. Appl. Phys.* **43**, 113 (2004).
- [179] T. V. Shubina, V. V. Mamutin, V. A. Vekshin, V. V. Ratnikov, A. A. Toropov, A. A. Sitnikova, S. V. Ivanov, M. Karlsteen, U. Södervall, M. Willander, G. Pozina, J. P. Bergman, and B. Monemar, *Phys. Stat. Sol. (b)* **216**, 205 (1999).
- [180] T. Peng, J. Piprek, G. Qiu, J. O. Lowolafe, K. M. Unruh, C. P. Swann, and E. F. Shubert, *Appl. Phys. Lett.* **71**, 2439 (1997).
- [181] M. Lukitsh, Y. V. Danylyuk, V. M. Naik, C. Huang, G. W. Auner, L. Rimai, and R. Naik, *Appl. Phys. Lett.* **79**, 632 (2001).
- [182] M. Ferhat, *Phys. stat. Sol. (b)* **241**, R38 (2004).
- [183] S. Yamaguchi, M. Kariya, S. Nitta, H. Kato, T. Takeuchi, C. Wetzel, H. Amano, and I. Akasaki, *J. Crystal Growth.* **195**, 309 (1998); *Appl. Phys. Lett.* **73**, 830(1998).
- [184] K. S. Kim, A. Saxler, P. Kung, M. Razegni, and K. Y. Lim, *Appl. Phys. Lett.* **71**, 800 (1997).
- [185] Ya. Agaev and N. G. Bekmedova, *Sov. Phys. Semicond.* **5**, 1330 (1972).
- [186] S. Isomura, F. G. D. Prat, and J. C. Woolley, *Phys. Stat. Sol. (b)* **65**, 213 (1974).
- [187] N. Dai, F. Brown, R. E. Doezema, S. J. Chung, K. J. Goldaumer, and M. B. Santos, *Appl. Phys. Lett.* **73**, 3132 (1998).
- [188] B. Wakefield, M. A. G. Halliwell, T. Kerr, D. A. Andreuos, G. J. Davies, and D. R. Wood, *Appl. Phys. Lett.* **44**, 341 (1984).
- [189] J. M. Rodriguez and G. Armelles, *J. Appl. Phys.* **69**, 965 (1991).

- [190] K. A. Mader, A. Zunger, Phys. Rev. B **51**, 10462 (1995).
- [191] Properties of Group III Nitrides, edited by J. H. Edgar (EMIS, London, 1994).
- [192] Y.-F. Wu, B. P. Keller, S. Keller, D. Kapolnek, P. Kozodoy, S. P. Denbaars, and U. K. Mishra, Appl. Phys. Lett. **69**, 1438 (1996).
- [193] S. Nakamura, J. Crystal Growth, **202**, 290(1999).
- [194] G. Ramirez-Flores, H. Navarro-Contreras, A. Lastras-Martinez, R. C. Powell, and J. E. Greene, Phys. Rev. B **50**, 8433 (1994).
- [195] T. Lei, T. D. Moustakas, R. J. Graham, Y. He, S. J. Berkowitz, J. Appl. Phys. **71**, 4933 (1992).
- [196] R. C. Powell, N.-E. Lee, Y.-W. Kim, and J. E. Greene, J. Appl. Phys. **73**, 189 (1993).
- [197] H. Okumura, S. Yoshida, and T. Okahisa, Appl. Phys. Lett. **64**, 2997 (1994).
- [198] J. Menniger, U. Jahn, O. Brandt, H. Yang, and K. Ploog, Phys. Rev. B **53**, 1881 (1996).
- [199] D. J. As, F. Schmilgus, C. Wang, B. Schöttker, D. Schikora, and K. Lischka, Appl. Phys. Lett. **70**, 1311 (1997).
- [200] H. Okumura, H. Hamaguchi, T. Koizumi, K. Balakrishnan, Y. Ishida, M. Arita, S. Chichibu, H. Nakanish, T. Nagatomo, S. Yoshida, J. Crystal Growth, **189**, 390 (1998).
- [201] C. Adelman, E. Martinez Guerrero, F. Chabuel, J. Simon, B. Bataillou, G. Mula, Le Si Dang, N. T. Pelekanos, B. Daudin, G. Feuillet and H. Mariette, Mat. Sci. and Eng. B **82**, 212 (2001).
- [202] D. Xu, H. Yang, J. B. Li, D. G. Zhao, S. F. Li, S. M. Zhuang, R. H. Wu, Y. Chen, and G. H. Li, Appl. Phys. Lett. **76**, 3025 (2000).
- [203] S. Strite, J. Ran, Z. Li, A. Salvador, H. Chen, D. J. Smith, W. J. Choyke, and H. Morkoc, J. Vac. Sci. Technol. B **9**, 1924 (1991).
- [204] Z. H. Feng, H. Yang, X. H. Zheng, Y. Fu, Y. P. Sun, X. M. Shen, and Y. T. Wang, Appl. Phys. Lett. **82**, 206 (2003).
- [205] J. Petalas, S. Logothetidis, S. Bouladakakis, M. Alouani, and J. M. Wills, Phys. Rev. B **52**, 8082 (1995).

- [206] W. J. Fan, M. F. Li, T. C. Chong, and J. B. Xia, *J. Appl. Phys.* **79**, 188 (1996).
- [207] A. Tadjer, B. Abbar, M. Rezki, H. Aourag, and M. Certier, *J. Phys. Chem. Solids* **60**, 419 (1999).
- [208] S. K. Pugh, D. J. Dugdale, S. Brand, and R. A. Abram, *Semicond. Sci. Technol.* **14**, 23 (1999).
- [209] V. I. Gavrilenko and R. Q. Wu, *Phys. Rev. B* **61**, 2632 (2000).
- [210] C. Persson, A. Ferreira da Silva, R. Ahuja, and B. Johansson, *J. Crystal Growth*, **231**, 397 (2001).
- [211] C. Persson, Bo E. Sernelius, R. Ahuja, and B. Johansson, *J. Appl. Phys.* **92**, 3207 (2002).
- [212] D. Fritsch, H. Schmidt, and M. Grundmann, *Phys. Rev. B* **67**, 235205 (2003).
- [213] B. Bouhafs, F. Litimein, Z. Dridi1, and P. Ruterana, *Phys. Stat. Sol. (b)***236**, 61 (2003).
- [214] M. B. Kanouna, A. E. Merada, J. Cibert, H. Aourag, G. Merada, *J. Alloys and Compounds*, **366**, 86 (2004).
- [215] J. B. Mullin, B. W. Straughan, C. M. H. Driscoll and A. F. W. Willoughby, *J. of Appl. Phys.* **47**, 2584 (1976).
- [216] D. E. Aspnes, C. G. Olson and D. W. Lynch, *Phys. Rev. Lett.* **37**, 766 (1976).
- [217] T. -C. Chiang, J. A. Knapp, M. Aono, and D. E. Eastman, *Phys. Rev. B* **21**, 3513 (1980).
- [218] P. Lautenschlager, M. Garriga, S. Logothetidis, and M. Cardona, *Phys. Rev. B* **35**, 9174 (1987).
- [219] D. J. Wolford and J. A. Bradley, *Solid State Commun.* **53**, 1069 (1985).
- [220] E. Grilli, M. Guzzi, R. Zamboni, and L. Pavesi, *Phys. Rev. B* **45**, 1638 (1992).
- [221] M. El Allali, C. B. Sorensen, E. Veje, and P. Tidemand-Petersson, *Phys. Rev. B* **48**, 4398 (1993).
- [222] C. S. Wang and B. M. Klein, *Phys. Rev. B* **24**, 3393 (1981).

- [223] S. Froyen and M. L. Cohen, Phys. Rev. B **28**, 3258 (1983).
- [224] N. E. Christensen, Phys. Rev. B **30**, 5753 (1984).
- [225] G. B. Bachelet and N. E. Christensen, Phys. Rev. B **31**, 879 (1985).
- [226] R. W. Godby and M. Schlüter, L. J. Sham, Phys. Rev. B **35**, 4170 (1987).
- [227] X. Zhu and S. G. Louie, Phys. Rev. B **43**, 14142 (1991).

VITA

PERSONAL INFORMATION

Surname, Name : Mohammad, Rezek Mahmoud Salim
Nationality : Palestinian.
Date and Place of birth : August 16th, 1967, Kuwait.
Marital Status : Married.
Phone : +97292672749
e – mail : rezek@metu.edu.tr; esteteh@hotmail.com

EDUCATION

Dgree	Institution	Year of Graduation
<i>MS</i>	<i>Al – Najah University, Physics</i>	2001
<i>BS</i>	<i>Yarmouk University, Jordan</i>	1989
<i>High School</i>	<i>Jleeb Ilshyookh High School</i>	1985

Special courses in Accounting For Public Companies, management and Finance, Kuwait National University, (1989-1990).

WORK EXPERIENCE

Year	Place	Enrollment
1991 – present	<i>Palestine Technical Colleges; Palestine</i>	<i>Instructor</i>
1990 – 1991	<i>Natinal Bnak Of Kuwait</i>	<i>Accountant</i>

PUBLICATIONS

1. MUSA EL-HASAN and REZEK Mohammad, "ENERGY GAP DEPENDENCE ON ANION CONCENTRATION FOR $Ga_xIn_{1-x}As_yP_{1-y}$ QUATERNARY ALLOY BY RECURSION METHOD", Modern Physics Letters B, **18**, 955 (2004).

2. Rezek Mohammad, Şenay Katircioğlu and Musa El-Hasan, "The Electronic Band Structure of InN, InAs and InSb compounds", Submitted to Physical Rev. B 2005.
3. Rezek Mohammad and Şenay Katircioğlu, "The Electronic Band Structure of InN_xAs_{1-x} , InN_xSb_{1-x} and $InAs_xSb_{1-x}$ alloys", Submitted to Physical Rev. B 2005.
4. Rezek Mohammad and Şenay Katircioğlu, "The electronic band structure of AlN, AlSb, AlAs and their ternary alloys with In", Submitted to Physical Rev. B 2005.
5. Rezek Mohammad and Şenay Katircioğlu, "The Electronic Band Structure of GaN and GaAs for band gap bowing of $In_xGa_{1-x}N_yAs_{1-y}$ alloys", Submitted to Physical Rev. B 2005.